Chair of Subsurface Engineering

Master's Thesis

Changes in geotechnical soil parameters due to influence of hydrothermal alteration at the volcano La Soufrière de Guadeloupe

Langer Katharina-Sophie, B.Sc.

Februar 2023

MONTANUNIVERSITÄT LEOBEN
www.unileoben.ac.at

AFFIDAVIT

I declare on oath that I wrote this thesis independently, did not use other than the specified sources and aids, and did not otherwise use any unauthorized aids.

I declare that I have read, understood, and complied with the guidelines of the senate of the Montan university Leoben for "Good Scientific Practice".

Furthermore, I declare that the electronic and printing version of the submitted thesis are identical, both, formally and with regard content.

Date 23 February 2023

Signature Author
Katharina-Sophie Langer

"Wünsche dir nicht, es wäre einfacher, wünsche dir, dass du besser wirst."

Jim Rohn

Acknowledgments

All dies wäre ohne die tatkräftige Unterstützung meiner Betreuerin assoz. Prof. Dr. Marlene Villeneuve nicht möglich gewesen. It was a wonderful and inspiring collaboration – thank you!
Einen herzlichen Dank ebenso an die Lehrstuhlleiter Univ.-Prof. Mag.rer.nat. Dr.mont. Frank Melcher und Univ.-Prof. Dipl.-Ing. Dr.mont. Robert Galler, die mir die Möglichkeit boten, meine Thesis an ihren Instituten abzuschließen. Darüber hinaus bedanke ich mich für die lehrreiche Zeit in Leoben.

Weiters möchte ich mich für die vielen konstruktiven Fachgespräche abseits der Universität bei meiner Kollegin und Freundin DI Elisabeth Hauzinger bedanken, du warst mir stets eine herausragende Hilfe!
Derselbe Dank gilt meinem Freund und Partner MMst. Aleks Kamenov, ohne dessen erfinderischen Geist keine Motorisierung der Scherversuchsapparatur möglich gewesen wäre. Merci für die vielen motivierenden Gespräche, deine Geduld und das Verständnis, vor allem in dieser letzten sehr zeitintensiven Lern- und Arbeitsphase. Мерси, Твой съм.
Anna, danke dass du immer mein Ruhepol warst, nach dessen Aufenthalt ich die Welt zerreißen konnte!

Nicht zu vergessen ist der Dank an meine Eltern – Danke, dass ihr mir diese Zeit an der Montanuniversität ermöglicht und mir stets beiseite gestanden habt. Eure tröstenden und motivierenden Worte ließen mich das Haus immer stärker als zuvor verlassen!

Abschließend möchte ich mich noch bei all den Personen bedanken, die mir meine Studienzeit in Leoben so wunderbar gemacht haben. Hierbei könnte ich unzählige Namen auflisten, doch es würde sich nicht alle auf dieser Seite ausgehen. Ihr wisst Bescheid – ihr seid großartig!

Abstract

The island of Basse-Terre, part of the Lesser Antilles in the western Caribbean, has been affected for centuries by both magmatic and phreatic eruptions from the volcano La Soufrière de Guadeloupe. In particular, the hot and toxic circulating fluids affect the slope stability of the volcano and increase the risks for various landslides.

The influence of these hydrothermal fluids on the geotechnical parameters of the material is explained in this thesis. For this purpose, ten samples of in-situ altered material were taken, sealed and later analyzed in a soil laboratory. Six of them came from the immediate environment of the summit (Cratère sud and Gouffre Tarissan), three from the Faille la Ty fault zone south of the peak, and another from a landslide to the southeast of the peak.

Sieve and sedimentation analysis, direct shear test, Atterberg limits, pH, grain density, water content, XRF, and XRD were used for classification of the material.

The degree of alteration could be determined to range between argillic and advanced argillic, as represented by the alteration minerals kaolinite/halloysite, smectite and opal.

Smectite is recognized only in the samples collected around the summit and is no longer represented in the more advanced altered samples. Samples with increasing content of this clay mineral show higher friction angles and cohesion, and thus higher strength. Their plasticity is also increasing.

Kaolinite/halloysite-containing material shows higher cohesion while still lowering the friction angle. The higher the amount of kaolinite/halloysite, the higher the shear strength is.

Amorphous silica phases, such as opal, have been found in the highly altered zones. The increasing content has a positive effect on the cohesion, a negative one on the friction angle and no consequence on the strength. The higher amount of amorphous silica decreases the plasticity of the material.

The progression of alteration shows no influence on the grain density nor the proportion of fine particle size. It is spatially variable, with no clear link to distance from active craters, such that alteration-induced material weaking cannot be identified easily at the surface.

Kurzfassung

Die Insel Basse-Terre, die zu den Kleinen Antillen in der westlichen Karibik gehört, ist seit Jahrhunderten von magmatischen und phreatischen Eruptionen des Vulkans La Soufrière de Guadeloupe erschüttert. Vor allem die heißen und toxischen zirkulierenden Fluide beeinträchtigen die Hangstabilität des Vulkans und erhöhen die Risiken für diverse Hangrutschungen.

Der Einfluss dieser hydrothermalen Gewässer auf die geotechnischen Parameter des Materials wird in dieser Arbeit erläutert. Zu diesem Zweck wurden zehn Proben von in-situ alteriertem Material entnommen, versiegelt und später in einem Bodenlabor analysiert. Sechs davon stammen aus der unmittelbaren Umgebung des Gipfels (Cratère sud und Gouffre Tarissan), drei aus der Störungszone Faille la Ty südlich - und eine weitere aus einem Hangrutsch im Südosten des Vulkangipfels.

Zur Klassifizierung des Materials wurden Sieb- und Sedimentationsanalysen, direkte Schertests, Atterberg Grenzen, pH-Wert, Korndichte, Wassergehalt, RFA und RDA verwendet.

Der Grad der Alteration konnte dabei auf argillisch bis fortgeschritten argillisch bestimmt werden. Die auftretenden Alterationsminerale sind vor allem Kaolinit/Halloysit, Smektit und Opal.

Smektit ist nur in den Proben zu erkennen, die in der Nähe des Gipfels gesammelt wurden und ist in jenen mit fortgeschrittener Alteration nicht mehr vertreten. Proben mit zunehmendem Gehalt an diesem Tonmineral weisen höhere Reibungswinkel, höhere Kohäsion und eine höhere Festigkeit auf. Ihre Plastizität nimmt ebenfalls zu.

Kaolinit-/Halloysit-haltiges Material weist eine höhere Kohäsion auf und senkt gleichzeitig den Reibungswinkel. Je höher der Anteil an Kaolinit/Halloysit, desto höher ist die Scherfestigkeit.

Das amorphe Minerale Opal wurden in den stark alterierten Zonen gefunden. Der zunehmende Gehalt in den Proben wirkt sich positiv auf die Kohäsion und negativ auf den Reibungswinkel aus. Es hat keine Auswirkungen auf die Festigkeit. Der höhere Anteil an dieser Phase vermindert die Plastizität des Materials.

Der Fortschritt der Alteration hat keinen Einfluss auf die Korndichte oder den Anteil der Feinkorngröße. Er ist räumlich variabel und steht in keinem eindeutigen Zusammenhang mit der Entfernung von aktiven Kratern, sodass eine alterationsbedingte Materialschwächung an der Oberfläche nicht ohne weiteres zu erkennen ist.

Table of Content

1 Introduction

Volcanoes are often ticking time bombs due to their unstable structures that can pose a hazard to their surroundings in a variety of ways. Not only the effusive eruption itself, but also the creeping hazards should not be underestimated. In fact, partial flank collapses at about 200 volcanoes have resulted in at least 20,000 fatalities over the past 10,000 years (Siebert et al., 2010). About 52% of these flank collapses are associated with magmatic eruption, but 22% with phreatic and/or hydrothermal eruption (Siebert, 1984; Siebert et al., 1987; Siebert et al., 2010).

Hydrothermal alteration is often an insidious process that accompanies volcanism for years and significantly affects stability. Many studies already show that such alterations can weaken a volcano strongly enough to promote collapse (Ball et al., 2013; Ball et al., 2015; Ball et al., 2018; Cecchi et al., 2004; Del Potro and Hürlimann, 2009; Finn et al., 2007; John et al., 2008; López and Williams, 1993; Opfergelt et al., 2006; Reid et al., 2001; Rosas-Carbajal et al., 2016; Salaün et al., 2011; van Wyk de Vries and Francis, 1997; Voight B., 2002; Watters and R. Zimbelman, 2000).

The volcano La Soufrière de Guadeloupe situated in the Lesser Antilles, Eastern Caribbean, is a basaltic-andesite to andesitic arc volcano and has a long eruption history with both magmatic - as well as phreatic eruptions (Komorowski et al., 2005; Komorowski et al., 2013a; Komorowski et al., 2013b; Legendre, 2012). In 1976, the most violent phreatic eruption with 26 non-magnetic explosions forced 73,000 people to leave their homes for up to 6 months (Boudon et al., 1988b; Feuillard et al., 1983; Komorowski et al., 2005). After some quiet years it reawakened in 1992 by restarting its fumarolic and seismic activities (Komorowski et al., 2005). In April 2018, the largest volcano-tectonic earthquake with an magnitude of 4.1 (Moretti et al., 2020) took place.

The unrest originates from an underlying magmatic body beneath the dome which causes the circulation of acid-chloride sulfate fluids. Degassing of the magma chamber supply CO_2, SO_2, H_2S, HCl and HF to the hydrothermal system (Villemant et al., 2005; Villemant et al., 2014).
The fluids are transported to the summit fumaroles and circulate through the dome structure along listric discontinuities that drain to the southwest (Brombach et al., 2000; Rosas-Carbajal et al., 2016; Salaün et al., 2011; Villemant et al., 2014).
This causes alteration of the country rock. Especially the shallow area shows advanced argillic alteration, which developed due to the circulation of cooled (150°C – 350°C), acidic (pH < 4) fluids, possibly mixed with meteoric waters (Heap et al., 2021).

The reawakening of La Soufrière de Guadeloupe in 1992 raised concerns about the stability of the southwest flank of the dome. It shows the largest displacements with up to 9 mm a year over the last 20 years (Moretti et al., 2020), therefore a lot of research has been done in the last couple of years.

The Montana university of Leoben started together with Université de Strasbourg, Institut Universitaire de France (IUF), Johannes Gutenberg University Mainz, Terrestrial Magmatic Systems (TeMaS) Research Platform in Mainz, Université de Paris, Technical University Munich, Observatoire Volcanologique et Sismologique de Guadeloupe and University College Dublin some geophysical, geomechanical and mineralogical investigations at the volcano. Also some numerical modelling had been done. To provide input parameters for the stability analyses, rock samples have been tested. As already mentioned, the volcano is not just built up out of solid rock, but also of converted, altered soil with different stability and hardness.

For further research on the material comprising La Soufrière, ten samples of soil like material with different degrees of alteration were taken in May 2022. Six of them derived from the area around the summit. One was taken from a former land slide east of the peak of the summit dome, and three from a normal fault south-east of it. Sieve and sedimentation analysis, direct shear test, Atterberg limits, pH-value, grain density, water content, XRD and XRF have been used for the soil classifications.
The goal was to find the correlations between porosity, shear strength, plasticity, pH-value, grain size, clay minerals with increasing alteration. The results of the analysis are presented in this thesis.

2 Research and background

2.1 Geographical setting

Guadeloupe is one of the four oversea departments of France and is situated in the Eastern Caribbean. It consists of nine islands: Basse-Terre, Grande-Terre, La Désirade, Petite-Terre, Marie-Galante, Terre-de-Haut, Terre-de-Bas, Saint-Barthélémy, Saint-Martin. The largest islands are Basse-Terre (848 km^2) and Grand-Terre (590 km^2). They are shown in Figure 1. In the south of Basse-Terre is the active volcano La Soufrière de Guadeloupe, with 1.467m height and only 5 km N of the town Saint-Claude, with a population of about 10.500 people (Komorowski et al., 2005).

The volcano la Soufrière de Guadeloupe is part of the Grand Découvert-Soufrière volcanic complex and is the only part out of 7 eruptive fields on Basse-Terre, which have been active in the last 10.000 years (Komorowski et al., 2005).

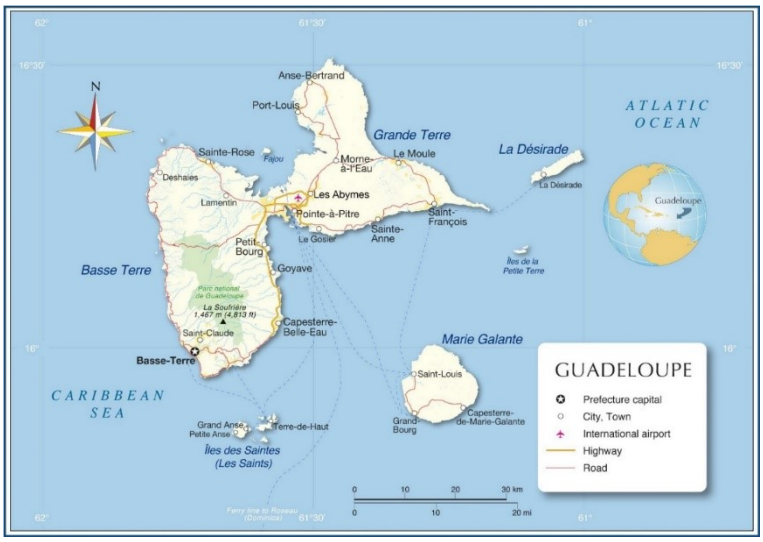

Figure 1: Map of Guadeloupe https://www.orangesmile.com/common/img_country_maps/guadeloupe-map-0.jpg; 29.11.2022)

2.2 Geological overview

The island itself is part of the Lesser Antilles, which mark the eastern boundary of the Caribbean Plate. They are located at the eastern margin of the large igneous province-thickened oceanic crust of the Caribbean plate (Mauffret and Leroy, 1997). The Caribbean plate has been moving in eastward direction relative to the North and South American plate over the last 100 My (Schlaphorst et al., 2021).
Typical structures like strike-slip boundaries joined the subduction of the plates. This resulted in a large shear zone through both continental and ocean crust, as well as in arc volcanism at various times and places on the plate margin (Boschman et al., 2014).

The Lesser Antilles and its islands formed due to westward subduction of the North and South American plates beneath the Caribbean Plate (Wadge and Shepherd, 1984). The boundary between these two is not located yet and probably diffused along the front of the Lesser Antilles arc (Bouysse and Westercamp, 1988). With an rate of 18-20 mm a year, the subduction is very slow (DeMets et al., 2000).
The geodynamical setting of this is illustrated in Figure 2.

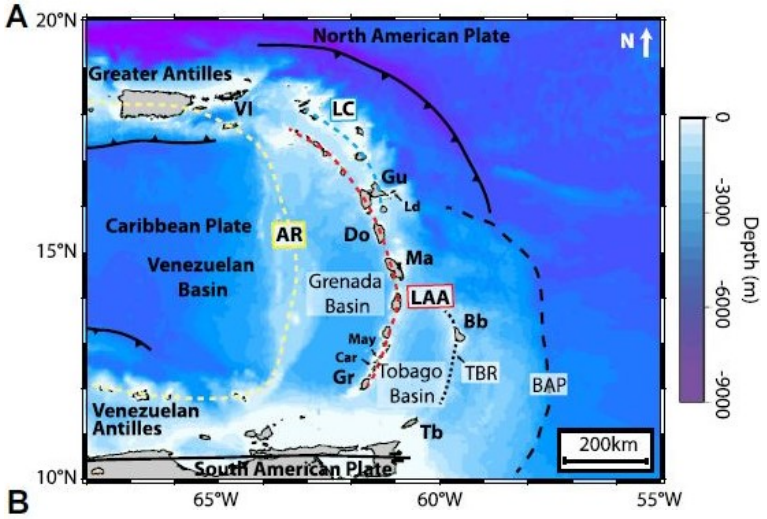

Figure 2: (A) Map of the Lesser Antilles region highlighting the major tectonic features. Abbreviations: LAA—Lesser Antilles arc (red dashed line), LC—Limestone Caribbees (blue dashed line), AR—Aves Ridge (yellow dashed line), VI—Virgin Islands, BAP—Barbados accretionary prism, TBR—Tobago-Barbados Ridge. Individual islands: Gu—Guadeloupe, Ma—Martinique, Gr—Grenada, Bb—Barbados, Tb—Tobago, May—Mayreau, Car—Carriacou; Ld—La Désirade; Do—Dominica. (Allen et al., 2019).

The Arc forms an 800-km-long curve from Grenade to Anguilla, mostly north-south orientation (Schlaphorst et al., 2021). In the north, it is curved to the Greater Antilles and in the south to the South American continent. A back arc basin (Allen et al., 2019, 2019; Bouysse, 1988; Padron C., 2020) called Grenada basin is located westwards of the arc, which border is build up by the Aves Ridge, an ancient Mesozoic volcanic arc (Boynton et al., 1979; Christeson et al., 2008).

Nowadays the volcanic arc consists of 11 islands plus the smaller Grenadine islands between St. Vincent and Grenada. Northern to Dominica, the arc is separated into two parts: the eastern inactive - (the Limestone Caribbees) and the western active (the Volcanic Caribbees) part. Guadeloupe is situated in between these two sections, with the same subdivision (Schlaphorst et al., 2021).

The Eastern part is of the so-called outer arc, its volcanic basement is buried under sediments of the Barbados accretionary prism (Allen et al., 2019). The curved form of the outer arc infer that there had been an increased strike-slip movement toward the north (DeMets et al., 1994; DeMets et al., 2000).

2.2.1 Regional setting

According to Burke (1988) and Pindell et al. (1988) the oceanic crust of the Caribbean plate has its origins in the Eastern Pacific. During the break-up of Pangea between ~200 and ~135 My the Central Atlantic and Proto-Caribbean oceans opened due to the rifting and drifting from Africa and South America away from North America (Boekhout et al., 2012; González, 2001; Litherland, 1994; Noble et al., 1997; Pindell and Kennan, 2009; Villagómez, 2008).

West-dipping subduction of this Proto-Caribbean lithosphere by the Caribbean plate along the evolving Great Arc of the Caribbean (GAC) started between 135 – 110 My (Boschman et al., 2014; Burke, 1988; Escuder-Viruete et al., 2013; Hastie and Kerr, 2010; Mann et al., 2007; Neill et al., 2012; Pindell and Kennan, 2009) and is illustrated in Figure 3a. It spanned the full length of the Proto-Caribbean, but also parts of the North and South American margins and formed an increasingly curved arc. Figure 4a shows this arc migration facilitated the forming of the back-arc basins ~70 and 50-60 My, the Yucatán basin along the northern GAC (Pindell, 2009) and the Venezuelan basin behind the west-facing subduction below the Aves Ridge in the south (Allen et al., 2019).

At the Caribbean plate itself, a short-lived magmatic event took place between 91 and 88 My (Hauff et al., 2000; Hoernle et al., 2002; Kerr et al., 1997; Révillon et al., 2000; Sinton et al., 1997; Sinton et al., 1998) when passing the plume-head of the Galápagos hotspot (Duncan and Hargraves, 1984; Hill, 1993). These flood basalts formed a major oceanic plateau, the Caribbean Large Igneous Province (CLIP) (Burke et al., 1978; Burke, 1988; Saunders et al., 1996).

The separation of South America and Africa around 90 My initiated the opening of the Equatorial Atlantic and stopped the spreading ridge of the Proto-Caribbean shortly after that event (70My) (Figure 3b). Divergence between the North and the South American plate stopped. When the northern part GAC collided with the North American margin between 60 and 50 My, the subduction of this part ceased and changed the former north-easterly convergence direction of the southern GAC, the Aves Ridge, to easterly direction. This allowed the Caribbean plate to move eastward relative to North America along the Cayment ridge-transform boundary (Braszus et al., 2021).

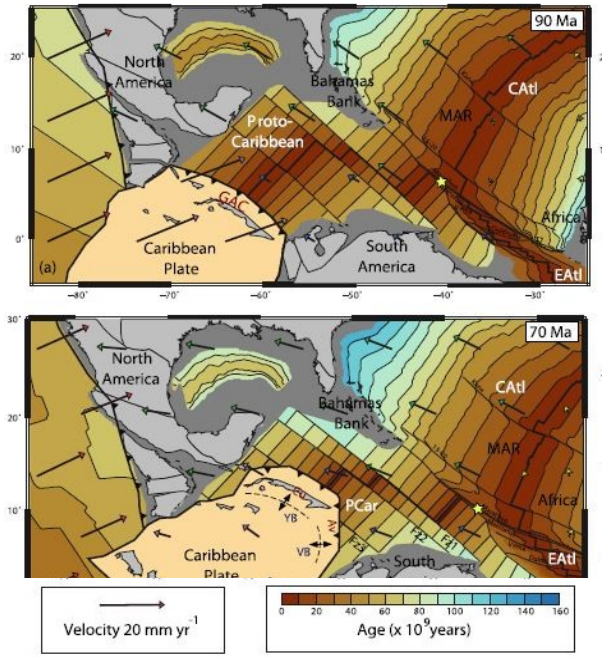

Figure 3: Plate configurations Upper Cretaceous to Oligocene in the Caribbean sea. Reconstruction from (Müller et al., 2019) with modifications from (Braszus et al., 2021). Proto-Caribbean—PCar, Central Atlantic—CAtl, Equatorial Atlantic, EAtl) meet. MAR—Mid-Atlantic Ridge.

According to Allen et al. (2019), a slab roll-back of the subducted lithosphere led to the extinction of Aves Ridge 59 My years ago. This implied upper-plate extension and formed the Granada back-arc basin. At the same time a new outer arc was formed between 40 and 25 My, the Outer Antillean Arc (Figure 4b). Today, only the northern part of this is exposed in the Limestone Caribbees.

Shallowing of the slab around 25 My migrated the arc westward back into its own back-arc basin to form the Lesser Antilles Arc (LAA), which is illuminated in Figure 4c. Another back-arc basin formed called the Tobago basin. The back arc- and forth-arc jump is externally driven by the interaction between the Caribbean and adjacent North and South American plates (Allen et al., 2019).

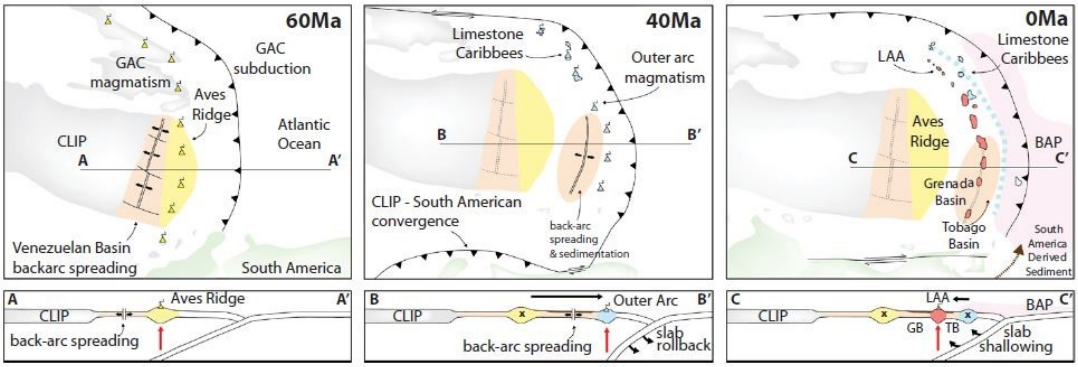

Figure 4: New tectonic model for the eastern Caribbean region. Locations of key tectonic blocks are based upon the reconstruction of Boschman et al. (2014). GAC - Great Arc of the Caribbean, CLIP—Caribbean large igneous province, LAA - Lesser Antilles arc (LAA), TB - Tobago Basin, GB - Grenada Basin, BAP - Barbados accretionary prism (Allen et al., 2019).

2.3 Volcanological background

The activity of recent arc since the upper Pliocene (Bouysse et al., 1990) formed the island of Basse-Terre. It consists out of 7 main eruptive fields: the Basal Complex, the Northern Chain, the Axial Chain, the Chaîne de Bouillante, the Monts des Caraïbes, the Trois-Rivières-Madeleine complex and the active Grande Découverte-Soufrière massif, illustrated in Figure 5. La Soufrière de Guadeloupe is part of the last one, which originated in the last 445.000 years, comprising three stratovolcanoes: Grand Découverte, Carmichael and Soufrière (Komorowski et al., 2005).

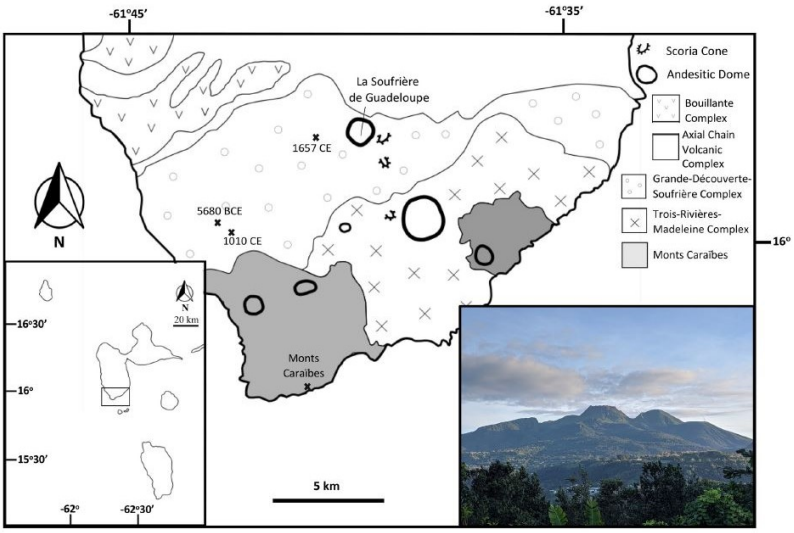

Figure 5: Map of Basse-Terre showing the location of the volcano La Soufrière, volcanic complexes and location of each eruption (Metcalfe et al., 2022).

La Soufrière is a basaltic-andesite to andesitic arc volcano and the most recent volcano on the island. Its history started 7.140 years ago, with both, magmatic and phreatic eruptions (Komorowski et al., 2005; Komorowski et al., 2013a; Komorowski et al., 2013b; Legendre, 2012). The latest magmatic eruption in 1530 CE caused a collapse of the complex, with a landslide which reached the 10 km far away coast. Ash, pumice fallout, pyroclastic flows and mud flows reached an area 5-7 km from the volcano (Boudon et al., 2008; Komorowski et al., 2008). The present dome formed during that event.

Non-magnetic steam-driven (phreatic) eruptions occurred in 1797–1798, 1812, 1836–1837, 1976–1977, minor ones in 1690 and 1956 (Hincks et al., 2014; Komorowski et al., 2005; Legendre, 2012; Lherminier, 1837c, 1837b, 1837a). The most violent phreatic eruption in 1976-1977 with 26 non-magmatic explosions forced the evacuation of 73.000 people for up to 6 months (Boudon et al., 1988b; Feuillard et al., 1983; Komorowski et al., 2005).
A strong seismic unrest event, interpreted as a failed phreatic eruption (Moretti et al., 2020), took place in 2018 and raised concerns for the stability of the southwest flank of the dome.

The hydrothermal activities are caused by the underlaying magmatic body, 5-8 km beneath the dome (Figure 6). Acid sulfate-chlorite springs and degassing of the magma chamber supply hot acid fluids and CO_2, SO_2, H_2S, HCl and HF to the hydrothermal system (Villemant et al., 2005; Villemant et al., 2014). Acid-chloride-sulfate hydrothermal fluids which have its source in andesitic system are characterized by either propylitic alteration (Taran and Kalacheva, 2020) or intermediate to advanced argillic alteration (Heap et al., 2021). Especially the shallow area show advanced argillic alteration, which developed due to the circulation of cooled (150°C – 350°C), acidic (pH < 4) fluids, possibly mixed with meteoric waters (Heap et al., 2021).
These fluids are transported to the summit fumaroles and circulate through the dome structure along listric discontinuities that drain to the southwest (Brombach et al., 2000; Rosas-Carbajal et al., 2016; Salaün et al., 2011; Villemant et al., 2014).

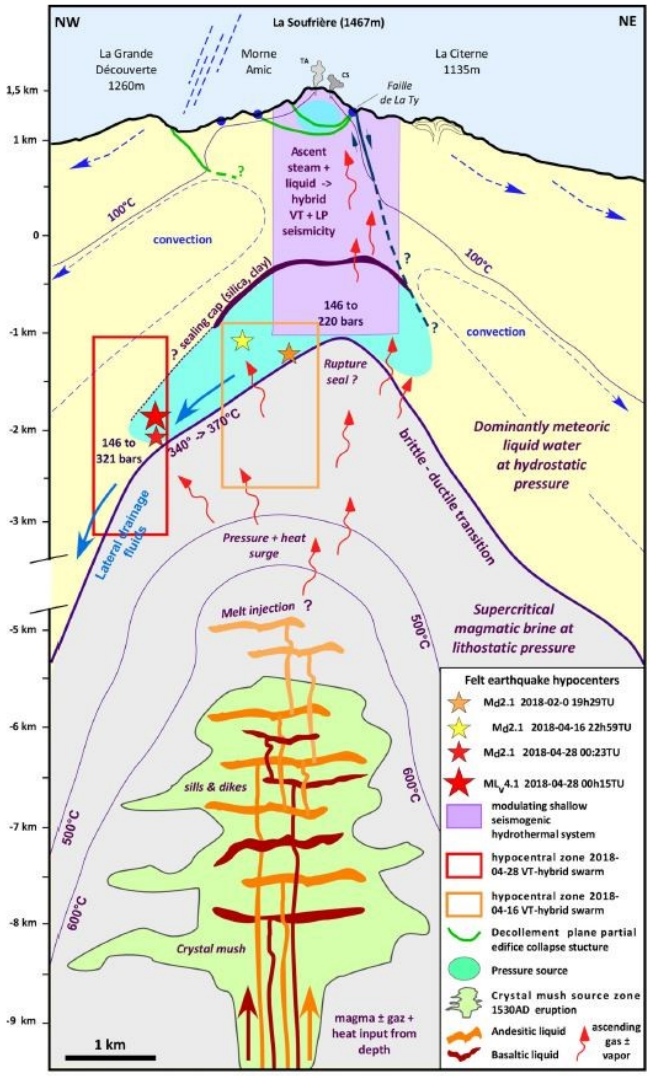

Figure 6: Conceptual model of La Soufrière de Guadeloupe and the 2018 unrest episode with its located epicenters between 1 and 3 km depths (Moretti et al., 2020)

The recent observed shallow deformations and seismic activities are the result of this shallow hydrothermal system. Deeper and higher activities are related to the increase of pore pressure response to the arrival of hot magmatic fluids along faults inside the dome structure (Moretti et al., 2020).

3 Samples

For further analysis and classification of the altered soil like material of the volcano La Soufrière de Guadeloupe, ten samples have been taken in May 2022. The exact position where confirmed, is given in Table 1.

Table 1: Coordinates of the samples (WGS84)

Sample	Longitude	Latitude	Height [m]
KSL_2	-61,663024	16,044068	1442
KSL_4	-61,663101	16,043270	1436
KSL_5	-61,663781	16,043723	1446
KSL_7	-61,662966	16,044002	1442
KSL_8	-61,66291	16,04403	1442
KSL_9	-61,662888	16,044025	1442
KSL_10	-61,660177	16,044768	1287
KSL_11	-61,661775	16,038378	1154
KSL_12	-61,661775	16,03837	1150
KSL_13	-61,661716	16,038149	1145

Sampling was chosen to ensure a wide range of samples with varying degrees of alteration. Shown in Figure 7, KSL_4 and KSL_5 are directly from the death zone surrounded by already dead vegetation associated with large, active fumaroles (Cratère sud and Gouffre Tarissan, respectively). Position KSL_7 is located in the proximity of a small active fumarole. KSL_2, KSL_8 and KSL_9 are still partially surrounded by living and dying plants.

Figure 7: Overview of the sampling (May 2022)

But not just the top area of the summit was sampled but also a landslide which occurred in the last couple of years (KSL_10) and material from a normal fault (Faille la Ty) in south direction to the summit (KSL_11-KSL_13) (Figure 8).

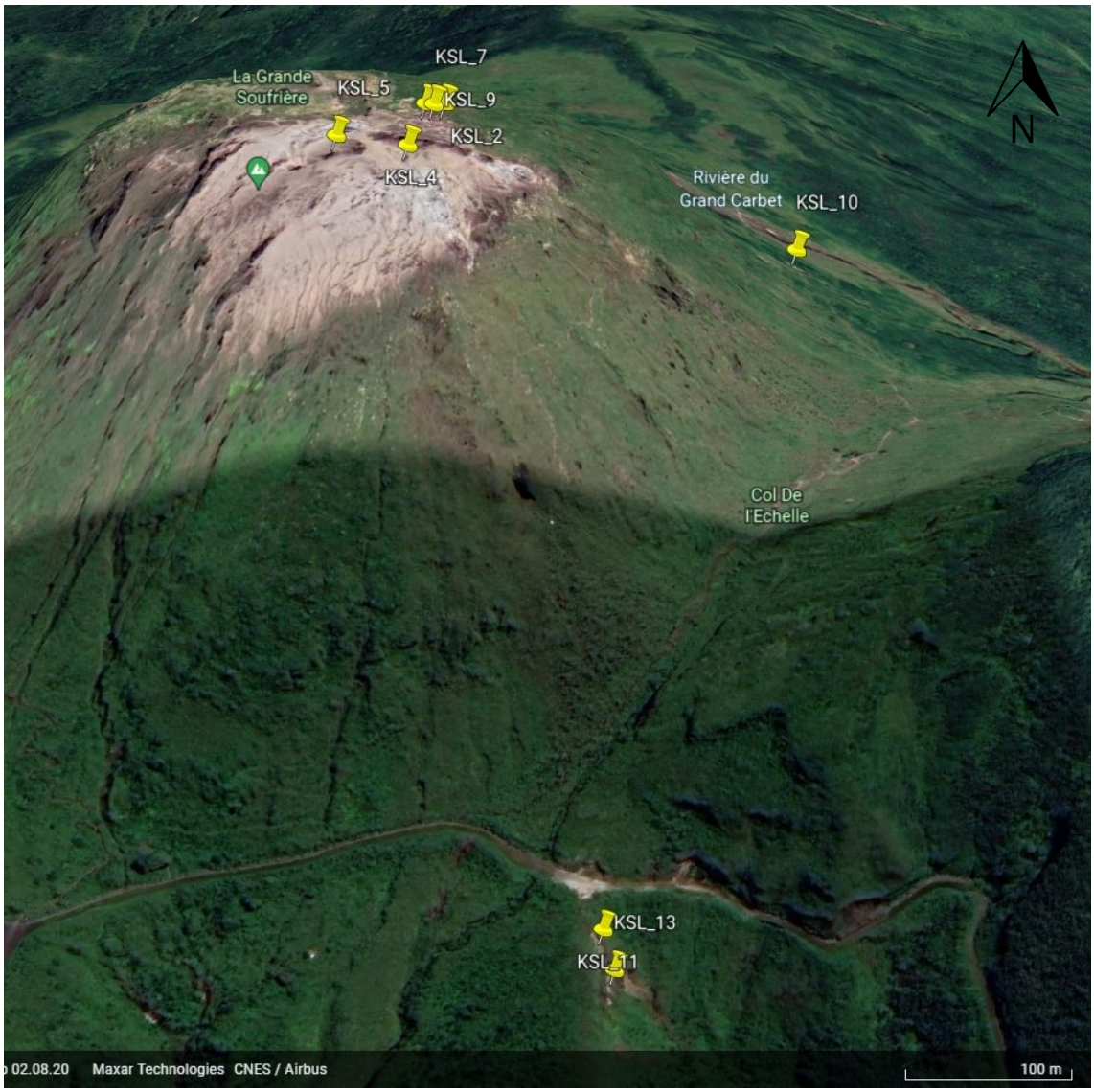

Figure 8: Positions of samples on map (www.earth.google.com; 06.01.2022)

3.1 Macroscopic analysis

For sampling either a circular cylindrical - sampler (diameter ~150 mm) or a trowel were used. The sampling depth ranged from 0 cm to 20 cm below the surface. The samples were wrapped with multiple layers of plastic wrap for transport off the volcano and to the laboratory in Austria. The samples were stored in a climate chamber in the laboratory at room temperature and 99% humidity to preserve the in-situ conditions of the material as much as possible. They have been unwrapped shortly before the shear test on a 43,3 x 29,3 cm platter.

3.1.1 KSL_2

KSL_2 was taken close to the border of the dead zone (Figure 9 and Figure 16). There is still some vegetation growing, but it's close to an active funnel.

Figure 9: KSL_2 next to a funnel but nearby growing vegetation (May 2022).

The material of this cake sample was brownish fine-grained material which was stuck together to bigger solid pieces of residual rock. Some areas in between remained greyish, as you can see on Figure 10. It was very dry and friable, which made the preparation difficult. The sample was taken from 30 – 50 mm depth.

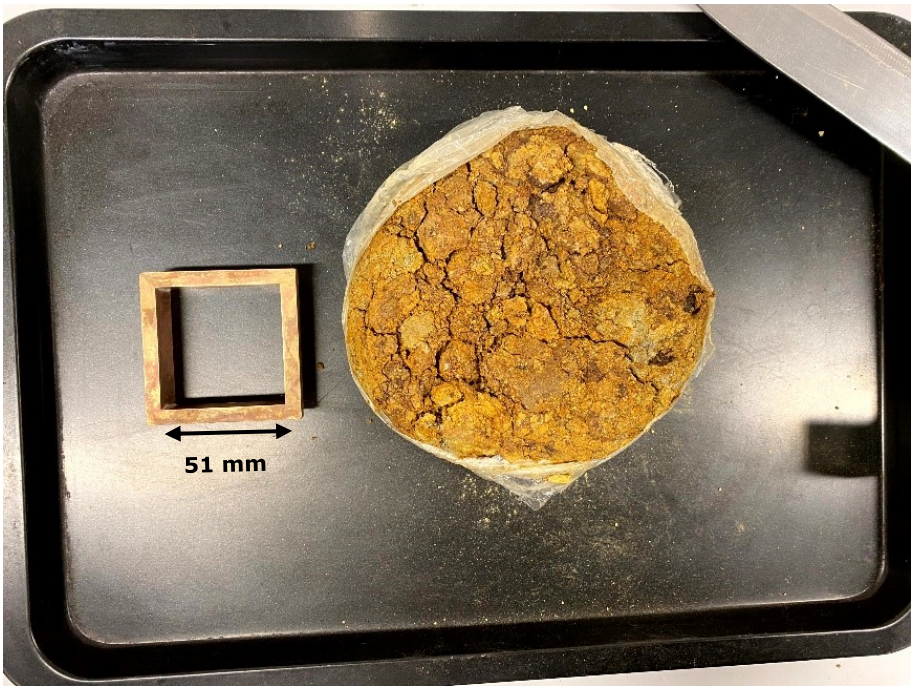

Figure 10: Cake sample KSL_2 (20.09.2022).

3.1.2 KSL_4

Close to the Cratère Sud, this dry, not very friable cake sample was cut from the top to ~100 mm depth out of the ground. There are no active fumaroles in closer surroundings, neither are growing plants nearby (Figure 11).

Figure 11: Cake sample KSL_4 close to the Cratère Sud (May 2022).

The material itself was dry and brittle when unwrapping it. The brownish, fine grained material had grey clay lenses in between, which were stuck together with the rest of the sample. The brittleness made it hard to handle with the material. As shown in Figure 12, the brown parts are very crumbling and weak.

Figure 12: Cake sample KSL_4 (19.09.2022).

3.1.3 KSL_5

Like KSL_4, KSL_5 had been taken on the top of La Soufrière. No vegetation was close to it and the material seemed very influcened by the activity of the volcano. The cake sample compromise from the top to a depth of ~200 mm from the ground. It was very clamp and not friable as the samples before. Also the material was sensitive to remolting.
The brown material was sticky and very fine grained, so it was easily to cut with a knife. Grey, more fine grained lenses appeared in the coarser grained brown fraction, shown in Figure 13.

Figure 13: Cake sample KSL_5 with grey lenses inside of the brown sticky material (27.07.2022).

3.1.4 KSL_7

This sample derived from a very active zone close to a small fumarole. Shown in Figure 14, the surrounding is greyish with no vegetation and clear precipitation of sulfur. The cake sample includes the topsoil to a depth of ~150 mm, where the temperature was so hot that it melted the sampler.

Figure 14: Surrounding area of KSL_7 (May 2022).

The top of it was friable and rocky and gets clayey in bottom direction. On the base of it there are sulfur crystals in the grey to black clayey material, which you can see in Figure 15a and b.

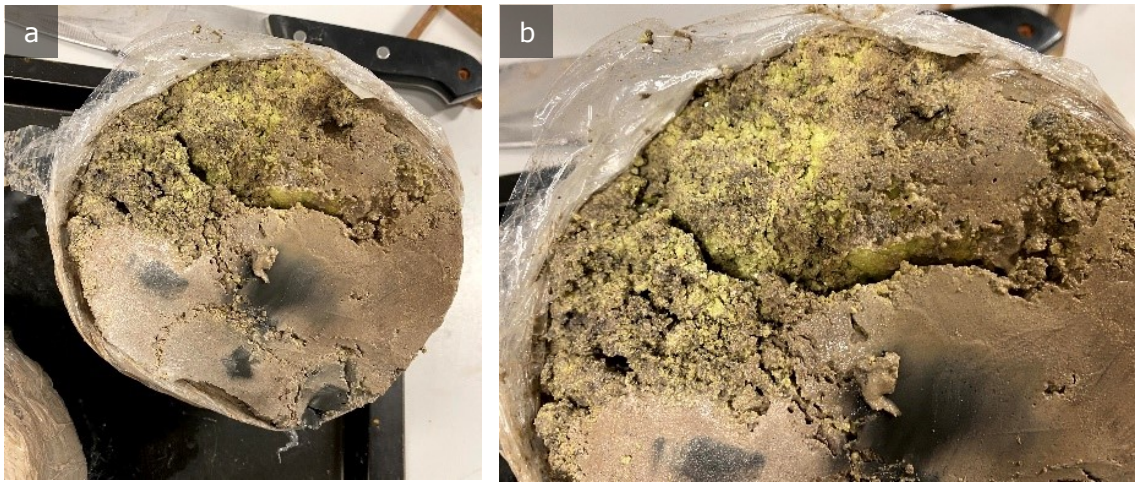

Figure 15: Cake sample KSL_7 (a) with sulfur crystals inside the grey clayey material (b) (20.09.2022).

3.1.5 KSL_8

To ensure a wide range of samples with varying degrees of alteration, samples KSL_2, KSL_8 and KSL_9 were taken in decline direction of the influence of the hydrothermal alteration (see Figure 16). KSL_8 is in between the other ones and close to a small fumarole.

Figure 16: Sample positions of KSL_2, KSL_8 and KSL_9 (May 2022).

The trowel sample reached from the topsoil to ~20 mm depth. It was moderately wet with a little vegetation in it, but not enough to pretreat the sample. The brown, sticky and silty material has darker browner areas in between which seemed more clayey.

Figure 17: KSL_8 from bird view (a) and front view (b) (22.09.2022).

3.1.6 KSL_9

This very stiff and brittle, dark grey sample derived from the border where live vegetation starts again (see Figure 16 and Figure 18). It was taken with a trowel.

Figure 18: Sample KSL_9 with still some growing vegetation in proximity (May 2022).

The dark brown soil has brown altered zones in between. The sandy to clayey sample was dry with no sticky lenses. Due to its stiffness it was hard to prepare and cut. A picture of KSL_9 is shown in Figure 19.

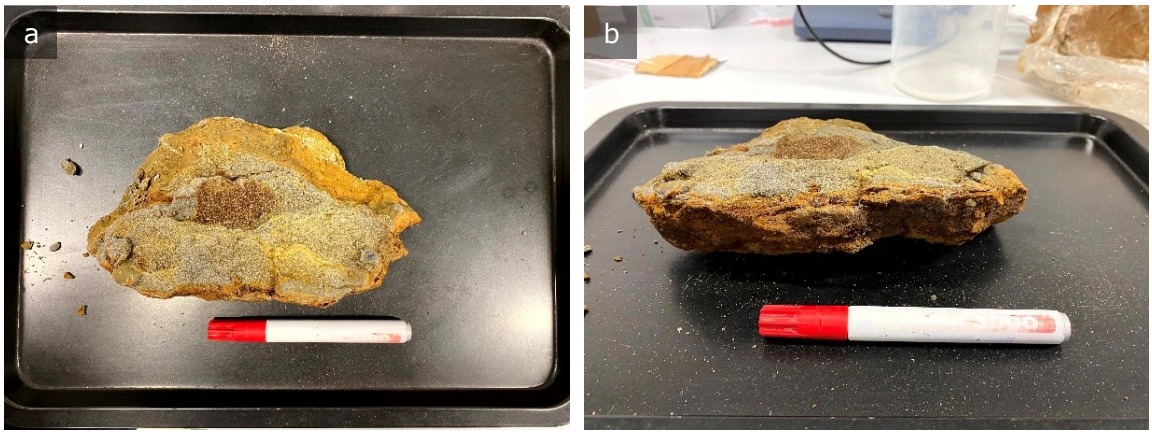

Figure 19: KSL_9 from bird view (a) and front view (b) (22.09.2022).

3.1.7 KSL_10

KSL_10 derived from a meanwhile inactive, previously altered area ~15 m south of the landslide side scarp on a walking track, shown in Figure 20.

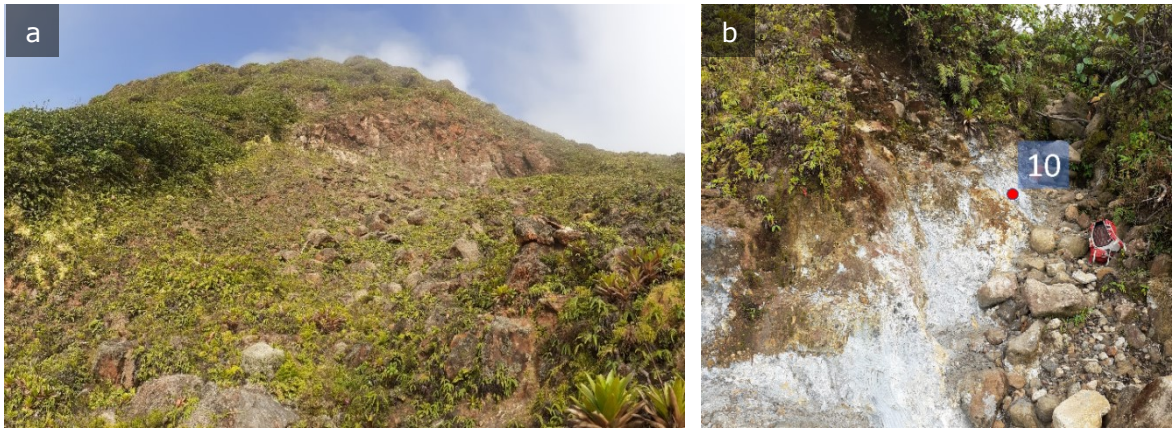

Figure 20: (a) Landslide scarp; (b) Sampling position of remolded, greyish, clayey material of the landslide (KSL_10) (May 2022).

There are still some relict textures visible, shown in Figure 21. The sample consists of very soft grey clay with brown alteration zone in between them. There are no coarser fractures in it. White layers follow the texture which seems to be the shear movement.

Figure 21: Overview picture of KSL_10 (14.07.2022).

3.1.8 KSL_11

Three samples, including KSL_11 were taken from a fault south-east of the summit of La Soufrière de Guadeloupe. Shown in Figure 21 is the surrounding area with a lot of vegetation, except in the fault itself. The fault contains active fumaroles.
The short axis of the trowel sample showed towards the slope and the long axis parallel to the slope.

Figure 22: KSL_11 - KSL_13 are taken from a normal fault in south direction to the summit (May 2022).

KSL_11 looked a lot different than the samples before. Shown in Figure 23, its color was lighter and kind of cream with light brown and greener zones in between. No coarser grains were visible. There were pieces of organic in it but not enough to pretreat the sample. The consistency is pretty crumbly, which makes the handling with the sample a bit difficult.

Figure 23: Trowel sample KSL_11 from bird's view (a) and side view (b) (23.09.2022).

3.1.9 KSL_12

This block sample was taken close to the position of KSL_11 (see Figure 22). Looking like an intact rock, the sample was cuttable with a knife. The inner material was grey and clayey, with a high strength Figure 24b. The outside was covered with roots and organics, which made pretreating for further tests necessary. There were no visible components in the material.

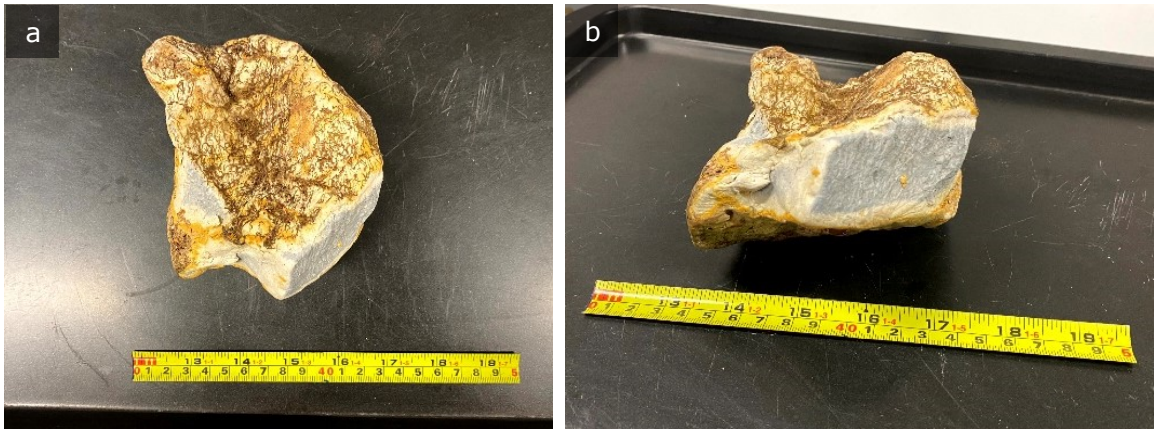

Figure 24: Roots and organic (a) are all over altered block sample (b) (26.09.2022).

3.1.10 KSL_13

The position of this KSL_13 is shown in Figure 22. The sampling was oriented, with its short axis towards the slope and the long axis parallel to the slope.
The first thing that is noticeable about this trowel sample is its light weight. It turned out that this will bring some problems for the following tests.
The color is close to the sample KSL_11, which is very light with altered grey zones in between, as you can see in Figure 25. The difference is that KSL_13 is finer grained and feels like skin cream when deformed between the fingers. There are no coarser grains visible.

Figure 25: KSL_13 turned out very brittle and remarkably light weight (27.09.2022).

4 Analytical methods

To get results that cover the area of the summit with different alteration age, ten samples were taken. The samples were analyzed with analytical methods and geotechnical measurements. They are described in this chapter.

4.1 Direct shear test on in situ samples

The shear strength τ_f is an important parameter in soil mechanics. From the determined parameters of the shear strength τ_f of a soil, fracture processes or failure modes of the soil can be calculated.
The general concept of shear strength τ_f is the resistance that a given solid body activates against an applied shear stress. After exceeding the maximum shear strength τ_f, the failure of the solid follows (ÖNORM EN ISO 17892-10, 2019).

In addition to the shear strength of a soil, the residual shear strength τ_r is the minimum (constant) shear stress that occurs after the maximum shear stress is reached with increasing shear displacement. The residual shear strength is the value that occurs (in cohesive soils) after very large displacement and placement of the clay minerals. If, after an increase in shear stress, a continuous maximum shear stress occurs or does not decrease during the shear test, this soil has no (characteristic) residual shear strength (ÖNORM EN ISO 17892-10, 2019).

The behavior at failure of a soil body is defined by the fracture condition according to Mohr Coulomb. The fracture line (failure envelope) represents the maximum effective shear stress τ_f' in a sliding surface, according to a certain effective normal stress σ'. The slope of the straight line is equal to the effective friction angle φ'. The point at which the straight line intersects the shear stress axis τ' is called the effective cohesion c'. To represent the fracture line, it is necessary to determine the maximum effective shear stresses τf' for three different effective normal stresses (Schmitt et al., 2021).

The Mohr-Coulomb failure criteria is defined by the effective normal stress σ’ and the occurring shear stress τ according Equation 1 (Schmitt et al., 2021):

Equation 1: $$\tau_f = c' + \sigma' * tan\varphi$$

τ_f	shear strength	[kN/m²]
c’	effective cohesion	[kN/m²]
φ	effective friction angle	[°]

In order to be able to determine effective shear parameters, three to four consolidated - drained test (CD test) were done. In the consolidated drained test conditions, an open system is present. The open system allows the pore water in the soil sample to escape, provided that the shear test is run "slowly" according to the soil sample. This is ensured by a water-permeable design of the shear apparatus and

a correspondingly "slow" shear rate. As a result, only effective stresses occur, since no pore water pressures are built up.

For the direct shear test a shearbox apparatus of dating from 1981 was modified, as shown in Figure 26. The apparatus was equipped with digital measuring instruments. Two Linear Variable Differential Transformers (LVDT) (model WA10, constructed by HBM) in vertical and horizontal direction were installed to determine the shear displacement and the settlement of the sample in the shear box.

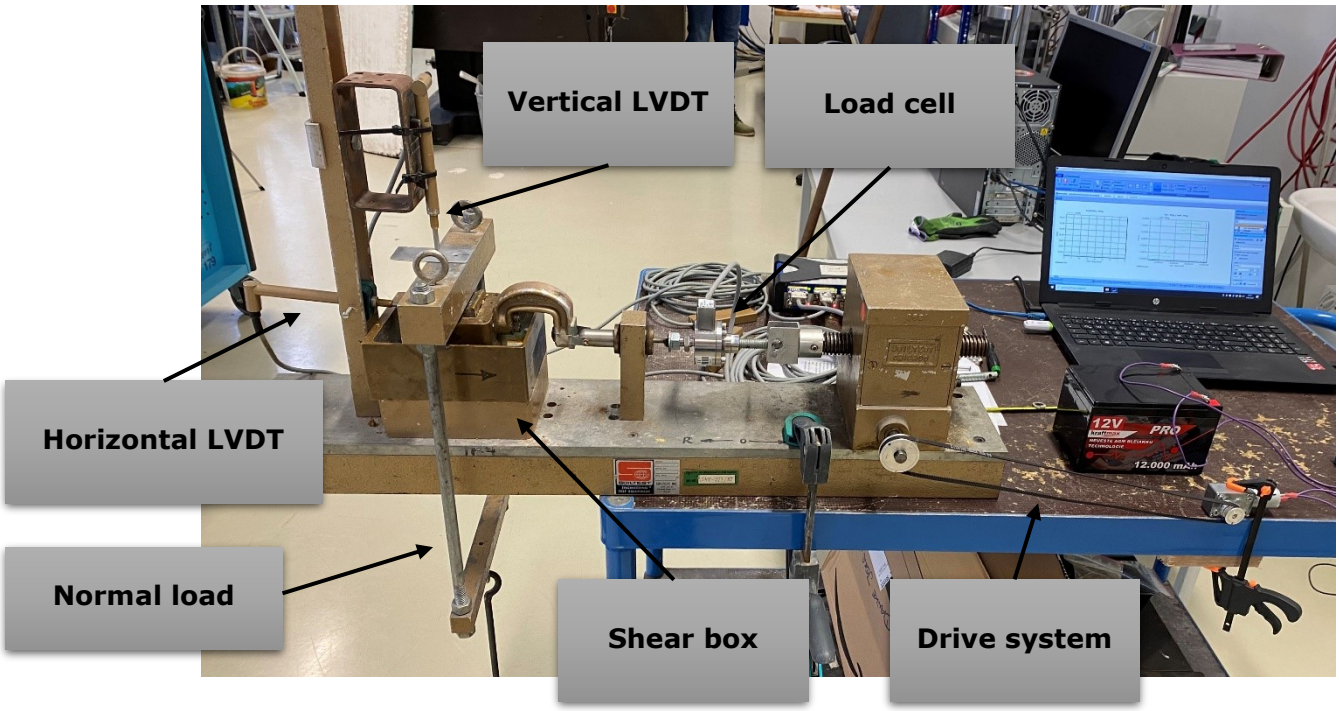

Figure 26: Device setup for the direct shear test.

Furthermore, a load cell (U2A 50kg, accuracy class 0,2 constructed by HBM) was added to measure the required shear force. A motor powered by a car battery driving a gear drive set the rotation time to one revolution per minute. This should avoid building up pore water pressure.
The software used for the measurements was CatmanEasy-AP from HBM.
The test was carried out according to the ÖNORM EN ISO 17892-10: Direct shear tests.
The in situ samples were put into the shear box and consolidated with a force between 60 - 200 N. The vertical settlements were measured and after the pore water was completely squeezed out, the shear test was done. Three to four measurements for each sample were conducted. In consideration of the mass of frame and the correction of the horizontal friction, the cohesion and the friction angle were calculated with Equation 1.

4.2 Particle size distribution

For the classification of soils samples, the particle size was determined by the combination of sieving and sedimentation (hydrometer test) according to the "ÖNORM EN ISO 17892-4: Determination of the particle size distribution".

4.2.1 Sieving

Both dry and wet sieving were done, depending on the state of the sample. The sizes of the sieves used were 4 mm, 2 mm, 1 mm, 425 µm, 250 µm, 125 µm and 63 µm. The minimum mass was calculated with Equation 2 and yield 160 g.

Equation 2:

$$m_{min} = \left[\frac{D_{max}}{10}\right]^2$$

m_{min}	..... minimum mass	[g]
D_{max}	..... maximum particle diameter	[mm]

A mechanical sieve shaker separated 10 minutes the different grain sizes. The residues on the sieves were weighted and converted into percentage of the total dry weight, using Equation 3. Afterwards a grain distribution line was created.

Equation 3:

$$f_n = 100\% - \left[\frac{m\prime_{ss1} + m\prime_{ss2} + \cdots + m\prime_{ssn}}{m} * 100\%\right]$$

f_n	..... fraction passing the given sieve size	[%]
$m'_{ss1} + m'_{ss2}$	..... masses of soil retained	[g]
m	..... total dry mass	[g]

According to ÖNORM EN ISO 17892-4 (2017), one sample was pre-treated with hydrogen peroxide (20% V/V) to remove the organic material. Also, a dispersing agent for this one was needed, so 4 g/l of hexa-sodium hexametaphosphate, were used.

4.2.2 Hydrometer method

The fraction of each sample which passed the 63 µm sieve was collected and dried at 65°C again. 25 g were combined with 40 g/l hexa-sodium hexametaphosphate dispersing agent, and mixed four hours in a mechanical shaker with 7,5 revolutions per minute (ÖNORM EN ISO 17892-4, 2017).
Hydrometer readings were taken after 30 s, 1 min, 2 min, 4 min, 8 min, 30 min, 1 h, 2h, 6h and 24h.
Using Stoke's law from Equation 4, the equivalent particle diameter can be calculated.

Equation 4: $$d_i = 0{,}005531 * \sqrt{\frac{\eta * H_r}{(\rho_s - \rho_w) * t}}$$

d_i	equivalent particle diameter	[mm]
η	dynamic viscosity of water	[mPa*s]
H_r	effective depth of hydrometer	[mm]
ρ_s	particle density	[Mg/m³]
ρ_w	density of sedimentation fluid	[Mg/m³]
t	time elapsed from start of sedimentation	[min]

4.2.3 Particle size distribution

For the classification of the soil like material, the grain size distribution was plotted in a diagram, on its x-axis the grain size [mm] and y-axis percentage that passed [%]. The particle diameters that passed at 10%, 30% and 60% were evaluated. With these values, the coefficient of uniformity U and coefficient of curvature Cc could be calculated according to Equation 5 and Equation 6.

Equation 5: $$U = \frac{d_{60}}{d_{10}}$$

Equation 6: $$Cc = \frac{{d_{30}}^2}{d_{10} * d_{60}}$$

U	coefficient of uniformity	[]
Cc	coefficient of curvature	[]
d_n	diameter where n-% of the material passes through	[mm]

The classification of the uniformity following González de Vallejo and Ferrer (2011) interpretates that if U is less than 5, the soil has a uniform grain size. A U between 5 and 20 can be interpretated as slightly uniform, and a U > 20 that it is a well-graded soil.
The coefficient of curvature gives information about the course of the sieving line. A widespread and therefor well-graded sand is defined with Cc = 1-3 and U > 6, in contrast to a narrow-stepped and poorly graded one with Cc = <>1-3 and U < 6. Gap in graded soils can be interpreted as lack of grains in a particular size range and they cause steps in the curve. In this case the values for U > 6 and Cc <>1-3.

The classification is made according to the United Soil Classification System (USCS) in Figure 27.

Major divisions (1)	Subdivisions (2)	USCS symbol (3)	Typical names (4)	Laboratory classification criteria (5)	
Coarse-grained soils (More than 50% retained on No. 200 sieve)	Gravels (More than 50% of coarse fraction retained on No. 4 sieve)	GW	Well-graded gravels or gravel-sand mixtures, little or no fines	Less than 5% fines*	$C_u \geq 4$ and $1 \leq C_c \leq 3$
		GP	Poorly graded gravels or gravelly sands, little or no fines	Less than 5% fines*	$C_u < 4$ and/or $1 > C_c > 3$
		GM	Silty gravels, gravel-sand-silt mixtures	More than 12% fines*	Minus No. 40 soil plots below the *A*-line
		GC	Clayey gravels, gravel-sand-clay mixtures	More than 12% fines*	Minus No. 40 soil plots on or above the *A*-line
	Sands (50% or more of coarse fraction passes No. 4 sieve)	SW	Well-graded sands or gravelly sands, little or no fines	Less than 5% fines*	$C_u \geq 6$ and $1 \leq C_c \leq 3$
		SP	Poorly graded sands or gravelly sands, little or no fines	Less than 5% fines*	$C_u < 6$ and/or $1 > C_c > 3$
		SM	Silty sands, sand-silt mixtures	More than 12% fines*	Minus no. 40 soil plots below the *A*-line
		SC	Clayey sands, sand-clay mixtures	More than 12% fines*	Minus No. 40 soil plots on or above the *A*-line
Fine-grained soils (50% or more passes the No. 200 sieve)	Silts and clays (liquid limit less than 50)	ML	Inorganic silts, rock flour, silts of low plasticity	Inorganic soil	PI < 4 or plots below *A*-line**
		CL	Inorganic clays of low plasticity, gravelly clays, sandy clays, etc.	Inorganic soil	PI > 7 and plots on or above *A*-line**
		OL	Organic silts and organic clays of low plasticity	Organic soil	LL (oven dried)/LL (not dried) < 0.75
	Silts and clays (liquid limit 50 or more)	MH	Inorganic silts, micaceous silts, silts of high plasticity	Inorganic soil	Plots below *A*-line
		CH	Inorganic highly plastic clays, fat clays, silty clays, etc.	Inorganic soil	Plots on or above *A*-line
		OH	Organic silts and highly plastic organic clays	Organic soil	LL (oven dried)/LL (not dried) < 0.75
Peat	Highly organic	PT	Peat and other highly organic soils	Primarily organic matter, dark in colour, and organic odor	

C_u (coefficient of uniformity) = D_{60}/D_{10}; C_c (coefficient of curvature) = $(D_{30})^2/(D_{10} \times D_{60})$.
* "Fines" are those soil particles that pass the No. 200 sieve. For gravels and sands with between 5 and 12% fines, use of dual symbols is required (i.e., GW-GM, GW-GC, GP-GM, or GP-GC).
** If $4 \leq PI \leq 7$ and PI plots above *A*-line, then dual symbols (i.e., CL-ML) are required.

Figure 27: United Soil Classification System (González de Vallejo and Ferrer, 2011).

4.3 Atterberg limits

For better classification, the liquid and the plastic limit of the soil samples were determined according to the ÖNORM EN ISO 17892-12: Determination of liquid and plastic limit.

4.3.1 Water content

Based on the assumption that there are different clay minerals in the sample, which destruction should be avoided with excessive heating, the samples were dried at 65°C until mass constancy.
The sample was weighed before and after the drying. The water content was determined according Equation 7.

Equation 7:
$$w = \frac{m_w}{m_d} * 100$$

m_w ..... mass of water [g]
m_d ..... dry mass sample [g]
w ..... water content [%]

4.3.2 Casagrande method

The water content at which the soil changes from liquid to plastic is called the liquid limit (w_L) and was measured with the Casagrande method. Therefore 200 g of the soil fraction <425 µm of the sample were used. After adding distilled water, the paste was put into a cup with a depth of at least 10 mm at its deepest point. A groove was cut in the soil paste. After that the cup was raised to a specific high by a cam and

then dropped on the base. The cam should be operated with 2 revolutions per second. The drops of the cup until the groove was closed over a length of 10 mm were recorded. Afterwards the water content was determined (ÖNORM EN ISO 17892-12, 2021).
Four tests of each sample were made and the liquid limit at 25 rotations was detected.

4.3.3 Plastic limit test

The water content at which the soil ceases to be plastic when dried further is called the plastic limit (w_P). Therefore 15 to 20g of the <425 µm fraction of the samples were used. After adding distilled water, the paste was put on a mixing plate and rolled backwards and forwards until the diameter approaches 3 mm. The procedure was repeated until it started crumbling at this diameter. At least 6 g at this point were collected and the water content determined.

4.3.4 Plasticity index

With the liquid and the plastic limits, the plasticity index (I_P) can be calculated according to Equation 8:

Equation 8: $$I_p = w_L - w_P$$

w_L ..... liquid limit [%]
w_P ..... plastic limit [%]

It represents the moisture content interval for passing from a semi-solid to a semi-liquid state. With this value, a classification according to the Casagrande plasticity chart was done. It is shown in Figure 28. The A-line defines various zones with organic content below the line while clays are found above it. According to Casagrande, soils with liquid limit above 50 % have high -, the one <50 % low plasticity.

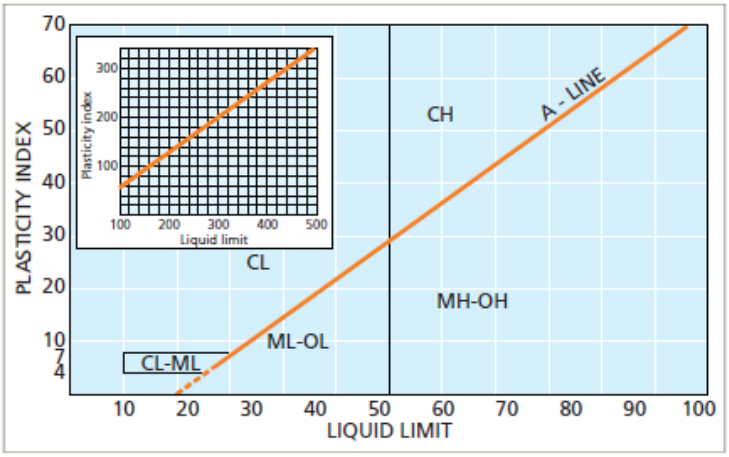

Figure 28: Casagrande plasticity chart: CL=clays with low plasticity; CH=clays with high plasticity; ML-OL=silts and organic soils with low plasticity; MH-OH=silts and organic soils with high plasticity (González de Vallejo and Ferrer, 2011)

4.4 pH-value

An eluate according to ÖNORM EN 14997:2015-03 with the ratio liquid and solid 10 l/kg and the grain size of <10 mm was produced. The pH value was determined with WTW inoLab pH 7110.

4.5 Grain density

For further evaluations on the grain size, the grain density was determined with Anton Paar Ultrapyc 5000 helium pycnometer. Gas pycnometers are based on the fact that the solids to be measured displace their volume of a test gas in a sample chamber. This difference in the volume of the test gas compared to the empty sample chamber or a reference chamber is measured. Helium was used as a test gas.

4.6 X-ray diffraction analysis

To further analyze the mineral composition of the samples X-ray diffraction (XRD) was conducted on the samples. The measurements were done by the Technical University of Munic. The method is the powder-diffractometry, a destructive method where the sample is converted into powder for further analysis (Rietveld, 1969).

4.7 X-ray fluorescence spectrometry

X-ray fluorescence analysis (XRF) is a non-destructive analytical method for determining the chemical composition of a wide variety of materials. These can be in powder form, as solids or as liquids. Generally, concentrations ranging from ppm range up to 100% are analyzed (Brouwer, 2006).
The sample is exposed to X-rays of known wavelength and energy. As soon as it hits an element of the sample, a X-ray photon is emitted. The energy is characteristic for each atom. Together in the spectrum, an element can be identified (Brouwer, 2006).

The same samples that have been used for the other measurements were crushed in a vibrating mill to a homogeneous powder. Then the sample was heated and pressed into a tablet together with lithium-tetraborate, which acted as a flux substance. The XRF spectrometry was conducted with a wave dispersive PANALYTICAL Axios max advanced at the Chair of Geology and Economic Geology at Montana university Leoben.

5 Results

In the following results of the various methods to analyze the samples are presented.

5.1 Evaluation of the direct shear test

The direct shear test was done on all samples under in situ conditions. Depending on the shear behavior, three to four tests with a load between 4 – 20 kg were done. The weight of the frame and the correction of the horizontal friction have been considered.

5.1.1 KSL_2

The test for this sample was done with 12 kg, 16 kg and 20 kg. The consolidation time of KSL_2 was with 1 minute for every test very low, but it didn't show any settlements after that time anymore.
The results for the test reach from 46 kN/m^2 up to nearly 63 kN/m^2. The spreading around the failure envelope is little, as shown in Figure 29. The Cohesion of this sample was calculated with 20,02 kN/m^2 and friction angle with 27,32°.

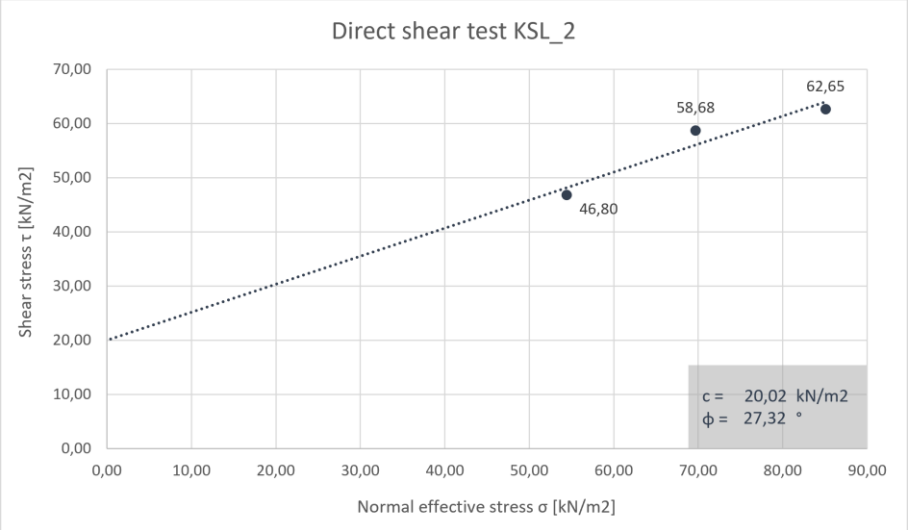

Figure 29: Results direct shear test KSL_2.

5.1.2 KSL_4

Figure 30 illustrates the conclusion of the direct shear test of sample KSL_4. The weights for these tests were 4 kg, 8 kg, 12 kg, 16kg and 20 kg. The first evaluations were unsatisfying, so more shear tests were done.
The range of the shear strength is between 38 kN/m^2 and 75 kN/m^2. The shear parameters are calculated from this, with a result of 24,93 kN/m^2 for the cohesion and 24,39° for the friction angle.

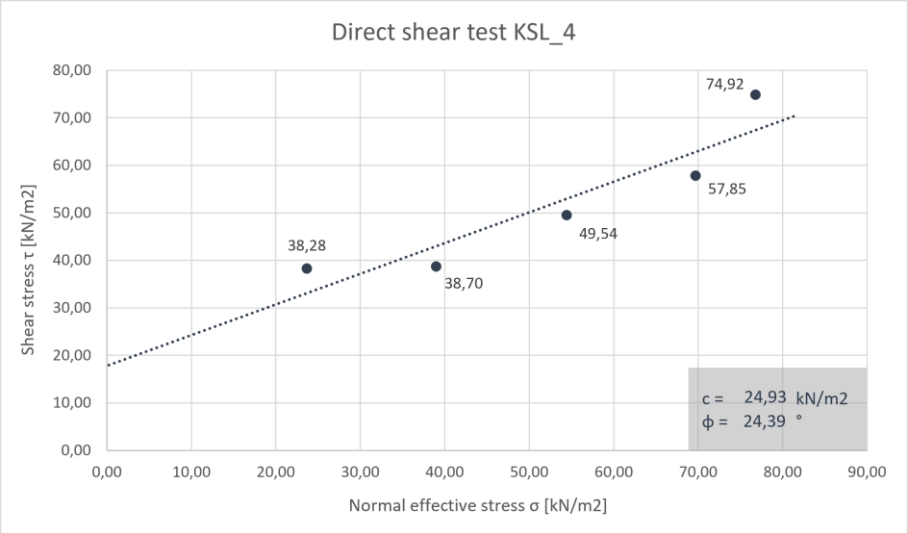

Figure 30: Results direct shear test KSL_4.

5.1.3 KSL_5

Four shear tests with loads from 4kg, 8 kg, 12 kg and 16 kg were done for KSL_5. The shear stresses range from 35kN/m^2 to 53 kN/m^2. The spreading around the failure envelope is higher with the lower loads than with the higher ones, which can be seen in Figure 31. The calculated value for the cohesion is 22,06 kN/m^2 and for the friction angle 22,54 kN/m^2.

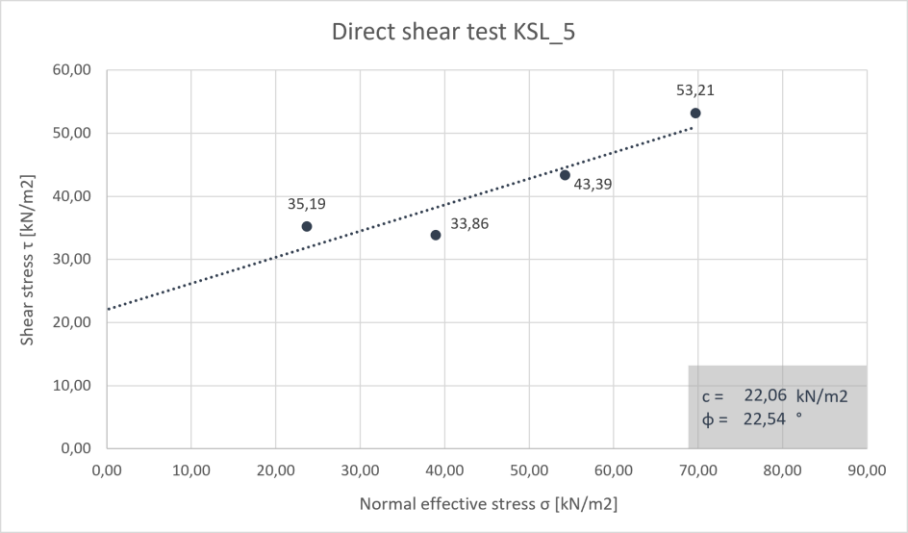

Figure 31: Results direct shear test KSL_5.

5.1.4 KSL_7

The sample KSL_7 caused a long consolidation time (10 - 20 minutes) until the tests could be done. It built a perfect failure envelope and shear surface, which is shown in Figure 32, after every direct shear test.

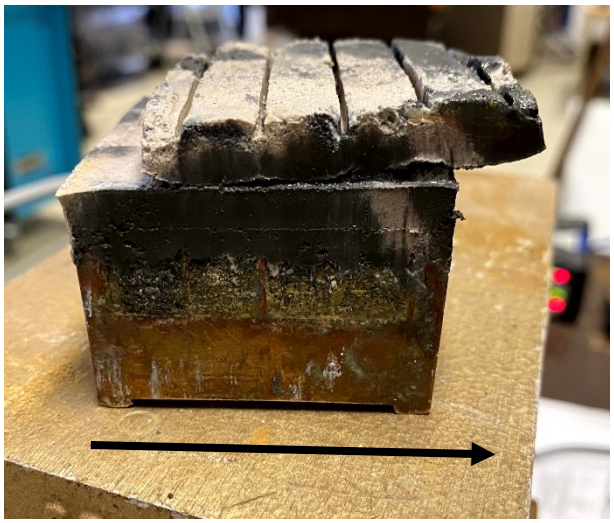

Figure 32: Picture of KSL_7_12kg after the direct shear test. The arrow shows shear direction (19.09.2022).

The evaluation showed peak shear stress values between 23 kN/m² and 50 kN/m². These are directly on the failure envelope, which can be seen in Figure 33.
The slope of the line is 29,69° and the cohesion was calculated with 10,67 kN/m².

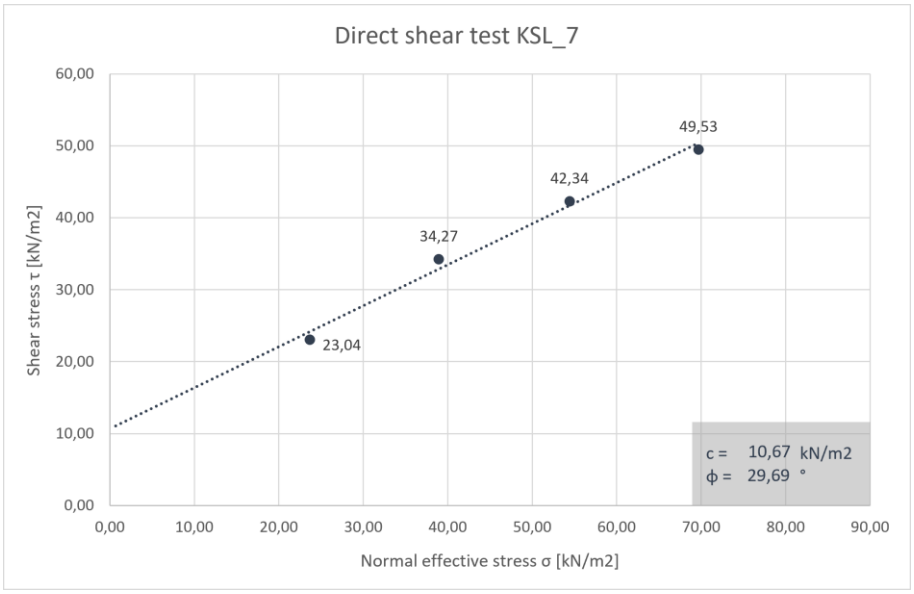

Figure 33: Results direct shear test KSL_7.

5.1.5 KSL_8

Figure 34 shows the results of the direct shear test for KSL_8 with 8 kg, 12 kg, 16 kg and 20 kg. The peak shear stresses range from 39 kN/m² up to 65 kN/m². The cohesion was calculated with 15,22 kN/m² and the friction angle with 28,94 °.

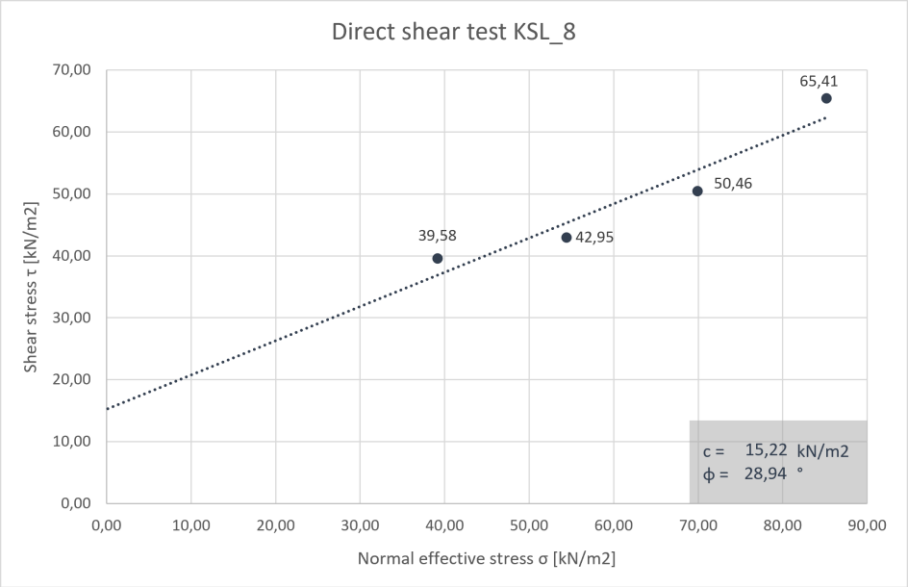

Figure 34 Results direct shear test KSL_8.

5.1.6 KSL_9

The test for this sample was done with 12 kg, 16 kg and 20 kg. The consolidation time of KSL_2 was with 1 minute for every test very low, but it didn't show any settlements after that time anymore.

The results for the test reach from 46 kN/m^2 up to nearly 63 kN/m^2. The spreading around the failure envelope is little, as shown in Figure 29. The cohesion of this sample was calculated with 20,02 kN/m^2 and friction angle with 27,32°.

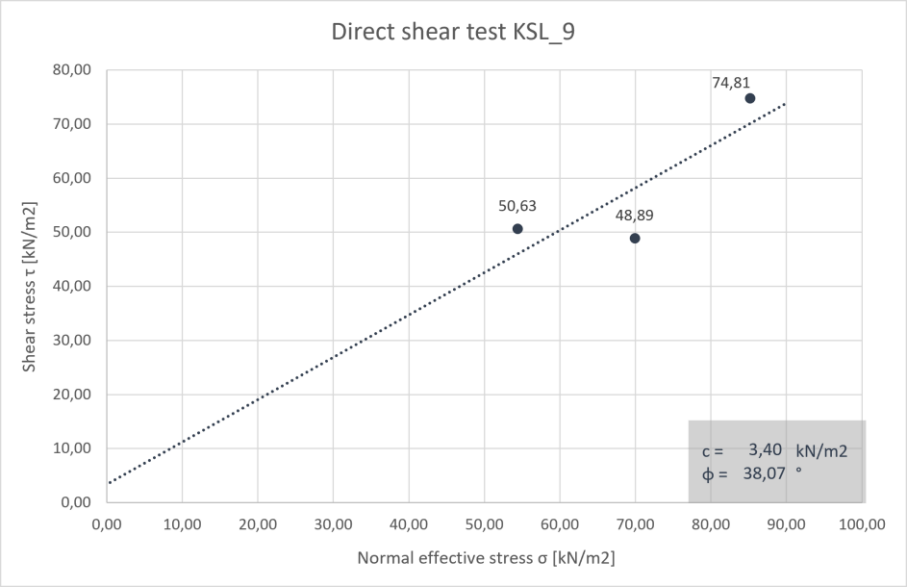

Figure 35: Results direct shear test KSL_9.

5.1.7 KSL_10

With peak shear strength between 22 kN/m^2 and 50 kN/m^2 the direct shear test was successfully completed for KSL_10. As shown in Figure 36, four tests with 4 kg, 8 kg, 12 kg and 16 kg were done due to the variance along the fracture line.

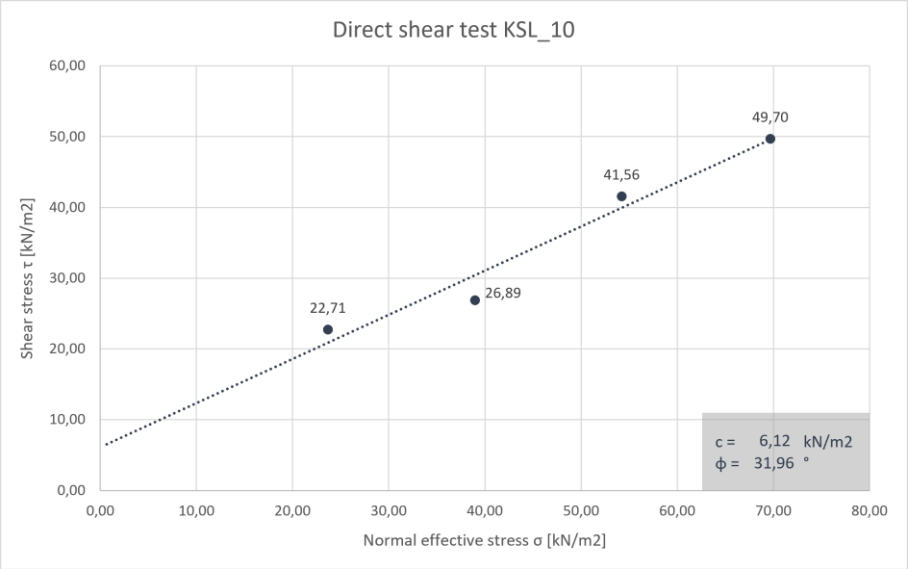

Figure 36: Results direct shear test KSL_10.

The soil like material shows well defined shear surface, as shown in Figure 37.

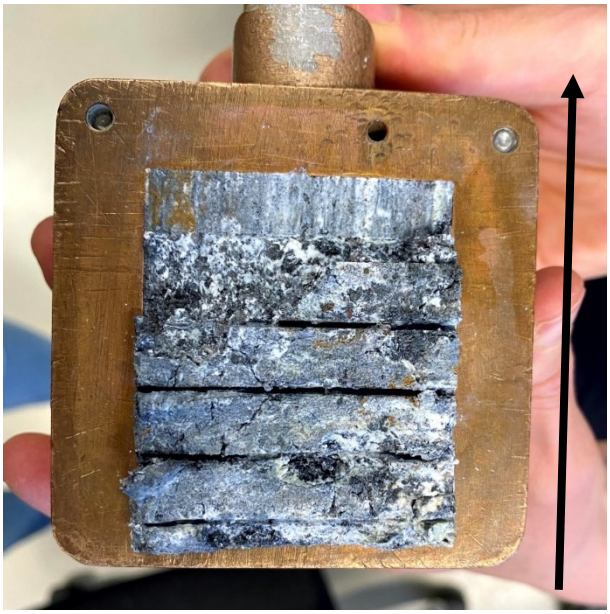

Figure 37: Concisely defined shear surface of KSL_10_12 kg. The arrow points in shear direction (18.07.2022).

The friction angle for the sample was calculated with 31,96° and a cohesion 6,32 kN/m^2.

5.1.8 KSL_11

The test for this sample was done with 8 kg, 12 kg and 16 kg. The consolidation time of KSL_11 decreased from 17 to 10 minutes with each test.
The shear strengths reach from 33 kN/m^2 up to nearly 52 kN/m^2. The spreading around the failure envelope is little, as shown in Figure 38 . The Cohesion of this sample was calculated with 8,67 kN/m^2 and friction angle with 31,02°.

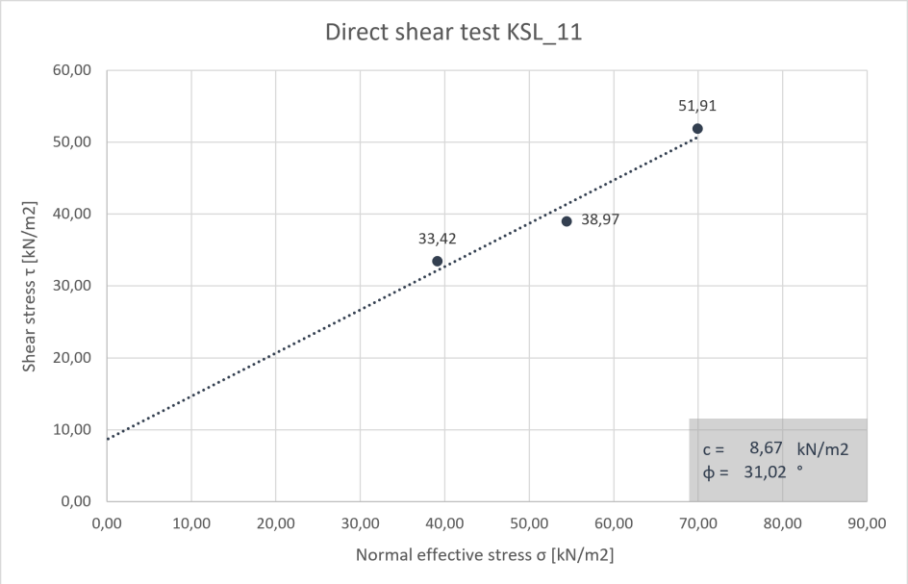

Figure 38: Results direct shear test KSL_11.

5.1.9 KSL_12

Compared to KSL_11, this sample shows higher shear strengths with values between 57 kN/m^2 up to nearly 75 kN/m^2. The weights used were 8 kg, 12 kg and 16 kg. All results of peak strengths are lying along the friction line (Figure 39).
The determined values for the friction angle and the cohesion are 29,41° and 34,62 kN/m^2.

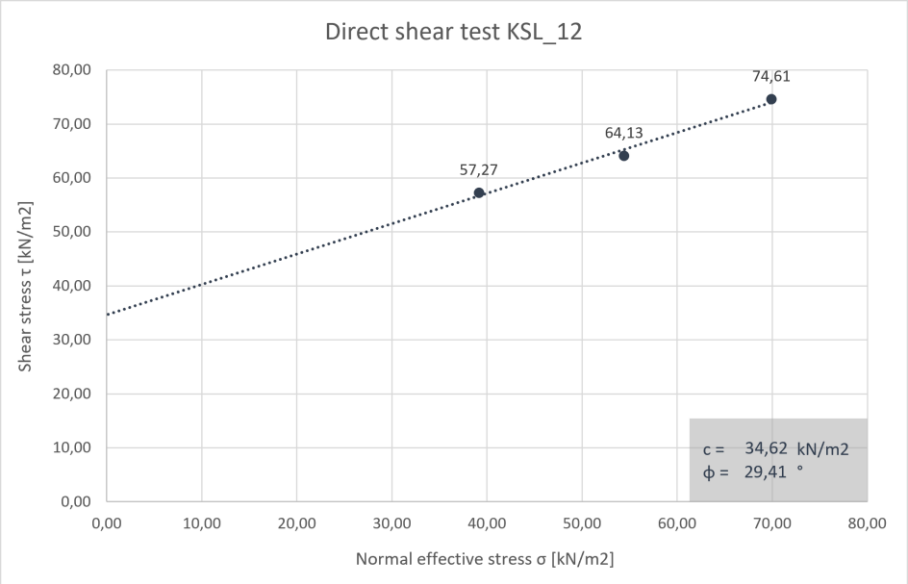

Figure 39: Results direct shear test KSL_12.

5.1.10 KSL_13

Figure 40 shows the results of the direct shear test of sample KSL_13. The shear parameters were calculated with c = 19,28 kN/m^2 and φ = 24,27°.
The test was executed with 8 kg, 12 kg and 16 kg. There is no spreading around the friction line, so no more than three tests were needed.

The consolidation time was shortened from 18 to 10 minutes with the increasing amount of tests.

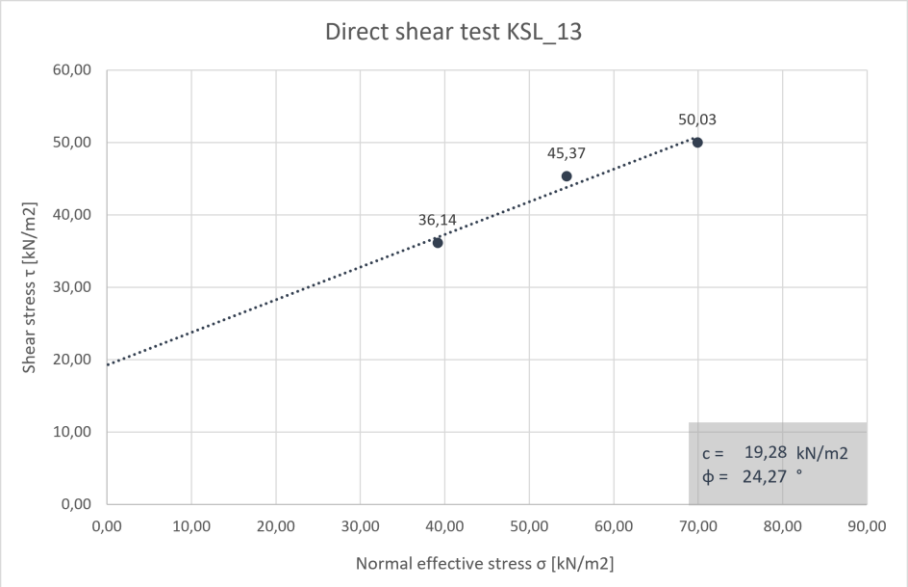

Figure 40: Results direct shear test KSL_13.

5.1.11 Summarized results of the direct shear test

Table 2 gives an overview of the calculated values for cohesion and friction angle of all samples.

Table 2: Combined results of the shear tests of all samples.

Sample	Cohesion [kN/m2]	Friction angle [°]
KSL_2	20,02	27,32
KSL_4	24,93	24,39
KSL_5	22,06	22,54
KSL_7	10,67	29,69
KSL_8	15,22	28,94
KSL_9	3,40	38,07
KSL_10	6,12	31,96
KSL_11	8,67	31,02
KSL_12	34,62	29,41
KSL_13	19,28	24,27

5.2 Results of the sieve analysis and hydrometer test

The grains size distribution compiled from the sieving and the hydrometer test are presented in the following.

5.2.1 KSL_2

The dry-sieve – and the hydrometer analyses for KSL_2 are illustrated in Figure 41.

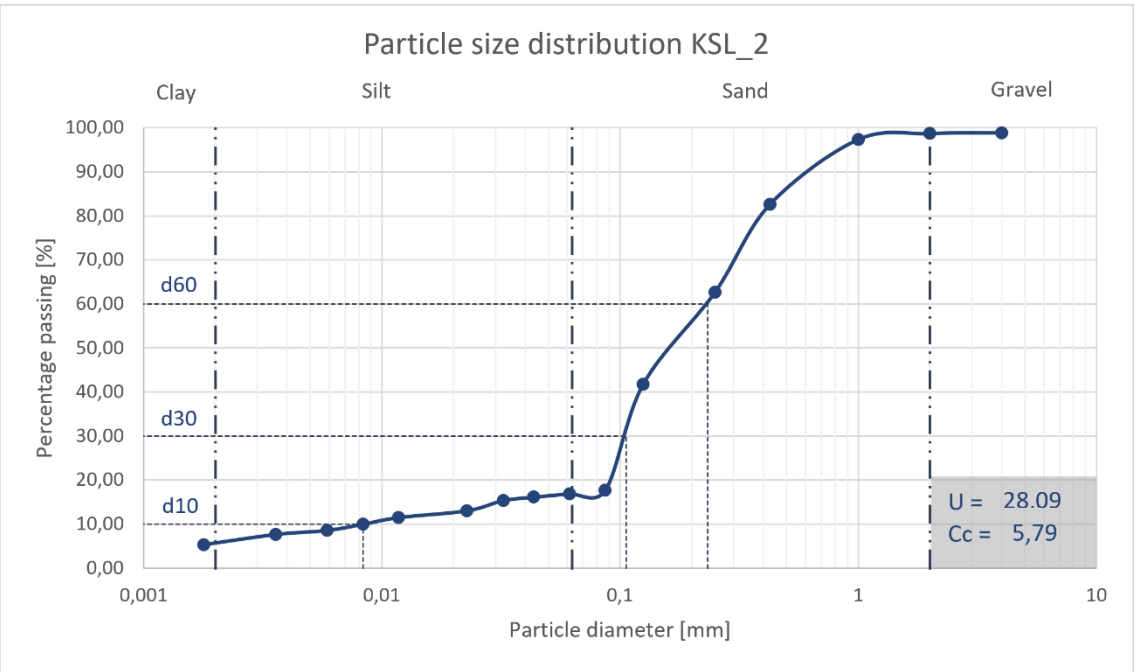

Figure 41: Grain size distribution of KSL_2 and its determined U and Cc.

The coefficient of uniformity and the coefficient of curvature are both very high (U = 28,09 and Cc = 5,79). The sieve line is widespread, as seen in Figure 41. More than 83 % are not passing the 63 µm sieve.

5.2.2 KSL_4

Just like KSL_2, KSL_4 was also dry sieved. Figure 42 shows the combined result of the dry-sieve and the hydrometer test. More than 77 % of the material is coarse grained and in the sand fraction. The sieve line spans over a wide range of the particle diameter. U reaches a high value of 70,61, so does Cc with 19,39.

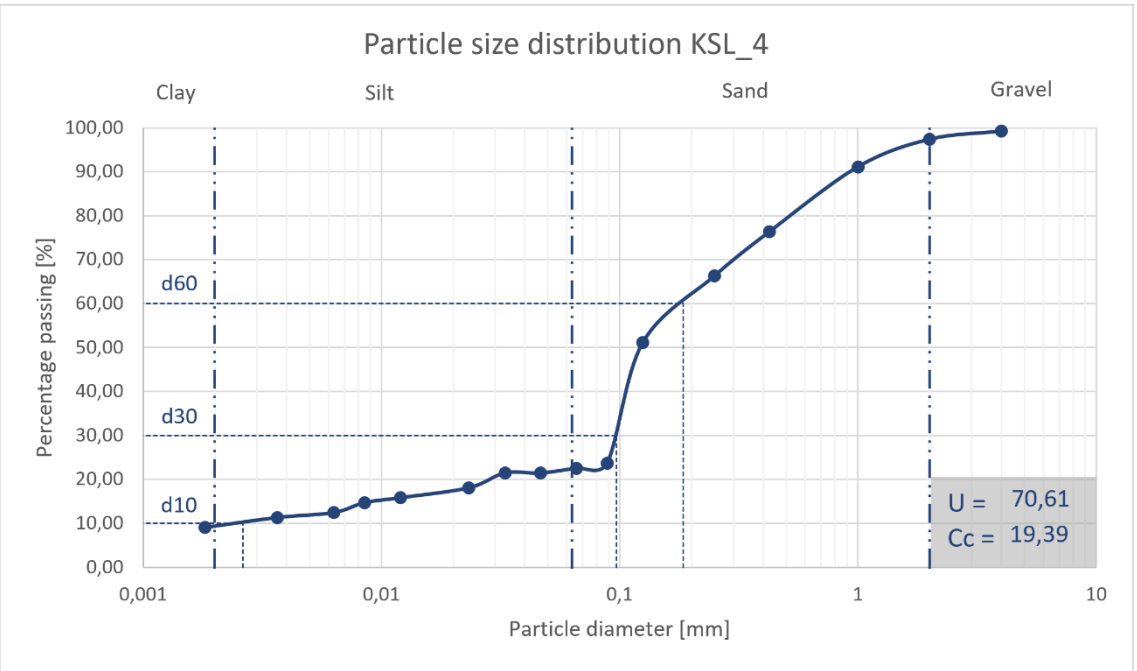

Figure 42: Grain size distribution of KSL_4 and its determined U and Cc.

5.2.3 KSL_5

With a major of its grain size fraction (75 %) defined as sand, KSL_5 shows just a quarter of fines. The coefficient of uniformity and a coefficient of curvature result in the values of 53,96 and 26,87. The widespread sieve line is presented in Figure 43.

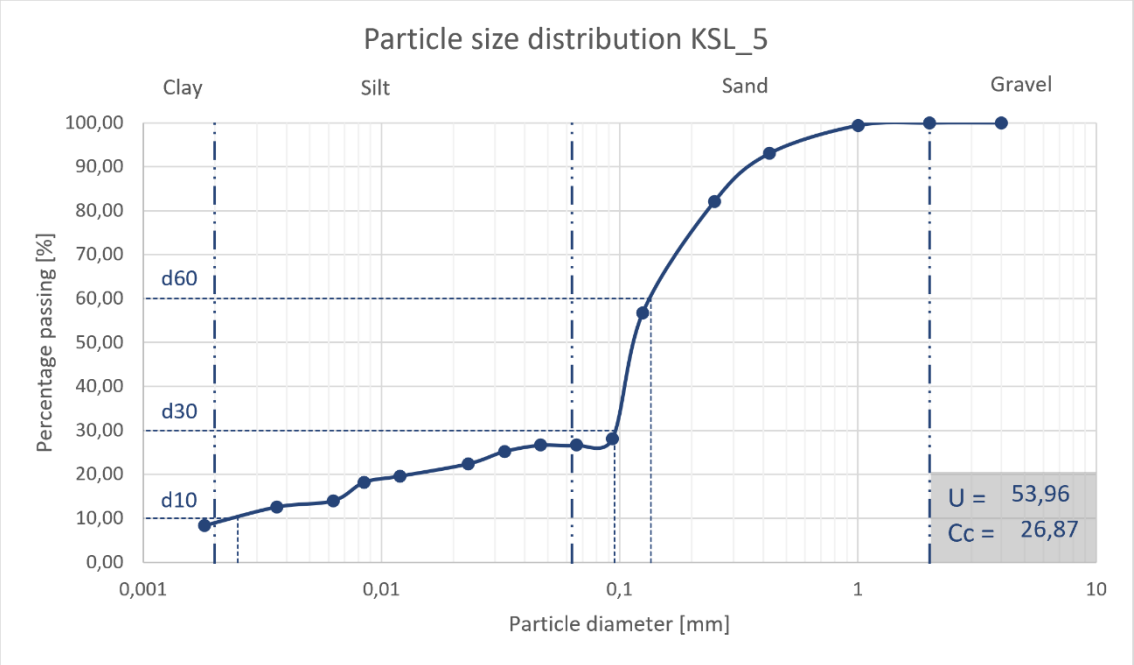

Figure 43: Grain size distribution of KSL_5 and its determined U and Cc.

5.2.4 KSL_7

The first try to dry sieve sample KSL_7 dry failed and yielded wrong results. A second wet sieving delivered the results presented in Figure 44.

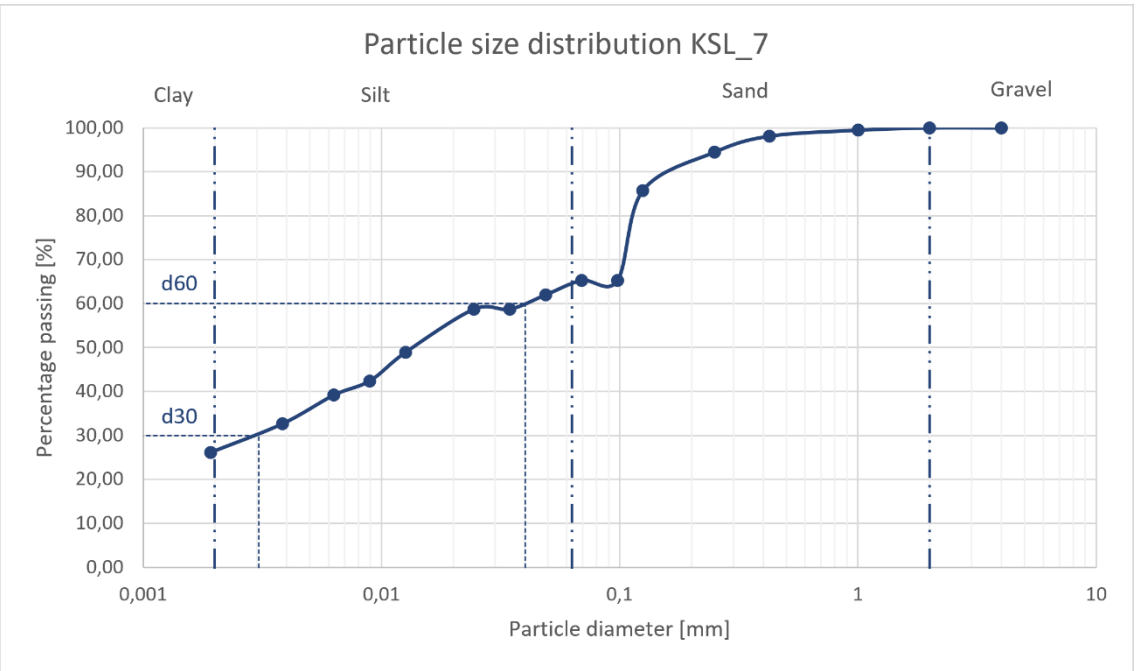

Figure 44: Grain size distribution of KSL_7 and its determined U and Cc.

The amount of fine-grained material is 65 %. Unfortunately during the hydrometer test the testing time was not sufficient to get the exact amount of clay nor the particle diameter of d_{10}. Hence no U and Cc were calculated for this sample.

5.2.5 KSL_8

The results of the dry-sieving and hydrometer analyses are shown in Figure 45.

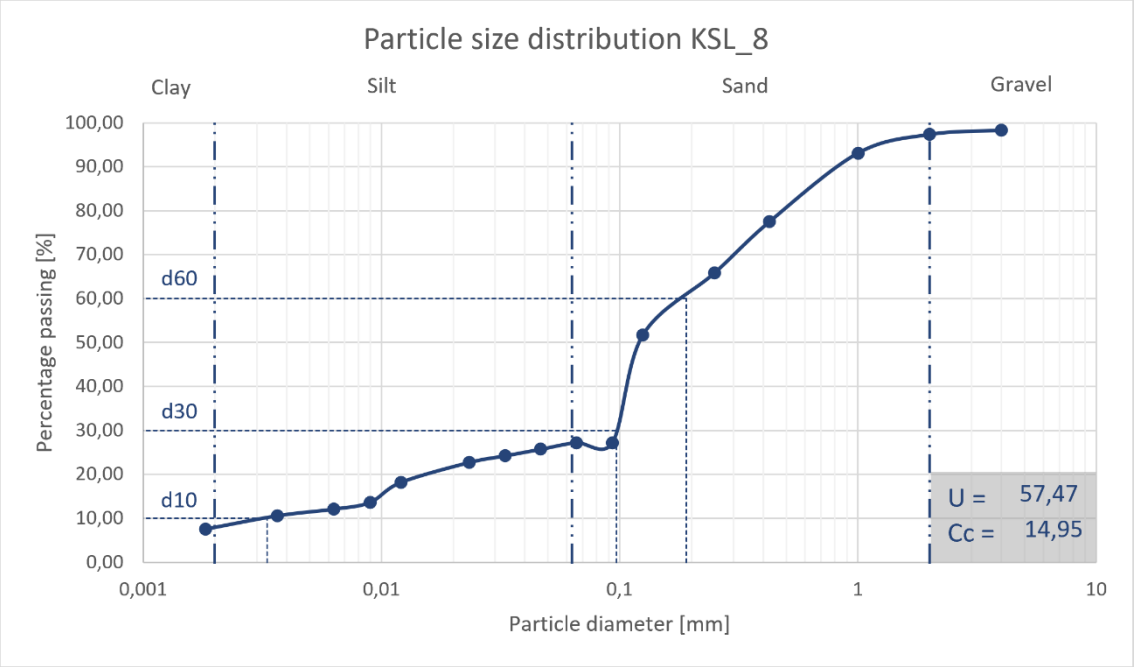

Figure 45: Grain size distribution of KSL_8 and its determined U and Cc.

The coefficient of uniformity was calculated with 57,47 and the coefficient of curvature with 14,95. The coarser grain fracture is with 73 % higher than the amount of fine grain fracture.

5.2.6 KSL_9

Figure 46 presents the results of the sample KSL_9. The major fraction amount (85%) is buildup of the coarser grain fraction sand and shows a steep slope in that range. The coefficients U and Cc reach a value of 14,40 and 6,11.

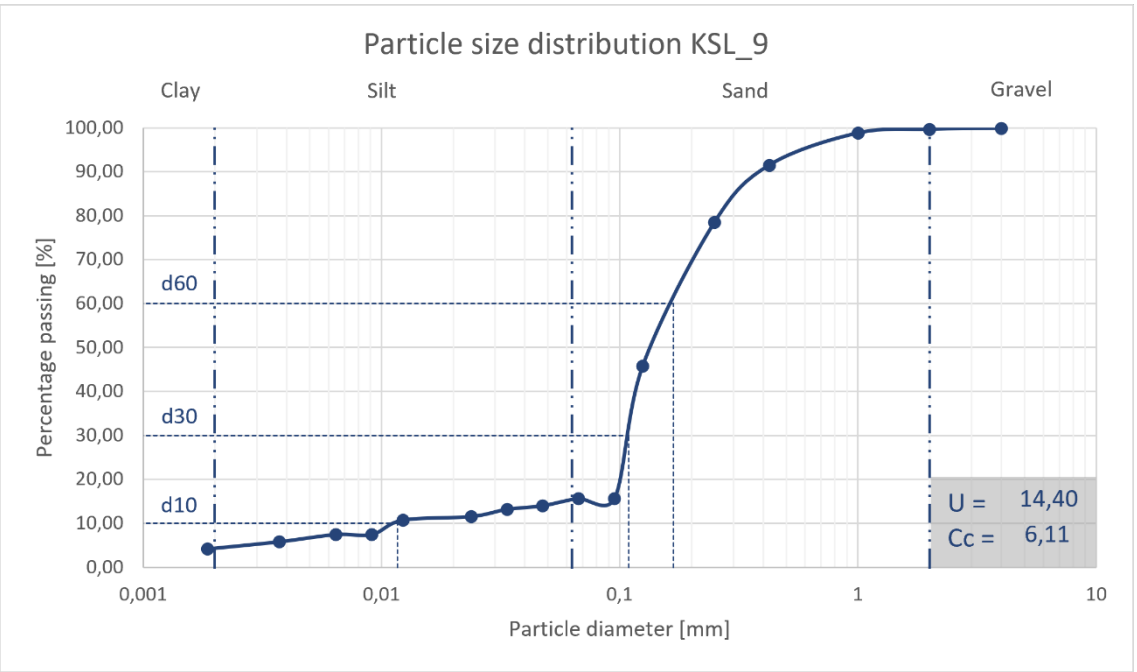

Figure 46: Grain size distribution of KSL_9 and its determined U and Cc.

5.2.7 KSL_10

During the first dry sieving, it turned out that a wet sieving has to be applied. Though the amount of the sand fracture is with a value of 57 % predominant, the hydrometer test was not sufficient to obtain a distribution of the clay-sized particles. The coefficients could not be calculated due to the missing data. The clay content is very high (35 %), as shown in Figure 47.

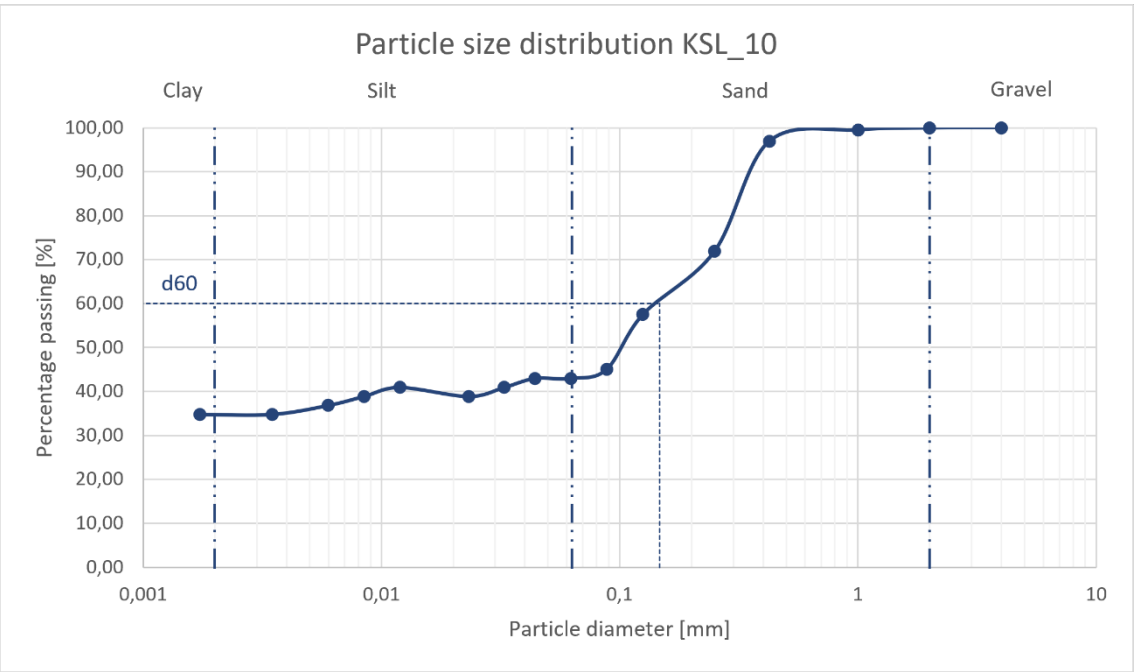

Figure 47: Grain size distribution of KSL_10 and its determined U and Cc.

5.2.8 KSL_11

With a major of its grain size fraction (73 %) defined as sand, KSL_11 shows just a medium number of fines. Unfortunately the hydrometer test was not successful, and the coefficients could not be calculated due to the missing value of d_{10} . The widespread sieve line is presented in Figure 48.

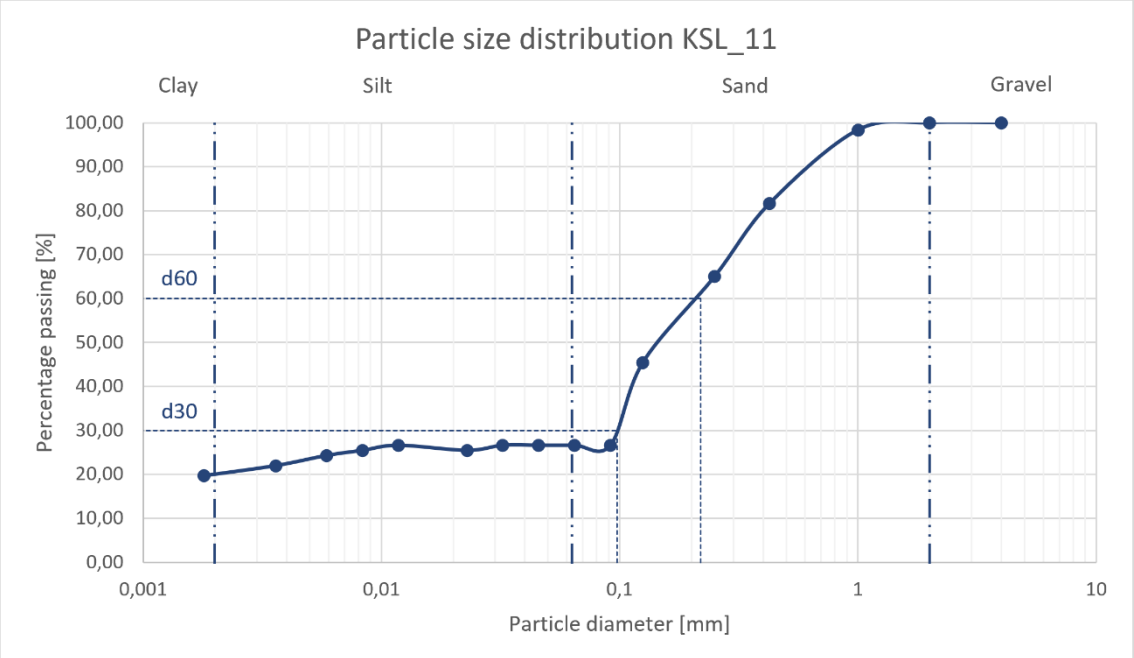

Figure 48: Grain size distribution of KSL_11 and its determined U and Cc.

5.2.9 KSL_12

Pretreated with hydrogen peroxide, the wet sieving was successfully at the second try, in contrast to the hydrometer test. The density of the solution did not change, even after waiting over three days and 8 hours (Figure 49). The fine-grained material comprises 80 % of the sample.

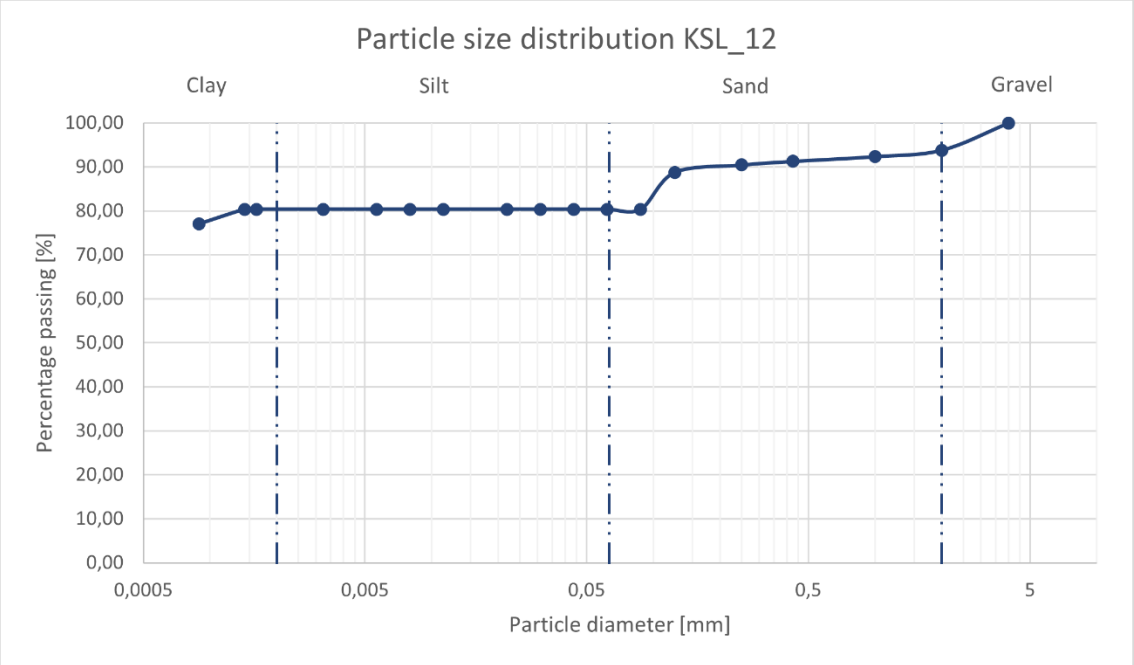

Figure 49: Grain size distribution of KSL_12 and its determined U and Cc.

5.2.10 KSL_13

Figure 50 presents the results of sample KSL_13. A wet sieving was necessary. The major fraction amount (60 %) is built up of the finer grain fractions silt and clay. The coefficients U and Cc were calculated with a value of 84,52 and 0,69.

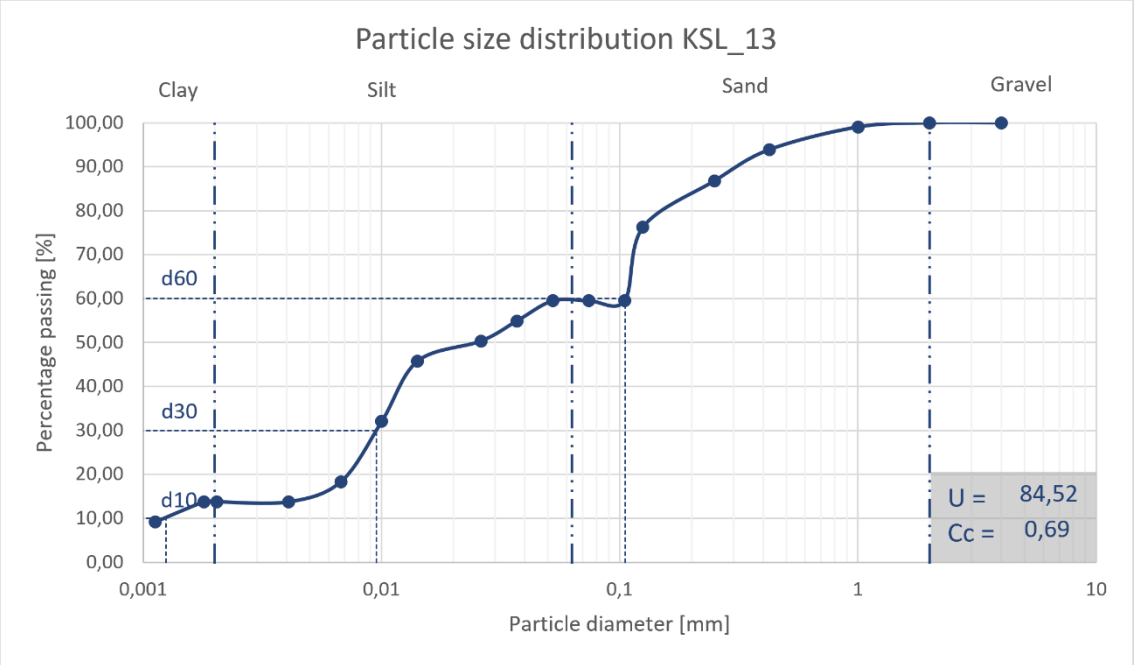

Figure 50: Grain size distribution of KSL_13 and its determined U and Cc.

5.2.11 Summarized results of the grain size distribution

An overview over the results of the previous chapter is given in Table 3.

Table 3: Results of sieve analysis and hydrometer test.

Sample	d60 [mm]	d30 [mm]	d10 [mm]	U	Cc
KSL_2	0,23	0,11	0,01	28,09	5,79
KSL_4	0,19	0,10	0,00	70,61	19,39
KSL_5	0,14	0,10	0,00	53,96	26,87
KSL_7	0,04	0,00	-	-	-
KSL_8	0,19	0,10	0,00	57,47	14,95
KSL_9	0,17	0,11	0,01	14,40	6,11
KSL_10	0,15	-	-	-	-
KSL_11	0,22	0,10	-	-	-
KSL_12	-	-	-	-	-
KSL_13	0,11	0,01	0,00	84,52	0,69

5.3 Results of Atterberg limits

Table 4 presents the results of the Casagrande test, the plastic limit test, the water content and the value of the plasticity index.

Table 4: Results of the liquid limit, plastic limit and water content, as well for the calculated plasticity index of all samples

Sample	Water content [%]	Liquid limit [%]	Plastic limit [%]	Plasticity index [%]
KSL_2	33,90	25,94	22,50	3,44
KSL_4	38,57	30,24	25,63	4,60
KSL_5	42,23	27,76	23,60	4,15
KSL_7	175,32	31,90	25,53	6,37
KSL_8	77,03	29,13	25,96	3,17
KSL_9	26,15	18,43	15,96	2,47
KSL_10	77,37	44,20	29,90	14,29
KSL_11	124,07	51,66	42,74	8,92
KSL_12	81,35	60,00	35,65	24,35
KSL_13	268,42	61,15	58,73	2,42

The water content of the samples varies between 26 % and 269 %. Especially the samples KSL_7, KSL_11 and KSL_13 are outstanding with a value of more than 100%.
The samples from the landslide and the fault zone are prominent with high liquid and plastic limits. While the average value of the samples from the two tests around the dome are 27 % and 24 %, those from the fault zone are around 54 % and 42 %.
With 2,42 % plasticity index, KSL_13 stands out with the lowest value. On the other hand, KSL_10 and KSL_12 exhibit very high plasticity.

5.4 Results of grain density and pH-value

Table 5 lists the results of the grain density and pH of all samples.

Table 5: Values of the grain density and pH measurements.

Sample	Grain density [g/cm³]	pH	Temperature [°C]
KSL_2	2,62	3,28	19,0
KSL_4	2,56	3,20	18,8
KSL_5	2,55	3,83	18,8
KSL_7	2,40	3,15	19,1
KSL_8	2,54	3,58	18,9
KSL_9	2,47	3,19	19,2
KSL_10	2,55	2,87	19,7
KSL_11	2,44	2,36	20,3
KSL_12	2,54	2,77	19,6
KSL_13	2,20	1,47	21,1

The average value for the grain density is around 2,52 g/cm^3. KSL_13 has an outstandingly low density, which is only 2,20 g/cm^3.
When evaluating the pH values, a clear distinction can be made between the material around the summit and the samples from the landslide and fault zone. While the former range between 3,83 and 3,15, the latter are even more acidic, with a result below 2, and for KSL_13 even below 1,50.

5.5 Results XRD

X-ray diffraction was conducted on all ten samples. The results are summarized in Appendix A – Results XRD analysis.
Except for KSL_7, which is fundamentally different from the others, the primary phases of plagioclase (andesine), pyroxene (oxp+cpx), amphibole (hornblende) and quartz were identified in the samples taken around the summit of the volcano.
KSL_2 – KSL_5 have a high content of the residual plagioclase, clino- and orthopyroxene and a higher content of smectite than kaolinite/halloysite. They are also characterized by a high tridymite content. KSL_8 and KSL_9 differ in this respect by a higher kaolinite/halloysite content.
KSL_7 has a very high opal content and no smectite, but halloysite/kaolinite. Tridymite, cristobalite and pyrites also occur in the mineral assemblage. Alunite is also included in the sample and clino- and orthopyroxenes are present. Similar to this sample is KSL_10, which differs by an even higher kaolinite content. It also lacks the residual pyroxenes and tridymite.
Most interesting are the samples from the fault zone. KSL_11 has predominantly halloysite and less smectite. Some opal occurs as does cristobalite. Some residual pyroxenes are also appearing. KSL_12 consists mainly of kaolinite. Minor components are pyrite, anatase, marcasite and possibly ferrihydrite.
No clay minerals are occurring in sample KSL_13. Consisting mainly of amorphous phases (opal-A) it also includes some traces of cristobalite, pyrite, quartz and possible ferrihydrite. Also, some anatase arises.

5.6 Results XRF

In Appendix B - Results XRF analysis, the chemical composition is listed of the investigated soil like material.

There is a variability in the elemental analysis between the samples from the dome area and the landslide/fault area. Except KSL_7, KSL_2 to KSL_9 have an average amount of SiO_2 of 60 % and differ from the rest of the samples due to a higher content of MgO, CaO and Na_2O. The Al_2O_3-content is significantly lower than that of samples KSL_10 - KSL_12, the latter additionally having a high V content (518 ppm). KSL_13 stands out due to the especially high Cu-Zn content of 0,1 % in each case.
In terms of the loss on ignition (LOI), we can see an increase in values from about 6% of the summit samples (except KSL_7), to ~13% of the samples from the fault zone.

6 Discussion

Further evaluations and correlations of the previous chapter should shed light on the influence of the hydrothermal activities at the volcano La Soufrière de Guadeloupe. They are discussed in the following.

6.1 TAS classification

For the classification and nomenclature of volcanic rocks, where the modal mineral content could not be determined, a classification was made in the TAS diagram (Figure 51).

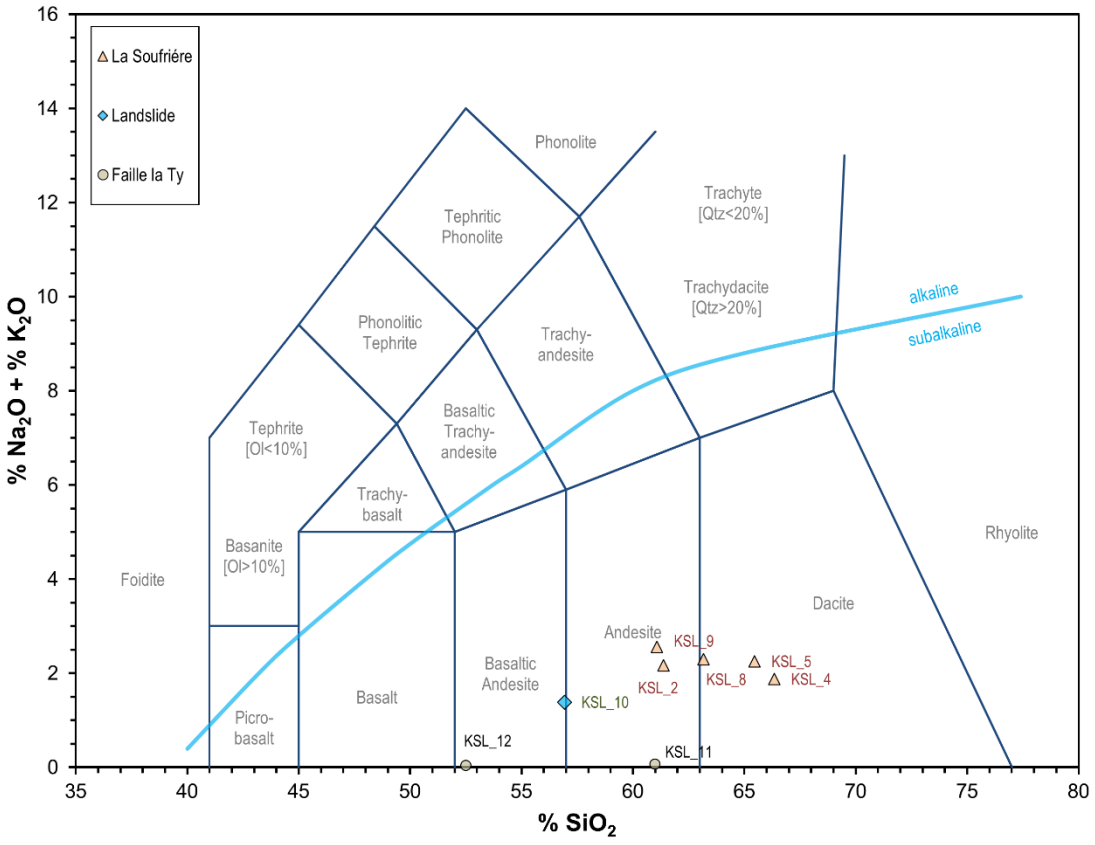

Figure 51: Total Alkali Silica diagram of the samples.

Komorowski et al. (2005) mentioned that the magma composition of the Grand Découverte-Soufrière volcanic center as homogenous and is represented by medium-K calc-alkaline basaltic andesites and andesites. Some andesite to dacite (~59 to 69 wt. % SiO_2 (Boudon et al., 1988a)) lava flows had been produced. These observations can be supported by the results of the samples. Most of them can be classified as andesites, with KSL_10 and KSL_12 being more of a basaltic andesite. KSL_4, KSL_5 and KSL_8 contain a higher SiO_2-content and are already identified as dacite.
However, the classification should be viewed with caution, as circulating fluids may have altered the chemical composition. For example, two samples, KSL_7 and KSL_13, are not listed in the diagram because their quartz content is 72% and 82%. They would therefore be referred to as rhyolites. In the case of the second, however,

it appears that it is very altered and therefore the high SiO_2 content is not representative of the original composition.

6.2 USCS classification

In order to make a classification according to the unified soil classification system, the results of the particle size distribution are compared with those of the Atterberg limits. As the samples are in-situ altered samples and not sediments, this classification may differ because of the prevailing conditions on the volcano. Due to the ongoing hydrothermal alteration, the proportion of the fine-grain fraction could change and lead to a different result.
First, the water content, the liquid and plastic limits were used to classify the soil in the plasticity chart. This is shown in Figure 52. It can be seen that all samples except KSL_9 are below the A-line. Most of them are classified as low plasticity silt, KSL_11, KSL_12 and KSL_13 as high plasticity silt.

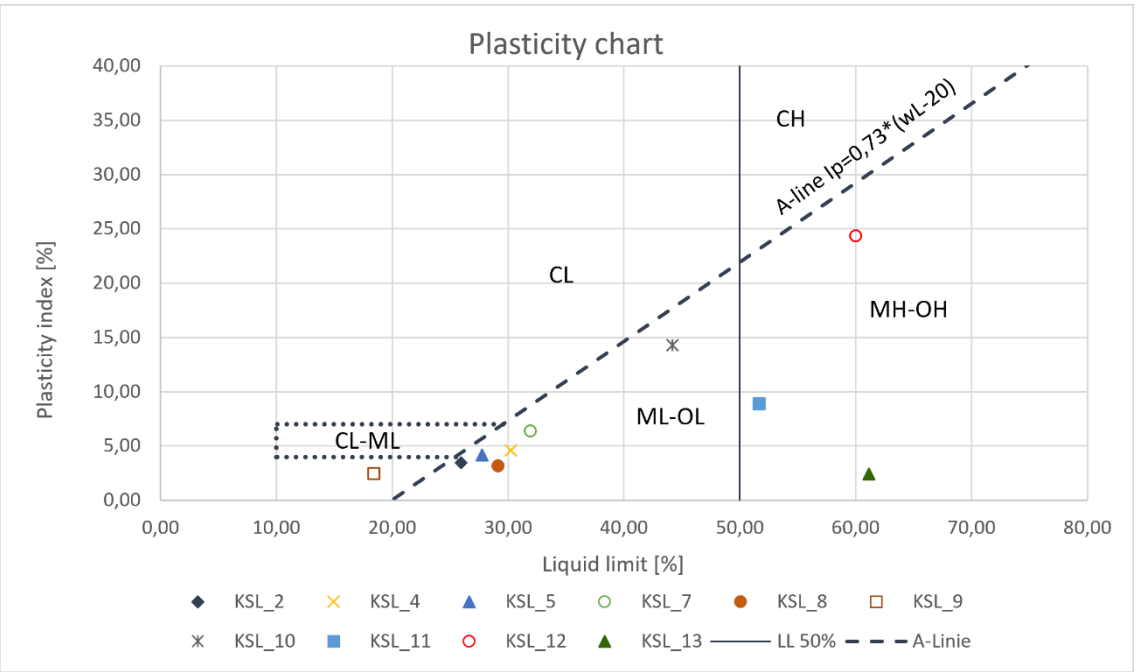

Figure 52: Casagrande plasticity chart; CL=clays with low plasticity; CH=clays with high plasticity; ML-OL=silts and organic soils with low plasticity; MH-OH=silts and organic soils with high plasticity

6.2.1 KSL_2

Due to the high values of the coefficient of uniformity U and the coefficient of curvature Cc (U>6 and Cc>3), the sample is non-uniform and poorly graded.
The amount of fine-grained particles (<63 µm) is smaller than 17 %. Considering the Atterberg limits, KSL_2 is plotted below the A-line. All these results classify the sample as silty sand, sand silt-mixture (SM).

6.2.2 KSL_4

With a value for U of 70,61 and Cc of 19,39, sample KSL_4 cannot be interpreted as well-graded.

The sample is situated in the plasticity chart under the A-line and therefore in the area for silts and organic soils with low plasticity. This fact, and the fact that only 23 % of the sample are finer than 63 µm, KSL_4 is defined as silty sand, sand silt-mixture (SM).

6.2.3 KSL_5

The particle size distribution of KSL_5 results in a sieve line, which spans over a wide range of the grain sizes, leading to U > 6 and a Cc > 3.
75 % of the grains did not pass the 63 µm sieve. The plasticity chart shows that the values of the liquid limit and the plasticity index led to a position below the A line in the low plasticity area for silt and organic soils. The sample can be classified as silty sand, sand silt-mixture (SM).

6.2.4 KSL_7

The high amount of silt and clay (65 %), a liquid limit 31,90 and the fact that it plots below the A-line in the plasticity chart, defines sample KSL_7 as an inorganic silt, rock flour, silt of low plasticity (ML).

6.2.5 KSL_8

In the plasticity chart KSL_8 is situated below the A-line. Both coefficients U and Cc are higher than the limit for well-graded material. According to the USCS it is a silty sand, sand silt-mixture (SM).

6.2.6 KSL_9

Sample KSL-9 is the only sample, which is plotted over the A-line in the plasticity chart. It is in the range of clays with low plasticity.
The amount of fine fraction is below 15 %. All these results classify KSL_9 as a clayey sand, sand-clay mixture (SC).

6.2.7 KSL_10

The high amount of sand (57 %) and the fact that it plots below the A-line in the plasticity chart, defines sample KSL_10 silty sand, sand silt-mixture (SM).

6.2.8 KSL_11

The particle size distribution of KSL_11 results in a sieve line, which spans over a wide range of the grain sizes. Due to the missing data, no statement can be made about the grading.
73 % of grains did not pass the 63 µm sieve. The plasticity chart shows that the values of the liquid limit and the plasticity index led to a position below the A line in the high plasticity area for silt and organic soils. The sample can be classified as silty sand, sand silt-mixture (SM).

6.2.9 KSL_12

The silt and clay amount of the sample is very high with 80 %. The failed hydrometer test could be explained by the high content of kaolinite/halloysite (96 %). Maybe the dispersion agent reacted with it and held the platelets in suspension.
Nevertheless, KSL_12 is plotted in the plasticity chart below the A-line, in the range of silt and clay with high plasticity. The liquid limit reaches 60,00 %. According to the USCS it is a inorganic silt, micaceous silt, silt of high plasticity (MH).

6.2.10 KSL_13

The amount of fine-grained material (<63 µm) is 60 %. Considering the Atterberg limits, KSL_13 has a liquid limit of 61,15 % and lies below the A-line. All these results classify the sample as inorganic silt, micaceous silt, silt of high plasticity (MH).

6.3 Classification of the alteration type

The secondary minerals, including silica polymorphs (cristobalite, quartz, tridymite and opal-A), hematite, pyrite, alunite, gypsum, kaolinite and talc occurring in our samples were interpreted by Heap et al. (2021) as the result of fluid-rock interactions. They were formed by cooled (150°C – 350°C), acidic (pH < 4) hydrothermal fluids, mixed with meteoric water. Faults and fractures allow the drainage of fluids and supergene and hypogene alteration. Intermediate to advanced argillic alteration form in these environments. For further classification of the alteration type of the samples, the pH and the secondary minerals were plotted in the chart by Corbett and Leach (1998), shown in Figure 53.

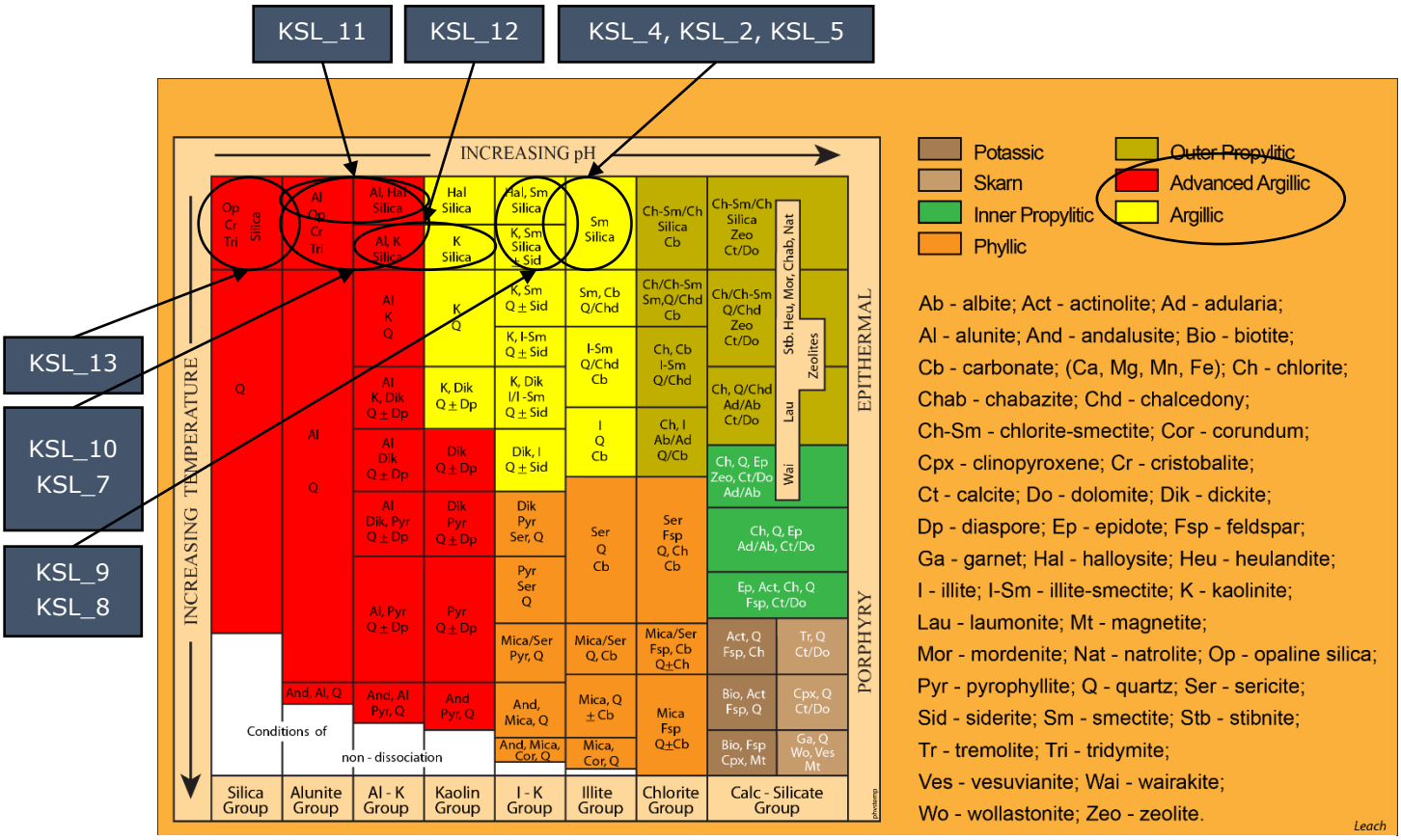

Figure 53: Temperature vs. pH chart of any hydrothermal alteration associated with epithermal and porphyry mineralization (Corbett, 2009). Mineralization assemblages of the samples from volcano La Soufrière de Guadeloupe are marked.

All samples have experienced epithermal alteration at low temperature, which is expected given their occurrence at the surface. Samples KSL_2, KSL_4 and KSL_5 can be assigned to the in the illite to illite-kaolinite group, based on the mineral assemblage and pH. Although the main constituent of the clay minerals is smectite, which forms at 100-150°C (Corbett and Leach, 1998) there is also a small amount of Kaolinite/Halloysite. Kaolinite/halloysite is the key mineral of argillic alteration facies and form at low fluid temperatures (<150°C – 200°C) and a pH of ~4,5 – 6 (Fulignati, 2020; Inoue, 1995), but also occur in advanced argillic alteration (pH < 3, temperatures <300°C). Furthermore, Corbett (2009) describes the Illite group as

having a pH of 5-6, but this is lower in the samples at ~3,4, which fits better to the Illite-kaolinite group. Those classes are interpreted as weak argillic alteration.
The increasing acid sulfate alteration causes an increasing amount of kaolinite/halloysite and the simultaneous decrease in smectite. For this reason, KSL_8 and KSL_9 can be assigned the illite-kaolinite group. The decreasing pH value confirms this, which classify the alteration type as argillic.
KSL_11 shows major acid sulfate alteration, due to its high content of kaolinite/halloysite and the occurrence of opal and cristobalite between the alunite-kaolinite and alunite group, whereas the presence of smectite also places it in the illite-kaolinite and illite groups. The sulfate mineral alunite is produced by hypogene magmatic-hydrothermal and steam-heated alteration of supergene process (Rye et al., 1992). It is commonly found in alteration products of rhyolitic to andesitic rock compositions and forms usually at 200°C – 350°C, but is also stable at 380°C – 450°C (Henley and Berger, 2011; Meyer C., 1967). According to the pH and the mineral assemblage, KSL_11 can be classified as advanced argillic alteration, possibly overprinting previous argillic alteration.
Containing halloysite/kaolinite, alunite, cristobalite and opal, KSL_7 and KSL_10 are clearly advanced argillic alteration. The amorphous silica, including cristobalite, tridymite and opal, form within hot spring deposits at low temperatures <100 – 150°C (Reyes, 1991), placing these in the alunite and alunite-kaolinite groups.
KSL_10 together with KSL_12 show complete alteration with no primary minerals preserved. The latter consists out of 96 % kaolinite and with a pH value of 2,77, it can be assigned somewhere between kaolinite- and alunite-kaolinite groups. Due to the complete alteration, we assume that it experienced advanced argillic alteration.
Given the combination of the minerals plus the low pH value of 1,47, sample KSL_13 experienced advanced alteration to even silicification due to its mostly amorphous phase(s). According to Corbett and Leach (1998) it can be incorporated in the silica group. The high content of Cu and Zn (0,1%) makes it interesting if there are more low grade ores close to the sampling place.
Considering the alteration (=percent of secondary minerals) according to Heap et al. (2021), the amount of alteration increases with the samples in the following order: KSL_5, KSL_9, KSL_2, KSL_8, KSL_4, KSL_11, KSL_7, KSL_13, KSL_12 and KSL_10.

6.4 Correlation of geotechnical parameters and secondary minerals/alteration type

Table 6 shows the summarized information about the samples from the volcano. The sorting is according to increasing alteration, determined in the previous chapter. The column "time of influence" refers to the location of the sample within an established alteration area (near the craters = Long) or adjacent to the progressing alteration front (near vegetation = Short). The tested material from the faults has an unknown time of influence and is therefore just called fault. KSL_10 has also been included for easier presentation, since it behaves similarly to the samples of the disturbance zone.

Table 6: Division of the samples due to their mineralogical composition, alteration type, sampling position and period of influence of the hydrothermal activity.

Sample	Dominant secondary mineral	Alteration type	Sampling position	Time of influence
KSL_5	Smectite>Halloysite/ Kaolinite	Argillic	Dome near gouffre Tarissan	Long
KSL_9	Mix Smectite & Halloysite/Kaolinite	Argillic	Dome nearest living vegetation	Short
KSL_2	Smectite>Halloysite/ Kaolinite	Argillic	Dome near small fumarole	Short
KSL_8	Mix Smectite & Halloysite/Kaolinite	Argillic	Dome in dead vegetation	Short
KSL_4	Smectite>Halloysite/ Kaolinite	Argillic	Dome near cratère sud	Long
KSL_11	Halloysite/Kaolinite	Advanced argillic	Fault la Ty near very small fumarole	Fault
KSL_7	Opal-A	Advanced argillic	Dome over very small fumarole	Short
KSL_13	Opal-A	Advanced argillic	Fault la Ty near very small fumarole	Fault
KSL_12	Halloysite/Kaolinite	Advanced argillic	Fault la Ty edge	Fault
KSL_10	Halloysite/Kaolinite	Advanced argillic	Landslide	Fault

6.4.1 Correlation of secondary minerals vs. alteration

Figure 54 shows the results of the XRD versus the alteration. Further graphical evaluations with the exact trends of the increasing or decreasing secondary minerals versus the alteration are attached in Appendix C – Diagrams of secondary minerals vs. alteration. Kaolinite/halloysite content initially remains constant during weaker argillic alteration and increases with advanced argillic alteration. Smectite increaes with the progression of argillic alteration, but it does not occur in samples with major acid sulfate alteration except for KSL_11.

There are no opal-bearing samples with argillic alteration, except for KSL_11. Opal is one of the key minerals used to identify the type of hydrothermal activity in this sample set. Cristobalite occurs only in samples with advanced alteration and the content increases with increasing alteration. The samples taken in the dome area contain tridymite in contrast to the samples from the landslide and fault zone, which contain none.

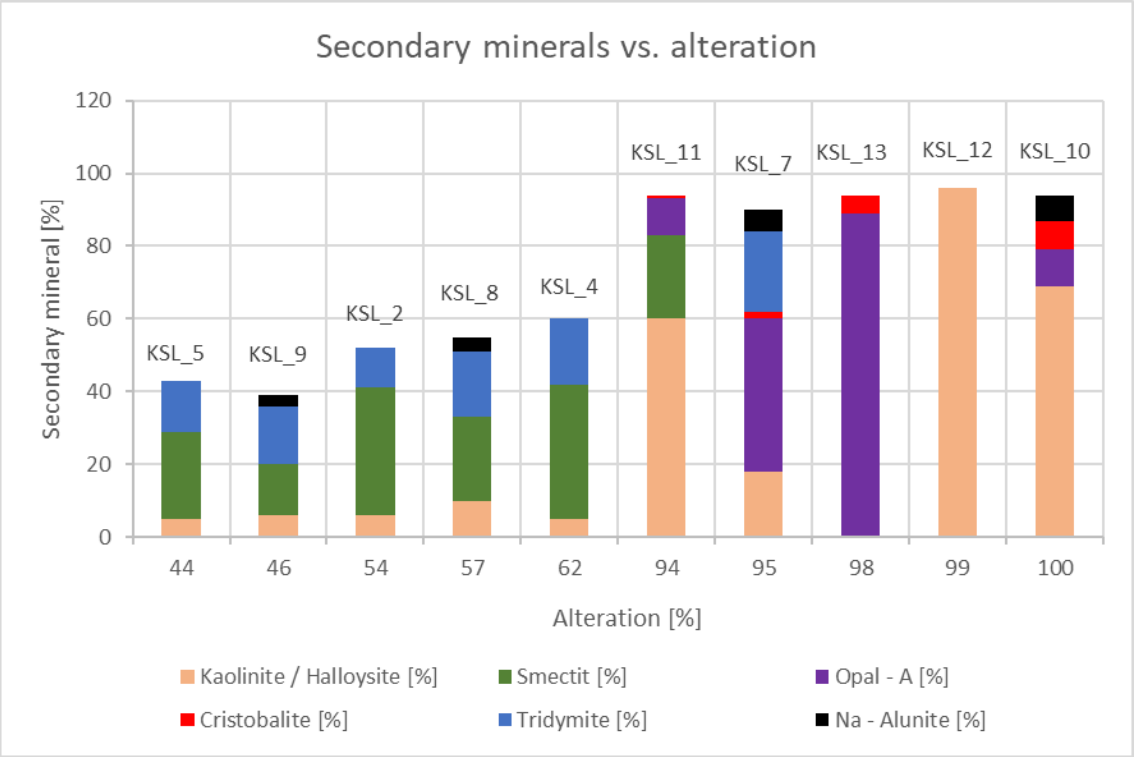

Figure 54: Samples ordered along increasing alteration (=percent secondary minerals) versus mineral content.

6.4.2 Correlation of secondary minerals vs. shear parameters

The graphical results of Appendix D – Diagrams secondary minerals vs. shear parameter show that there is an increase in cohesion with increasing secondary mineral content, independent of the type of mineral.
The friction angle decreases with increasing opal and kaolinite/halloysite content and increases with increasing smectite.
For the comparison between the shear strength of the samples, the value at 70 kN/m^2 normal stress was used and plotted on the x-axis versus the secondary mineral content. There is no indication that opal influences the shear strength. Higher amounts of smectite or kaolinite/halloysite seem to increase it.

6.4.3 Correlation of shear parameters vs. alteration

The comparison of the shear parameters and the progress of the alteration can be taken from the charts in Appendix E – Diagrams shear parameter vs. alteration .
The cohesion and the shear strength increase with the progress of argillic alteration, as well as for the samples with advanced argillic alteration. The opposite can be observed for the friction angle. It shows a negative trend within the argillic and the advanced argillic influenced samples.
Considering the general trend of shear parameters with increasing alteration, it seems that neither the cohesion, nor the friction angle are influenced by the rock alteration. Only the shear strength seems to increase slightly with it.
Gonzalez De Vallejo et al. (1981) and Campbell et al. (2009) attribute the frictional resistance to the particle shape of the halloysite clay minerals, and the aggregation

of the clay minerals. According to Skempton (1964), Morgenstern and Tchalenko (1967), Gylland et al. (2013) and (Gylland et al; 2014), the increase in halloysite and its tubular particle shape would lead to longer particle realignment, increasing frictional resistance. Due to the increase in kaolinite/halloysite with increasing alteration, this could also play a role in our samples.
Heap et al. (2021) also found little variation of the the friction angle for slightly to heavily altered rock samples from La Soufrière. The opposite observation was made for the rock cohesion: it is decreasing with progressive alteration. It appears that cohesion decreases significantly with increasing alteration (from 46 to 17 MPa to 400 kPa in rocks (from Heap et al. (2021), to ~18 kPa in our soil-like material), however once the rock has been altered to a soil-like material, the cohesion seems not to be influenced by further hydrothermal alteration.

6.4.4 Correlation of secondary minerals vs. Atterberg limits

As presented in the graphical evaluation in Appendix F – Diagrams of secondary minerals vs. Atterberg limits, the amount of the different secondary minerals influence the Atterberg limits in various ways.
It can be said that the increasing amount of kaolinite/halloysite leads to an increase of the plasticity index and the liquid limit, but on the other hand lowers the water content and the plastic limit. Wesley (1973) and Bain (1971) already reported of high liquid and plastic limits of halloysite clays and halloysite-rich soils, which plot under the A-line in the plasticity chart, compared to other clay minerals.
Opal on the other hand shows different correlations. The rise of the amount of amorphous silica also increases the liquid limit, the plastic limit, and is associated with increasing water content, but reduces the PI on the other hand. The PI is not affected by the content of smectite. But the higher amount of this type of clay mineral increases the liquid limit and the plastic limit but is associated with a reduction in the water content.

6.4.5 Correlation of shear parameters vs. Atterberg limits considering clay minerals

The question behind this correlation was whether the clay or silica minerals have different influences on the comparison between the cohesion or the friction angle and the water content, plasticity index and the liquid or plastic limit. The results are illustrated in Appendix G – Diagrams of shear parameter vs. Atterberg limits considering clay minerals.
First, as the liquid limit - and plastic limit increase, the cohesion also increases. The exception seems to be the samples containing kaolinite/halloysite. Their cohesion seems to decrease with increasing water content. Opal seems to have the same influence on the plasticity index. In contrast to the other weathering products, the cohesion of these samples decreases with increasing PI.
A general trend can also be made when comparing the friction angle and the water content, liquid - and plastic limits. The latter seems to decrease with increasing percentage of Atterberg limits or water content. Only kaolinite/halloysite bearing samples seem to have no effect of increasing water content on the friction angle.

As before, the influence of opal is evident in the behavior of the samples with respect to PI. It seems that the presence of this mineral shows a simultaneous increase of the PI with the increase of the friction angle. In the other cases, the shear parameter decreases. Unfortunately it seems that there is a lack of comparable studies, which are focused on soil like material originated by hydrothermal fluids. It seems that they are behaving in a different way compared to volcanic-derived sediments.

6.4.6 Correlation of shear parameters vs. Atterberg limits considering the alteration type

If we now consider the alteration type instead of the individual altered minerals, similar trends as before can be seen. The results are shown in Appendix H – Diagrams shear parameter vs. Atterberg limits considering alteration type. As before, the cohesion and the friction angle (y-axis) are plotted on the axes against the Atterberg limits and the water content.

In general, both the argillic and advanced argillic altered samples have increasing values in the cohesion, provided that the water content, plastic limit, and liquid limit also increase. This corresponds to the observation of previous evaluations. The exception is KSL_12 which has not been considered in the average due to outlying values.

An exception shows up again for the plasticity index. While the argillic altered samples continue to show a positive trend, the opal in the advanced argillic alteration samples seems to decrease the cohesion with increasing PI.

A similar observation can be made when comparing the parameters with the friction angles. Friction angle shows a reduction with the decrease of water content, liquid limit, and plastic limit. The plasticity index shows an increase of the shear parameter in the advanced argillic weathered samples, as well as a decrease in the zones argillic alteration.

6.4.7 Comparison of dome vs. fault samples

When comparing the clay mineral content of the dome and fault samples, which is visible in Table 6, higher proportion of kaolinite/halloysite content can be detected in the fault zone samples. These results are presented in Appendix I – Diagrams comparison dome vs. fault samples. Smectite, on the other hand, occurs only around the summit, except for KSL_11. Another observation is that opal is only present in KSL_7, the Faille la Ty and landslide samples.

The percentage of clay sized particles increases only slightly in samples KSL_10 - KSL_13 from the landslide and fault. KSL_12 stands out strongly with a proportion of 80%.. There also appears to be no noticeable change between the two sampling locations in terms of grain density, except for KSL_13.

6.4.8 Comparison of short-, long- and fault influence of hydrothermal alterations

The aim of this comparison was to detect a difference in the content of secondary minerals, clay content or grain density versus the duration of alteration. For this

purpose, the samples were structured according to their ongoing hydrothermal influence. This structuring is to be noted in Table 6.
Results of this comparison showed that there is significant change in clay minerals. The corresponding diagrams are presented in Appendix J – Diagrams comparison short-, long and fault influence. Thus, the short- and long-term influenced samples from the dome show a lower kaolinite/halloysite content than those of the disturbance zones of the landslide and fault. In contrast, smectite can only be detected in the samples from the dome and KSL_11. Opal occurs only in the samples of the landslide and the Faille la Ty, with exception of KSL_7.
A change with respect to the clay content and the grain content with increasing or decreasing alteration is not evident.

6.4.9 Recommendations for future work

When comparing soil-like material samples with correlation values in the literature, I noticed that most studies deal entirely with clay-bearing sediments. The focus is less on hydrothermally altered material, which seems different. La Soufrière is not the only volcano worldwide, where hot, acidic fluids circulate and transform the rocks. Therefore, further research with this overprinted material from volcanic domes, which has not mobilized yet, would definitely be interesting and promising for better parameterization of assessment of slope movements. Especially the samples from the landslide and shear zone (KSL_10 - KSL_13) proved to be exceptional. Further geotechnical and geochemical studies from these areas would be recommended. They would fill a lack in the literature.
From raw material geology point of view, especially the area around sampling site KSL_13 would prove to be exciting, as the Cu and Zn grades stand out with 0,1 %. Such epithermal or hydrothermal systems often have smaller deposits.

7 Conclusion

The following conclusions can be drawn: there is a direct correlation between the secondary minerals and the alteration types.
While smectite occurs only in the argillic altered zones around the summit, the samples that could be assigned to advanced argillic alteration contain none.
Smectite has a positive influence on the cohesion, the friction angle and the shear strength. A higher smectite content increases the liquid limit and plastic limit but has no effect on the plasticity. In contrast, the water content decreases with increasing amount of this clay mineral.

In comparison, opal content has a negative effect on the plasticity and a positive one on water content and liquid limit or plastic limit. This amorphous silica occurs only in advanced argillic hydrothermally influenced material. KSL_7 was taken directly next to a fumarole and includes opal, as do the samples from the fault zones. It has no effect on the shear strength but increases cohesion and decreases the friction angle. This could explain why a lot of the mineral was found in the very zones of weakness of the volcano.

Kaolinite/Halloysite has the same effect on the shear parameters. The higher the amount of the clay mineral is, the higher the cohesion but the lower the friction angle is. This has an overall positive effect on the shear strength.
This clay mineral increases mainly with progressive hydrothermal influence. It shows no increase in samples with argillic alteration, but the amount raises drastically for samples with advanced argillic alteration.
According to the results of the Atterberg limits, the plasticity index and the liquid limit also increase with the increase of this secondary mineral. In contrast, kaolinite/halloysite lowers the plastic limit and the water content. This could be related to the emplacement of water molecules in the crystal lattice.

The progress of the alteration does not show any influence on the grain density or the distribution of the particle sizes.

In general, it can be argued that the cohesion and the friction angle in the soil like material samples from La Soufrière are not influenced by increasing alteration. Only the shear strength shows slightly enhancing values with it.

The progression of alteration is spatially variable, with no clear link to distance from active craters, such that alteration-induced material weaking cannot be identified easily at the surface. For example, KSL_4 and KSL_5, which were actually taken in the crater area and far from vegetation, were found to be less altered than samples taken closer to vegetated areas. Also the samples KSL_2, KSL_8 and KSL_9, which were considered to have a decreasing trend of alteration due to the increasing proximity to live vegetation, do not show this in the mineralogy.

Only the samples taken from an active fumarole (KSL_7), the landslide (KSL_10) and fumarolic fault (KSL_13) have advanced argillic alteration. Here the acid sulfate fluids seem to circulate more strongly to the surface. The mineral assemblages of the secondary minerals of all samples confirms they were formed by cooled (below 350°C, and down to 150°C – 200°C), acidic (pH < 4) hydrothermal fluids, mixed with meteoric water.

8 References

Allen, R.W., Collier, J.S., Stewart, A.G., Henstock, T., Goes, S., Rietbrock, A., 2019. The role of arc migration in the development of the Lesser Antilles: A new tectonic model for the Cenozoic evolution of the eastern Caribbean. Geol 47 (9), 891–895. doi:10.1130/G46708.1.

Bain, J.A., 1971. A plasticity chart as an aid to the identification and assessment of industrial clays. Clay miner. 9 (1), 1–17. doi:10.1180/claymin.1971.009.1.01.

Ball, J.L., Calder, E.S., Hubbard, B.E., Bernstein, M.L., 2013. An assessment of hydrothermal alteration in the Santiaguito lava dome complex, Guatemala: implications for dome collapse hazards. Bulletin of Volcanology 75 (1). doi:10.1007/s00445-012-0676-z.

Ball, J.L., Stauffer, P.H., Calder, E.S., Valentine, G.A., 2015. The hydrothermal alteration of cooling lava domes. Bulletin of Volcanology 77 (12). doi:10.1007/s00445-015-0986-z.

Ball, J.L., Taron, J., Reid, M.E., Hurwitz, S., Finn, C., Bedrosian, P., 2018. Combining Multiphase Groundwater Flow and Slope Stability Models to Assess Stratovolcano Flank Collapse in the Cascade Range. Journal of Geophysical Research: Solid Earth 123 (4), 2787–2805. doi:10.1002/2017jb015156.

Boekhout, F., Spikings, R., Sempere, T., Chiaradia, M., Ulianov, A., Schaltegger, U., 2012. Mesozoic arc magmatism along the southern Peruvian margin during Gondwana breakup and dispersal. Lithos 146-147, 48–64. doi:10.1016/j.lithos.2012.04.015.

Boschman, L.M., van Hinsbergen, D.J., Torsvik, T.H., Spakman, W., Pindell, J.L., 2014. Kinematic reconstruction of the Caribbean region since the Early Jurassic. Earth-Science Reviews 138, 102–136. doi:10.1016/j.earscirev.2014.08.007.

Boudon, G., Dagain, J., Semet, M.P., Westercamp, D., 1988. Notice explicative de la carte géologique à 1/20.000e du Massif volcanique de la Soufrière (Département de la Guadeloupe, Petites Antilles). Bureau de recherches géologiques et minières.

Boudon, G., Komorowski, J.-C., Villemant, B., Semet, M.P., 2008. A new scenario for the last magmatic eruption of La Soufrière of Guadeloupe (Lesser Antilles) in 1530 A.D. Evidence from stratigraphy radiocarbon dating and magmatic evolution of erupted products. Journal of Volcanology and Geothermal Research 178 (3), 474–490. doi:10.1016/j.jvolgeores.2008.03.006.

Bouysse, P., 1988. Opening of the Grenada back-arc Basin and evolution of the Caribbean plate during the Mesozoic and early Paleogene. Tectonophysics 149 (1-2), 121–143. doi:10.1016/0040-1951(88)90122-9.

Bouysse, P., Westercamp, D., 1988. Effets de la subduction de rides océaniques sur l'évolution d'un arc insulaire : l'exemple des Petites Antilles.

Bouysse, P., Westercamp, D., Andreieff, P., 1990. The Lesser Antilles Island Arc, in: Moore, J.C., Mascle, A. (Eds.), Proceedings of the Ocean Drilling Program, 110 Scientific Results, vol. 110. Ocean Drilling Program.

Boynton, C.H., Westbrook, G.K., Bott, M.H.P., Long, R.E., 1979. A seismic refraction investigation of crustal structure beneath the Lesser Antilles island

arc. Geophysical Journal International 58 (2), 371–393. doi:10.1111/j.1365-246X.1979.tb01031.x.

Braszus, B., Goes, S., Allen, R., Rietbrock, A., Collier, J., Harmon, N., Henstock, T., Hicks, S., Rychert, C.A., Maunder, B., van Hunen, J., Bie, L., Blundy, J., Cooper, G., Davy, R., Kendall, J.M., Macpherson, C., Wilkinson, J., Wilson, M., 2021. Subduction history of the Caribbean from upper-mantle seismic imaging and plate reconstruction. Nature Communications 12 (1), 4211. doi:10.1038/s41467-021-24413-0.

Brombach, T., Marini, L., Hunziker, J.C., 2000. Geochemistry of the thermal springs and fumaroles of Basse-Terre Island, Guadeloupe, Lesser Antilles. Bull Volcanol 61 (7), 477–490. doi:10.1007/PL00008913.

Brouwer, P., 2006. Grundlagen der Röntgenfluoreszenzanalyse (RFA): Eine Einführung: 2nd ed. Panalytical. Almelo, 66 pp.

Burke, K., 1988. Tectonic Evolution of the Caribbean. Annual Review of Earth and Planetary Sciences 16 (1), 201–230. doi:10.1146/annurev.ea.16.050188.001221.

Burke, K., Fox, P.J., Şengör, A.M.C., 1978. Buoyant ocean floor and the evolution of the Caribbean. J. Geophys. Res. 83 (B8), 3949. doi:10.1029/JB083iB08p03949.

Campbell, A.J., Danielson, L., Righter, K., Seagle, C.T., Wang, Y., Prakapenka, V.B., 2009. High pressure effects on the iron–iron oxide and nickel–nickel oxide oxygen fugacity buffers. Earth and Planetary Science Letters 286 (3-4), 556–564. doi:10.1016/j.epsl.2009.07.022.

Cecchi, E., van Wyk de Vries, B., Lavest, J.-M., 2004. Flank spreading and collapse of weak-cored volcanoes. Bulletin of Volcanology 67 (1), 72–91. doi:10.1007/s00445-004-0369-3.

Christeson, G.L., Mann, P., Escalona, A., Aitken, T.J., 2008. Crustal structure of the Caribbean-northeastern South America arc-continent collision zone. J. Geophys. Res. 113 (B8). doi:10.1029/2007JB005373.

Corbett, G., 2009. Geological models in epithermal - porphyry exploration: Terry Leach's Legacy. Geological Society of Australia. Specialist Group in Economic Geology. Newsletter 1.2 2009, 3–14.

Corbett, G.J., Leach, T.M., 1998. Southwest Pacific gold-copper systems: Structure, alteration and mineralization. Society of Economic Geologists Special Publication 6, 238 p.

Del Potro, R., Hürlimann, M., 2009. The decrease in the shear strength of volcanic materials with argillic hydrothermal alteration, insights from the summit region of Teide stratovolcano, Tenerife. Engineering Geology 104 (1-2), 135–143. doi:10.1016/j.enggeo.2008.09.005.

DeMets, C., Gordon, R.G., Argus, D.F., Stein, S., 1994. Effect of recent revisions to the geomagnetic reversal time scale on estimates of current plate motions. Geophys. Res. Lett. 21 (20), 2191–2194. doi:10.1029/94GL02118.

DeMets, C., Jansma, P.E., Mattioli, G.S., Dixon, T.H., Farina, F., Bilham, R., Calais, E., Mann, P., 2000. GPS geodetic constraints on Caribbean-North America Plate Motion. Geophys. Res. Lett. 27 (3), 437–440. doi:10.1029/1999GL005436.

Duncan, R., Hargraves, R.B., 1984. Plate tectonic evolution of the Caribbean region in the mantle reference frame. Geological Society of America Memoirs (162), 81–94.

Escuder-Viruete, J., Valverde-Vaquero, P., Rojas-Agramonte, Y., Jabites, J., Pérez-Estaún, A., 2013. From intra-oceanic subduction to arc accretion and arc-continent collision: Insights from the structural evolution of the Río San Juan metamorphic complex, northern Hispaniola. Journal of Structural Geology 46, 34–56. doi:10.1016/j.jsg.2012.10.008.

Feuillard, M., Allegre, C.J., Brandeis, G., Gaulon, R., Le Mouel, J.L., Mercier, J.C., Pozzi, J.P., Semet, M.P., 1983. The 1975–1977 crisis of la Soufriere de Guadeloupe (F.W.I): A still-born magmatic eruption. Journal of Volcanology and Geothermal Research 16 (3-4), 317–334. doi:10.1016/0377-0273(83)90036-7.

Finn, C.A., Deszcz-Pan, M., Anderson, E.D., John, D.A., 2007. Three-dimensional geophysical mapping of rock alteration and water content at Mount Adams, Washington: Implications for lahar hazards. J. Geophys. Res. 112 (B10). doi:10.1029/2006jb004783.

González, H., 2001. Mapa geologico del departamento de Antioquia y memoria explicitiva (Scale 1:400000). http://productos.ingeominas.gov.co/productos/.

Gonzalez De Vallejo, L.I., Jimenez Salas, J.A., Legy Jimenez, S., 1981. Engineering geology of the tropical volcanic soils of La Laguna, Tenerife. Engineering Geology 17 (1-2), 1–17. doi:10.1016/0013-7952(81)90018-1.

González de Vallejo, L.I., Ferrer, M., 2011. Geological engineering. CRC Press, an imprint of Taylor and Francis, Boca Raton, FL.

Gylland, A.S., Jostad, H.P., Nordal, S., 2014. Experimental study of strain localization in sensitive clays. Acta Geotech. 2014 (2), 227–240. doi:10.1007/s11440-013-0217-8.

Gylland, A.S., Rueslåtten, H., Jostad, H.P., Nordal, S., 2013. Microstructural observations of shear zones in sensitive clay. Engineering Geology 2013, 75–88. doi:10.1016/j.enggeo.2013.06.001.

Hastie, A.R., Kerr, A.C., 2010. Mantle plume or slab window?: Physical and geochemical constraints on the origin of the Caribbean oceanic plateau. Earth-Science Reviews 98 (3-4), 283–293. doi:10.1016/j.earscirev.2009.11.001.

Hauff, F., Hoernle, K., van den Bogaard, P., Alvarado, G., Garbe-Schönberg, D., 2000. Age and geochemistry of basaltic complexes in western Costa Rica: Contributions to the geotectonic evolution of Central America. Geochem. Geophys. Geosyst. 1 (5). doi:10.1029/1999GC000020.

Heap, M.J., Baumann, T.S., Rosas-Carbajal, M., Komorowski, J.-C., Gilg, H.A., Villeneuve, M., Moretti, R., Baud, P., Carbillet, L., Harnett, C., Reuschlé, T., 2021. Alteration-Induced Volcano Instability at La Soufrière de Guadeloupe (Eastern Caribbean). J. Geophys. Res. 126 (8). doi:10.1029/2021JB022514.

Hill, R.I., 1993. Mantle plumes and continental tectonics. Lithos 30 (3-4), 193–206. doi:10.1016/0024-4937(93)90035-B.

Hincks, T.K., Komorowski, J.-C., Sparks, S.R., Aspinall, W.P., 2014. Retrospective analysis of uncertain eruption precursors at La Soufrière volcano, Guadeloupe,

1975–77: volcanic hazard assessment using a Bayesian Belief Network approach. J Appl. Volcanol. 3 (1). doi:10.1186/2191-5040-3-3.

Hoernle, K., van den Bogaard, P., Werner, R., Lissinna, B., Hauff, F., Alvarado, G., Garbe-Schönberg, D., 2002. Missing history (16–71 Ma) of the Galápagos hotspot: Implications for the tectonic and biological evolution of the Americas. Geol 30 (9), 795. doi:10.1130/0091-7613(2002)030<0795:MHMOTG>2.0.CO;2.

John, D.A., Sisson, T.W., Breit, G.N., Rye, R.O., Vallance, J.W., 2008. Characteristics, extent and origin of hydrothermal alteration at Mount Rainier Volcano, Cascades Arc, USA: Implications for debris-flow hazards and mineral deposits. Journal of Volcanology and Geothermal Research 175 (3), 289–314. doi:10.1016/j.jvolgeores.2008.04.004.

Kerr, A.C., Marriner, G.F., Tarney, J., Nivia, A., Saunders, A.D., Thirlwall, M.F., Sinton, C.W., 1997. Cretaceous Basaltic Terranes in Western Columbia: Elemental, Chronological and Sr-Nd Isotopic Constraints on Petrogenesis. Journal of Petrology 38 (6), 677–702. doi:10.1093/petroj/38.6.677.

Komorowski, J.C., Boudon, G., Semet, M.P., Beauducel, F., Cheminée, J.-L., 2005. Guadeloupe, 64 pp.

Komorowski, J.C., Legendre, Y., Barsotti S., Esposti-Ongaro, T., Jenkins, S., Baxter, P., Boudon, G. Leone, Frederic, Neri, A., Spence R., Aspinall, W., Grancher, D., Redon, M., Chopineau, C., Chabalier, J.B. de, 2013a. Assessing long-term hazards for la Soufriere of Guadeloupe volcano : insights from a new eruptive chronology, credible scenario definition, and integrated impact modelling.

Komorowski, J.-C., Jenkins, S., Baxter, P.J., Picquout, A., Lavigne, F., Charbonnier, S., Gertisser, R., Preece, K., Cholik, N., Budi-Santoso, A., Surono, 2013b. Paroxysmal dome explosion during the Merapi 2010 eruption: Processes and facies relationships of associated high-energy pyroclastic density currents. Journal of Volcanology and Geothermal Research 261, 260–294. doi:10.1016/j.jvolgeores.2013.01.007.

Komorowski, J.-C., Legendre, Y., Caron, B., Boudon, G., 2008. Reconstruction and analysis of sub-plinian tephra dispersal during the 1530 A.D. Soufrière (Guadeloupe) eruption: Implications for scenario definition and hazards assessment. Journal of Volcanology and Geothermal Research 178 (3), 491–515. doi:10.1016/j.jvolgeores.2007.11.022.

Legendre, Y., 2012. Reconstruction fine de l'histoire éruptive et scénarii éruptifs à La Soufrière de Guadeloupe: vers un modèle intégré de fonctionnement du volcan. (French) [A high resolution reconstruction of the eruptive past and definition of eruptive scenaris at La Soufrière of Guadeloupe]. Ph.D. thesis, Paris 7 (2012).

Lherminier, 1837a. L˝eruption du volcan de la Guadeloupe. La Soufrière of Guadeloupe. Nouvelles Annales de Voyage 74, 349.

Lherminier, 1837b. Note sur l˝eruption du volcan de la Guadeloupe. (French). On the products from the volcano of La Guadeloupe. Comptes rendus de l'Acad´emie des sciences, 294.

Lherminier, 1837c. Sur les produits du volcan de la Guadeloupe. Comptes rendus de l'Académie des sciences, 454.

Litherland, 1994. The metamorphic belts of Ecuador. Brit. Geol. Surv. Overseas Mem., 11.

López, D.L., Williams, S.N., 1993. Catastrophic volcanic collapse: relation to hydrothermal processes. Science 260 (5115), 1794–1796. doi:10.1126/science.260.5115.1794.

Mann, P., Rogers, R.D., Gahagan, L., 2007. In Central America: Geology, Resources and Hazards (eds. Bundschuh, J. & Alvarado, G. E.) 205– 241 (Taylor and Francis, 2007).

Mauffret, A., Leroy, S., 1997. Seismic stratigraphy and structure of the Caribbean igneous province. Tectonophysics 283 (1-4), 61–104. doi:10.1016/S0040-1951(97)00103-0.

Metcalfe, A., Moune, S., Komorowski, J.-C., Moretti, R., 2022. Bottom-up vs top-down drivers of eruption style: Petro-geochemical constraints from the holocene explosive activity at La Soufrière de Guadeloupe.

Moretti, R., Komorowski, J.-C., Ucciani, G., Moune, S., Jessop, D., Chabalier, J.-B. de, Beauducel, F., Bonifacie, M., Burtin, A., Vallée, M., Deroussi, S., Robert, V., Gibert, D., Didier, T., Kitou, T., Feuillet, N., Allard, P., Tamburello, G., Shreve, T., Saurel, J.-M., Lemarchand, A., Rosas-Carbajal, M., Agrinier, P., Le Friant, A., Chaussidon, M., 2020. The 2018 unrest phase at La Soufrière of Guadeloupe (French West Indies) andesitic volcano: Scrutiny of a failed but prodromal phreatic eruption. Journal of Volcanology and Geothermal Research 393, 106769. doi:10.1016/j.jvolgeores.2020.106769.

Morgenstern, N.R., Tchalenko, J.S., 1967. Microscopic Structures in Kaolin Subjected to Direct Shear. Géotechnique 17 (4), 309–328. doi:10.1680/geot.1967.17.4.309.

Müller, R.D., Zahirovic, S., Williams, S.E., Cannon, J., Seton, M., Bower, D.J., Tetley, M.G., Heine, C., Le Breton, E., Liu, S., Russell, S.H.J., Yang, T., Leonard, J., Gurnis, M., 2019. A Global Plate Model Including Lithospheric Deformation Along Major Rifts and Orogens Since the Triassic. Tectonics 38 (6), 1884–1907. doi:10.1029/2018TC005462.

Neill, I., Kerr, A.C., Hastie, A.R., Pindell, J.L., Millar, I.L., Atkinson, N., 2012. Age and Petrogenesis of the Lower Cretaceous North Coast Schist of Tobago, a Fragment of the Proto–Greater Antilles Inter-American Arc System. The Journal of Geology 120 (4), 367–384. doi:10.1086/665798.

Noble, S.R., Aspden, J.A., Jemielita, R., 1997. Northern Andean crustal evolution: New U-Pb geochronological constraints from Ecuador. Geological Society of America Bulletin 109 (7), 789–798. doi:10.1130/0016-7606(1997)109<0789:NACENU>2.3.CO;2.

ÖNORM EN ISO 17892-10, 2019. ÖNORM EN ISO 17892-10: Geotechnical investigation and testing - Laboratory testing of soil: Part 10: Direct shear tests. Austrian Standards International, Heinestraße 38, 1020 Wien 13.080.20; 93.020.

ÖNORM EN ISO 17892-12, 2021. ÖNORM EN ISO 17892-12: Geotechnical investigation and testing - Laboratory testing of soil: Part 12: Determination of

liquid and plastic limits. Austrian Standards International, Heinestraße 38, 1020 Wien 13.080.20; 93.020.

ÖNORM EN ISO 17892-4, 2017. ÖNORM EN ISO 17892-4: Geotechnical investigation and testing - Laboratory testing of soil: Part 4: Determination of particle size distribution. Austrian Standards International, Heinestraße 38, 1020 Wien 13.080.20; 93.020.

Opfergelt, S., Delmelle, P., Boivin, P., Delvaux, B., 2006. The 1998 debris avalanche at Casita volcano, Nicaragua: Investigation of the role of hydrothermal smectite in promoting slope instability. Geophysical Research Letters 33 (15). doi:10.1029/2006gl026661.

Padron C., 2020. Deep structure of the Grenada Basin from wide-angle seismic, bathymetric and gravity data. Journal of Geophysical Research: Solid Earth 126, e2020JB020472.

Pindell, 2009. Tectonic evolution of the Gulf of Mexico, Caribbean and northern South America in the mantle reference frame: an update 328, 1.

Pindell, J.L., Cande, S., Pitman, W.C., Rowley, D.B., Dewey, J.F., Labrecque, J., Haxby, W., 1988. A plate-kinematic framework for models of Caribbean evolution. Tectonophysics 155 (1-4), 121–138. doi:10.1016/0040-1951(88)90262-4.

Pindell, J.L., Kennan, L., 2009. Tectonic evolution of the Gulf of Mexico, Caribbean and northern South America in the mantle reference frame: an update. Geological Society, London, Special Publications 328 (1), 1–55. doi:10.1144/SP328.1.

Reid, M.E., Sisson, T.W., Brien, D.L., 2001. Volcano collapse promoted by hydrothermal alteration and edifice shape, Mount Rainier, Washington. Geology 29 (9), 779. doi:10.1130/0091-7613(2001)029<0779:vcpbha>2.0.co;2.

Révillon, S., Hallot, E., Arndt, N.T., Chauvel, C., Duncan, R.A., 2000. A Complex History for the Caribbean Plateau: Petrology, Geochemistry, and Geochronology of the Beata Ridge, South Hispaniola. The Journal of Geology 108 (6), 641–661. doi:10.1086/317953.

Reyes, A., 1991. Mineralogy, distribution and origin of acid alteration in Philippine geothermal systems. Chishitsu Chosajo Hokoku (Report, Geological Survey of Japan), 277. https://www.osti.gov/etdeweb/biblio/7246532.

Rietveld, H.M., 1969. A profile refinement method for nuclear and magnetic structures. J Appl Crystallogr 2 (2), 65–71. doi:10.1107/S0021889869006558.

Rosas-Carbajal, M., Komorowski, J.-C., Nicollin, F., Gibert, D., 2016. Volcano electrical tomography unveils edifice collapse hazard linked to hydrothermal system structure and dynamics. Scientific Reports 6 (1), 29899. doi:10.1038/srep29899.

Salaün, A., Villemant, B., Gérard, M., Komorowski, J.-C., Michel, A., 2011. Hydrothermal alteration in andesitic volcanoes: Trace element redistribution in active and ancient hydrothermal systems of Guadeloupe (Lesser Antilles). Journal of Geochemical Exploration 111 (3), 59–83. doi:10.1016/j.gexplo.2011.06.004.

Saunders, A.D., Tarney, J., Kerr, A.C., Kent, R.W., 1996. The formation and fate of large oceanic igneous provinces. Lithos 37 (2-3), 81–95. doi:10.1016/0024-4937(95)00030-5.

Schlaphorst, D., Harmon, N., Kendall, J.M., Rychert, C.A., Collier, J., Rietbrock, A., Goes, S., 2021. Variation in Upper Plate Crustal and Lithospheric Mantle Structure in the Greater and Lesser Antilles From Ambient Noise Tomography. Geochem. Geophys. Geosyst. 22 (7). doi:10.1029/2021GC009800.

Schmitt, J., Burbaum, U., Bormann, A., 2021. Simmer Grundbau, 20th ed. Springer Vieweg, Wiesbaden, Heidelberg, 622 pp.

Siebert, L., 1984. Large volcanic debris avalanches: Characteristics of source areas, deposits, and associated eruptions. Journal of Volcanology and Geothermal Research 22 (3-4), 163–197. doi:10.1016/0377-0273(84)90002-7.

Siebert, L., Glicken, H., Ui, T., 1987. Volcanic hazards from Bezymianny- and Bandai-type eruptions. Bulletin of Volcanology 49 (1), 435–459. doi:10.1007/bf01046635.

Siebert, L., Kimberly, P., Simkin, T., 2010. Volcanoes of the World: Third Edition. University of California Press, Berkeley, CA. doi:10.1525/9780520947931, 568 pp.

Sinton, C.W., Duncan, R.A., Denyer, P., 1997. Nicoya Peninsula, Costa Rica: A single suite of Caribbean oceanic plateau magmas. J. Geophys. Res. 102 (B7), 15507–15520. doi:10.1029/97JB00681.

Sinton, C.W., Duncan, R.A., Storey, M., Lewis, J., Estrada, J.J., 1998. An oceanic flood basalt province within the Caribbean plate. Earth and Planetary Science Letters 155 (3-4), 221–235. doi:10.1016/S0012-821X(97)00214-8.

Skempton, A.W., 1964. Long-Term Stability of Clay Slopes. Géotechnique 14 (2), 77–102. doi:10.1680/geot.1964.14.2.77.

Taran, Y., Kalacheva, E., 2020. Acid sulfate-chloride volcanic waters; Formation and potential for monitoring of volcanic activity. Journal of Volcanology and Geothermal Research 405, 107036. doi:10.1016/j.jvolgeores.2020.107036.

van Wyk de Vries, B., Francis, P.W., 1997. Catastrophic collapse at stratovolcanoes induced by gradual volcano spreading. Nature 387 (6631), 387–390. doi:10.1038/387387a0.

Villagómez, 2008. Thermotectonic history of the Northern Andes, 573.

Villemant, B., Hammouya, G., Michel, A., Semet, M.P., Komorowski, J.-C., Boudon, G., Cheminée, J.-L., 2005. The memory of volcanic waters: Shallow magma degassing revealed by halogen monitoring in thermal springs of La Soufrière volcano (Guadeloupe, Lesser Antilles). Earth and Planetary Science Letters 237 (3-4), 710–728. doi:10.1016/j.epsl.2005.05.013.

Villemant, B., Komorowski, J.C., Dessert, C., Michel, A., Crispi, O., Hammouya, G., Beauducel, F., Chabalier, J.B. de, 2014. Evidence for a new shallow magma intrusion at La Soufrière of Guadeloupe (Lesser Antilles). Journal of Volcanology and Geothermal Research 285, 247–277. doi:10.1016/j.jvolgeores.2014.08.002.

Voight B., 2002. The eruption of Soufrière Hills volcano, Montserrat, from 1995 to 1999, 363 pp.

Wadge, G., Shepherd, J.B., 1984. Segmentation of the Lesser Antilles subduction zone. Earth and Planetary Science Letters 71 (2), 297–304. doi:10.1016/0012-821X(84)90094-3.

Watters, R.J., R. Zimbelman, S.D.B.D., 2000. Rock Mass Strength Assessment and Significance to Edifice Stability, Mount Rainier and Mount Hood, Cascade Range Volcanoes. Pure and Applied Geophysics 157 (6-8), 957–976. doi:10.1007/s000240050012.

Wesley, L.D., 1973. Some basic engineering properties of halloysite and allophane clays in Java, Indonesia. Géotechnique 23 (4), 471–494. doi:10.1680/geot.1973.23.4.471.

9 List of figures

10 List of tables

11 Table of equations

Appendix

11.1 Appendix A – Results XRD analysis

Mineral	KSL_2	KSL_4	KSL_5	KSL_7	KSL_8	KSL_9	KSL_10	KSL_11	KSL_12	KSL_13
Plagioclase (and.)	31	30	41		32	37				
Pyroxenes (opx+cpx)	12	6	12	5	9	11		6		
Amphiboles (hbl)	3	2	2		<1	2				
Quartz[a)]	2	2	1	1	2	2	<1			1
Tridymite, low [a)]	11	18	14	22	18	16				
Cristobalite [a)]				2			8	1		5
Opal - A [a)]				42			10	10		89
Smectite - dioct. [a)]	35	37	24		23	14		23		
Kaolinite / Halloysite [a)]	6	5	5	18	10	6	69	60	96	
Na- Alunite [a)]	<<1	<1		6	4	3	7			
Gypsum [a)]						1				
Pyrite [a)]				4		4	5		2	1
Marcasite [a)]							1		<1	
Anatase [a)]									1	2
Ferrihydrite? [a)]							X		X	X
(9.4A broad Talc?) [a)]	x	x	x		xx	xx				

Note. Values in wt.%

[a)] A secondary/alteration mineral

11.2 Appendix B - Results XRF analysis

		KSL2	KSL4	KSL5	KSL7	KSL8	KSL9	KSL10	KSL11	KSL12	KSL-13
Sum	%	94,99	94,61	95,08	89,01	91,76	94,25	83,02	89,02	84,90	88,36
LOI	%	5,40	5,84	5,11	12,93	8,78	5,56	16,51	10,99	14,73	12,63
SiO2	%	58,23	62,69	62,18	72,27	57,89	57,51	47,17	54,18	44,48	81,85
TiO2	%	0,84	1,02	0,84	1,01	0,85	0,74	0,80	1,06	1,23	1,94
Al2O3	%	16,28	12,33	14,44	8,24	15,84	17,10	23,77	23,49	33,07	1,04
Fe2O3	%	11,84	11,77	10,65	3,99	9,45	9,18	9,18	6,28	4,98	2,09
MnO	%	0,10	0,11	0,08	0,05	0,10	0,10	0,02	0,10	0,03	0,01
MgO	%	2,74	2,85	2,10	1,21	2,58	2,67	0,20	3,27	0,80	0,30
CaO	%	2,67	1,80	2,45	0,66	2,69	4,37	0,46	0,38	0,02	0,66
Na2O	%	1,39	1,07	1,42	0,63	1,40	1,78	0,43	0,02	0,00	0,10
K2O	%	0,66	0,70	0,72	0,62	0,71	0,63	0,72	0,04	0,04	0,05
P2O5	%	0,13	0,17	0,12	0,10	0,15	0,11	0,12	0,05	0,10	0,03
Ba	ppm	210	188	141	353	220	133	251	200	150	212
Ce	ppm	<51	<51	70	<51	<51	<51	<51	<51	<51	<51
Co	ppm	24	8	<7	19	12	12	13	21	32	11
Cr	ppm	24	28	17	15	30	24	83	36	64	85
Cu	ppm	57	39	45	633	87	102	187	298	84	1007
Ga	ppm	19	21	19	27	19	16	34	27	30	5
La	ppm	<40	<40	<40	<40	43	<40	<40	<40	<40	<40
Nb	ppm	5	4	7	7	5	5	5	5	7	6
Ni	ppm	<4	<4	<4	<4	<4	<4	20	9	6	37
Pb	ppm	114	135	22	39	112	21	262	24	325	67
Rb	ppm	26	28	26	22	27	25	26	14	13	15
Sr	ppm	129	105	144	195	146	185	401	12	36	37
Th	ppm	13	11	15	<9	16	11	13	<9	17	12

V	ppm	168	210	155	121	159	145	225	251	518	195
Y	ppm	8	10	6	<3	5	6	<3	<3	<3	<3
Zn	ppm	134	102	74	639	83	80	89	478	25	1038
Zr	ppm	85	98	93	139	99	81	102	92	123	180

11.3 Appendix C – Diagrams of secondary minerals vs. alteration

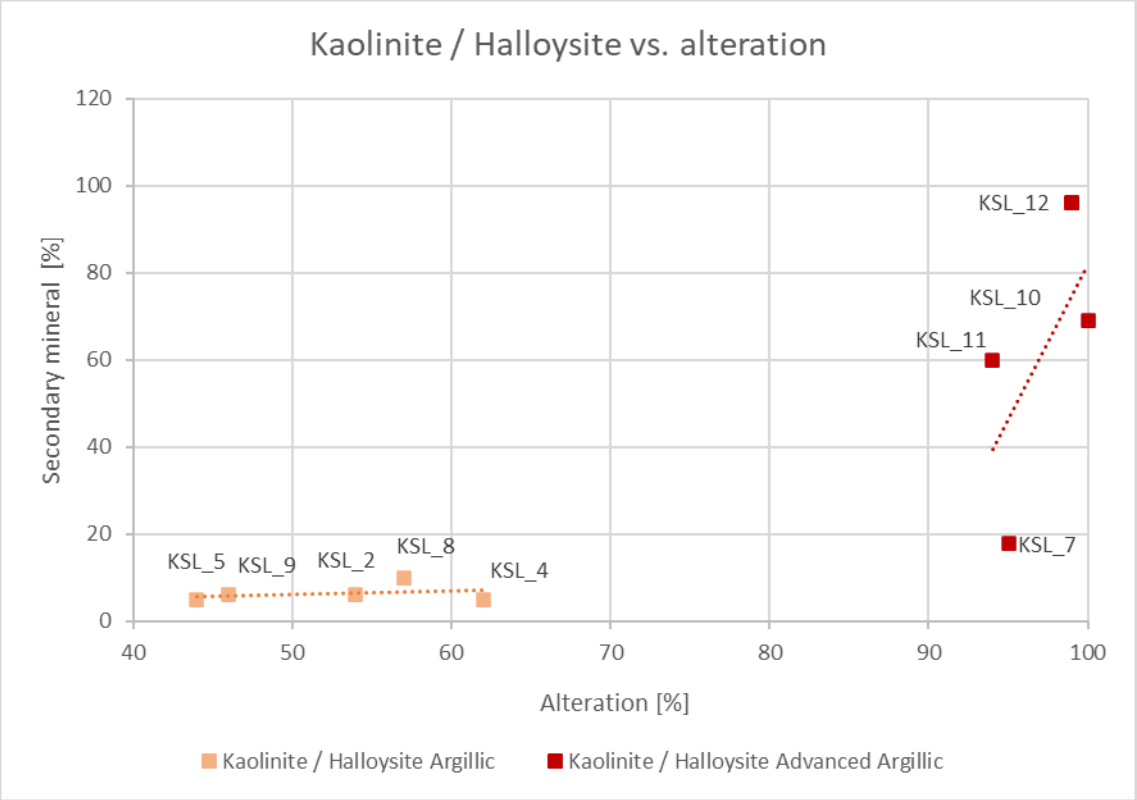

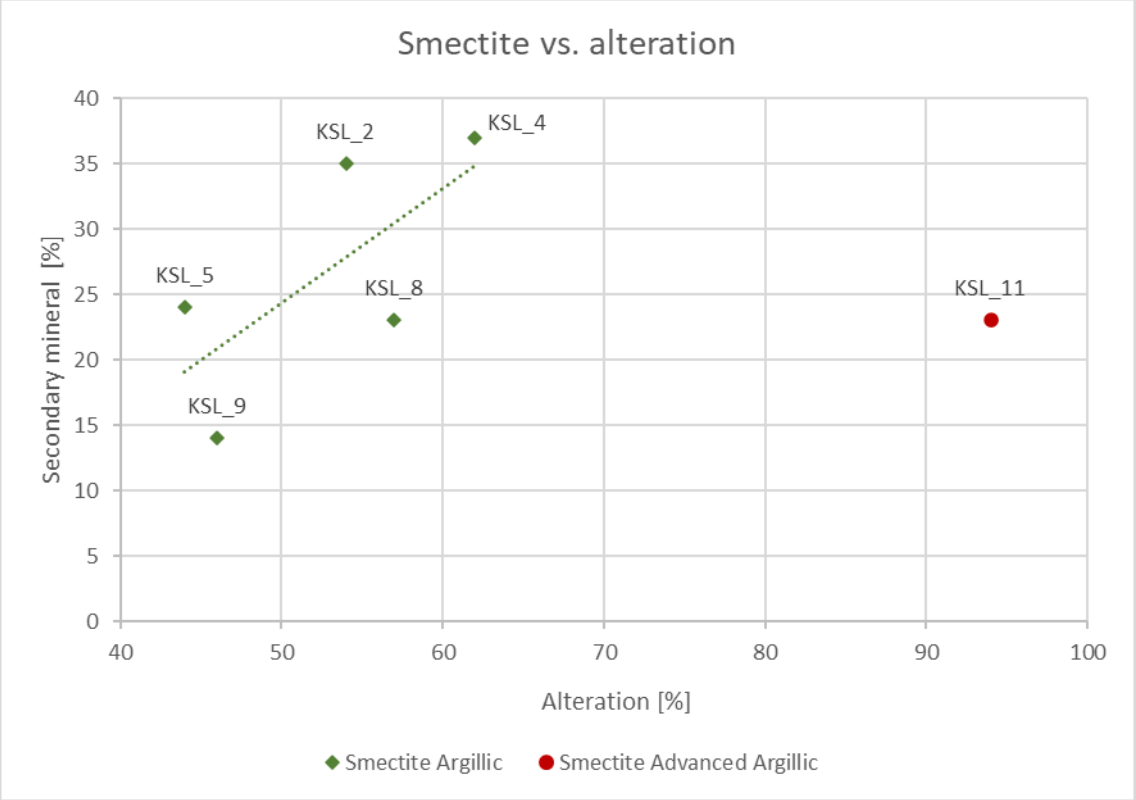

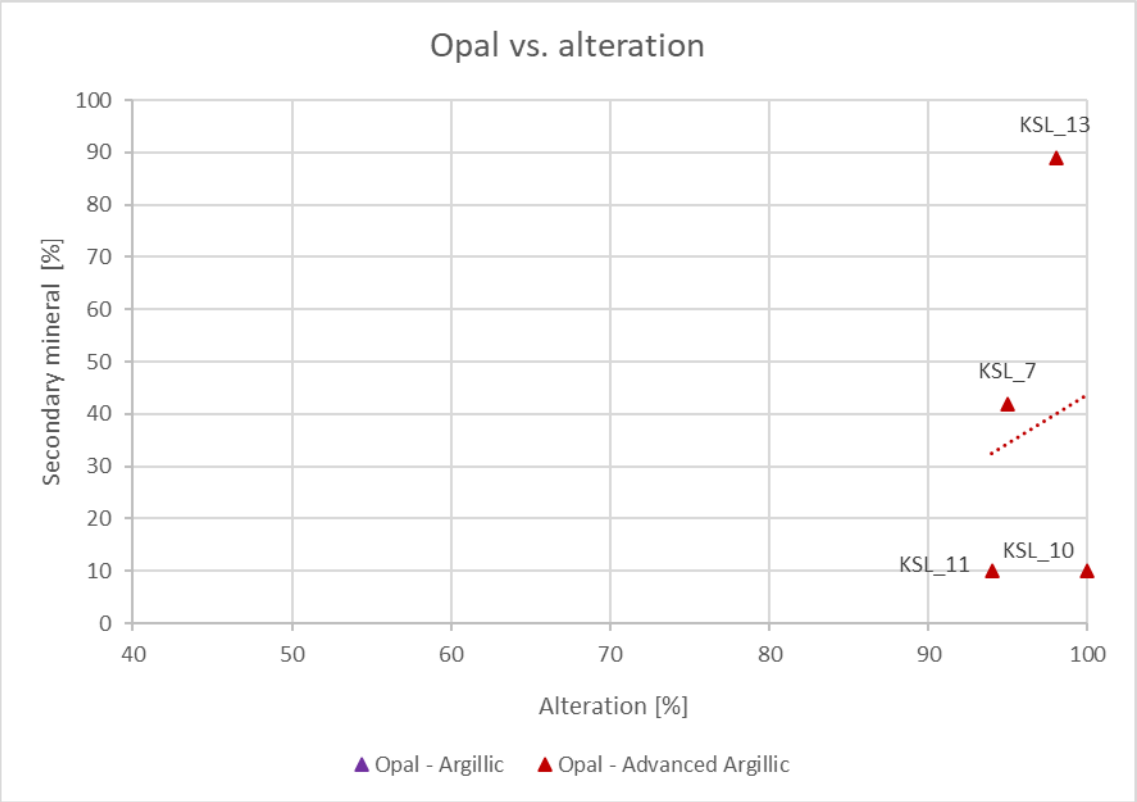
Opal vs. alteration
Secondary mineral [%]
100
90
80
70
60
50
40
30
20
10
0
40
50
60
70
80
90
100
Alteration [%]
KSL_13
KSL_7
KSL_11
KSL_10
Opal - Argillic
Opal - Advanced Argillic

11.4 Appendix D – Diagrams secondary minerals vs. shear parameter

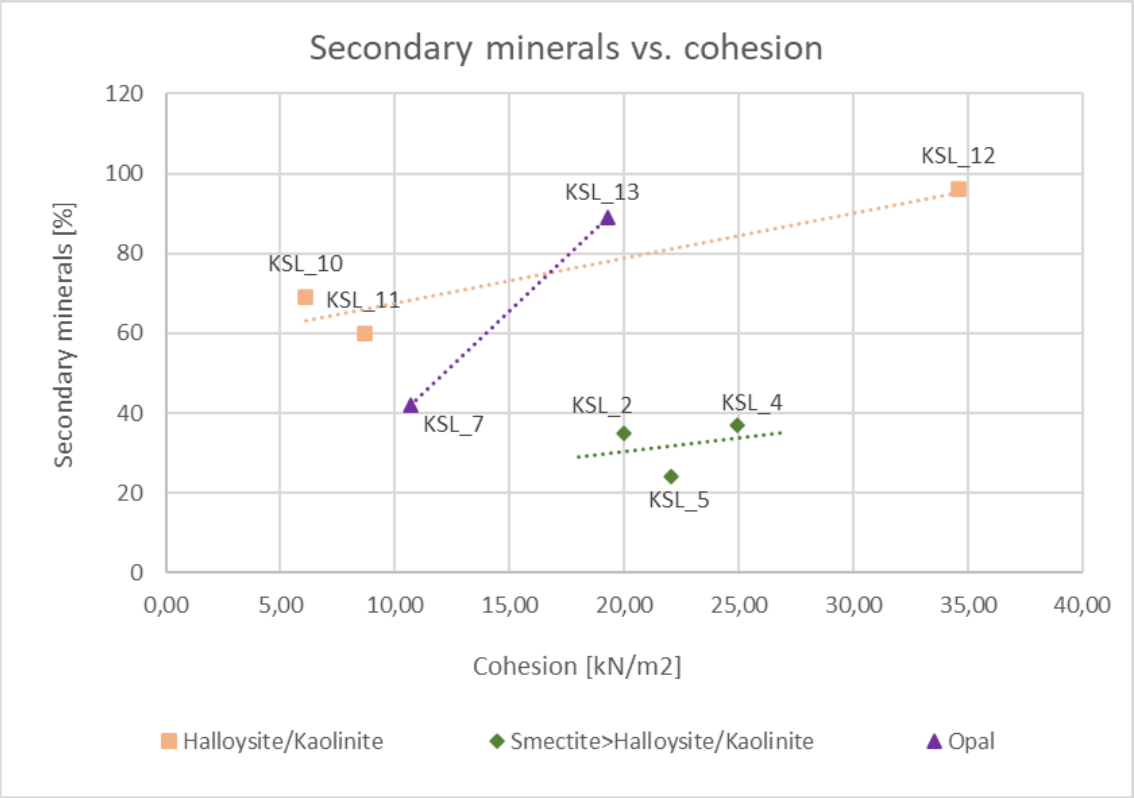

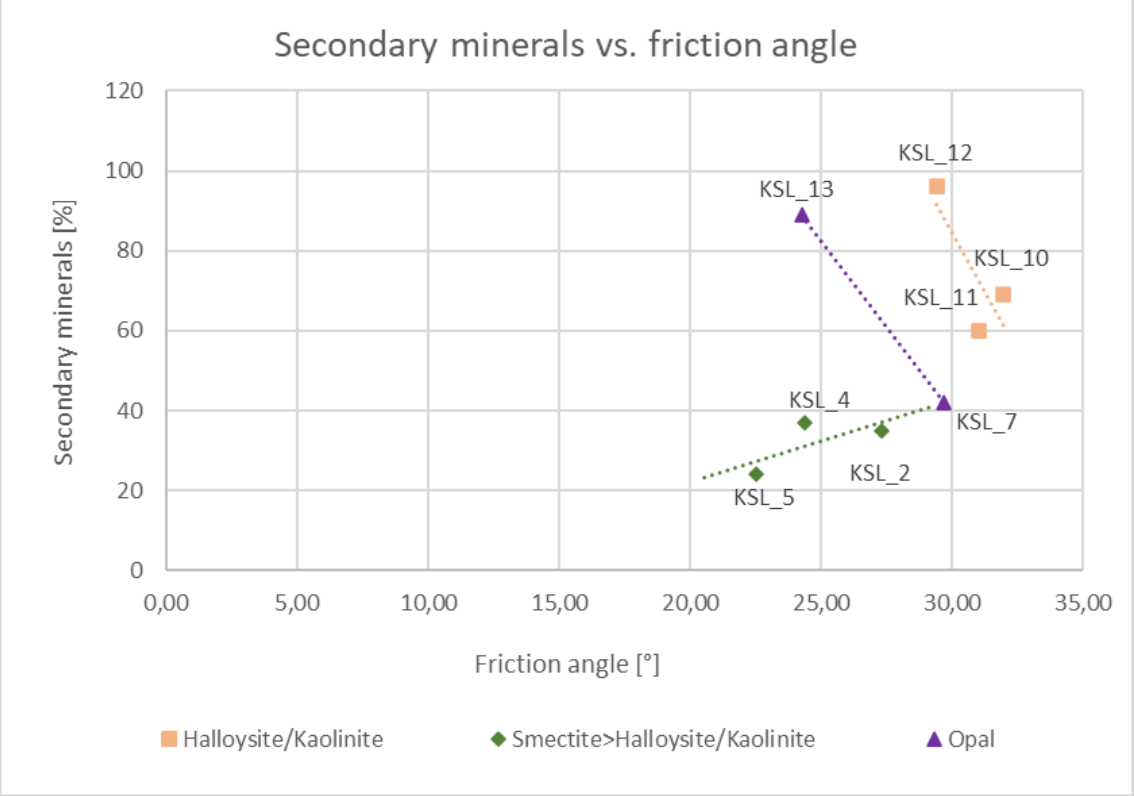

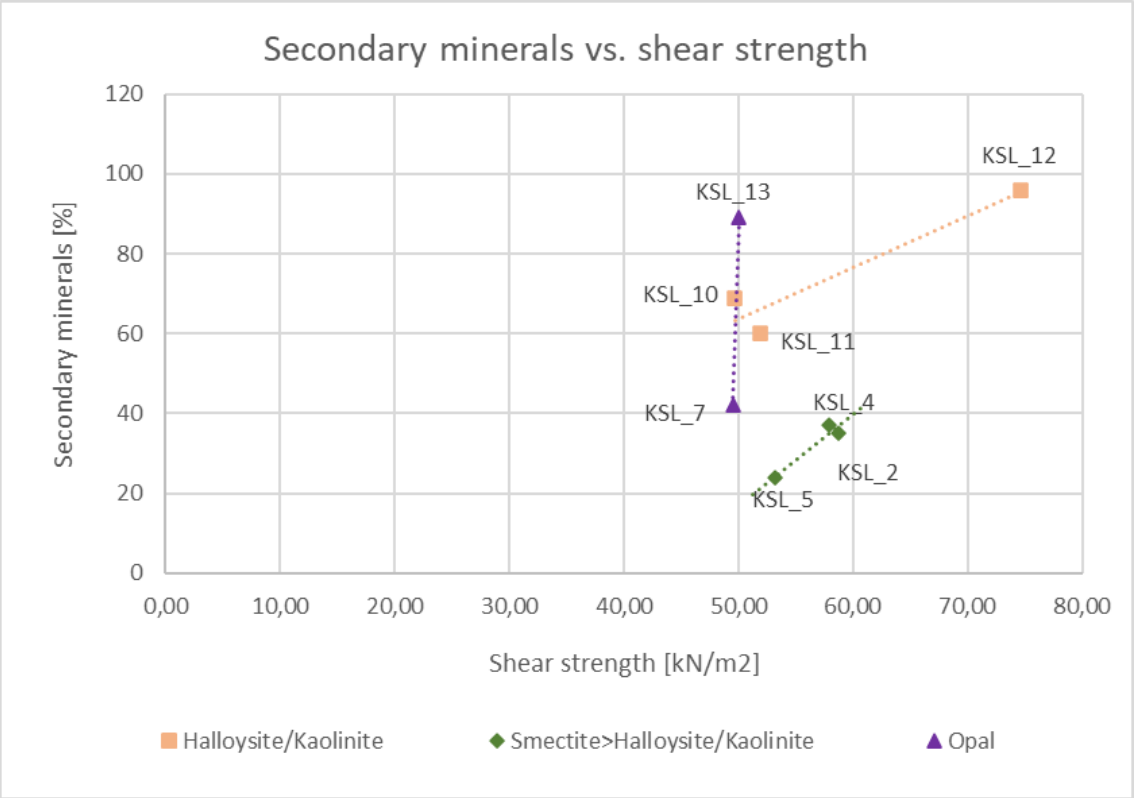
Secondary minerals vs. shear strength
Secondary minerals [%]
120
100
80
60
40
20
0
0,00
10,00
20,00
30,00
40,00
50,00
60,00
70,00
80,00
Shear strength [kN/m2]
KSL_12
KSL_13
KSL_10
KSL_11
KSL_7
KSL_4
KSL_2
KSL_5
Halloysite/Kaolinite
Smectite>Halloysite/Kaolinite
Opal

11.5 Appendix E – Diagrams shear parameter vs. alteration

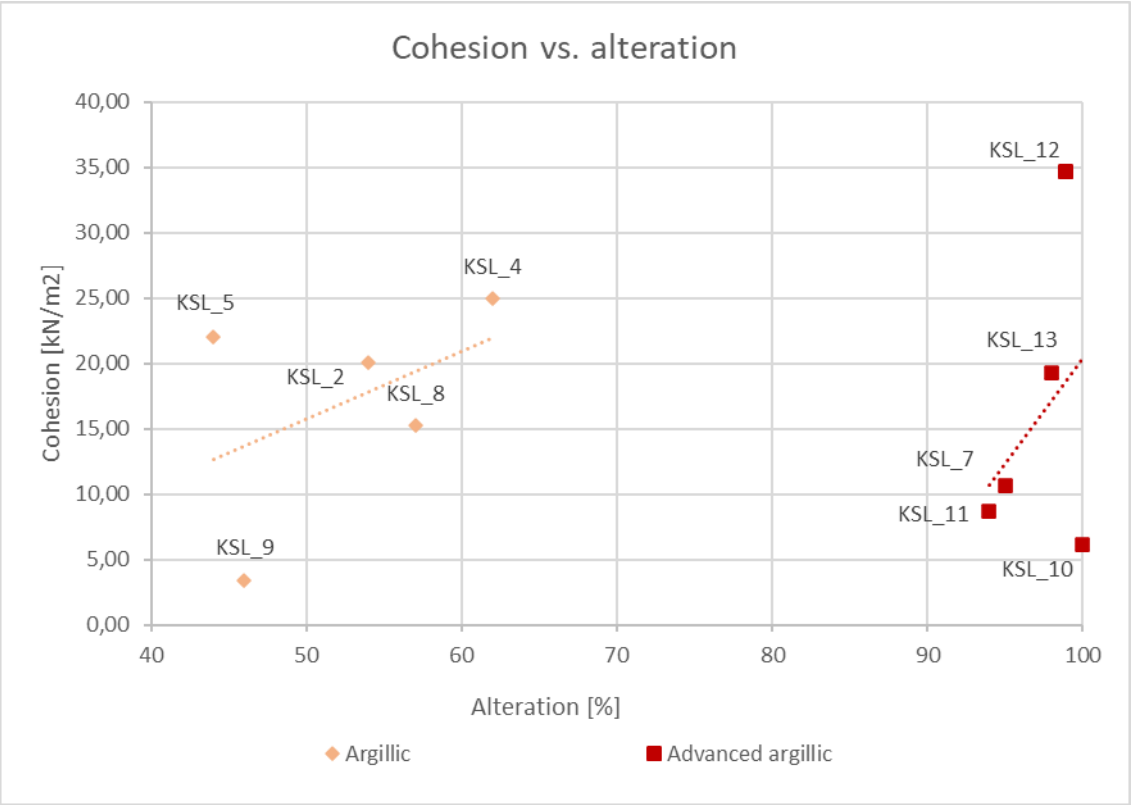

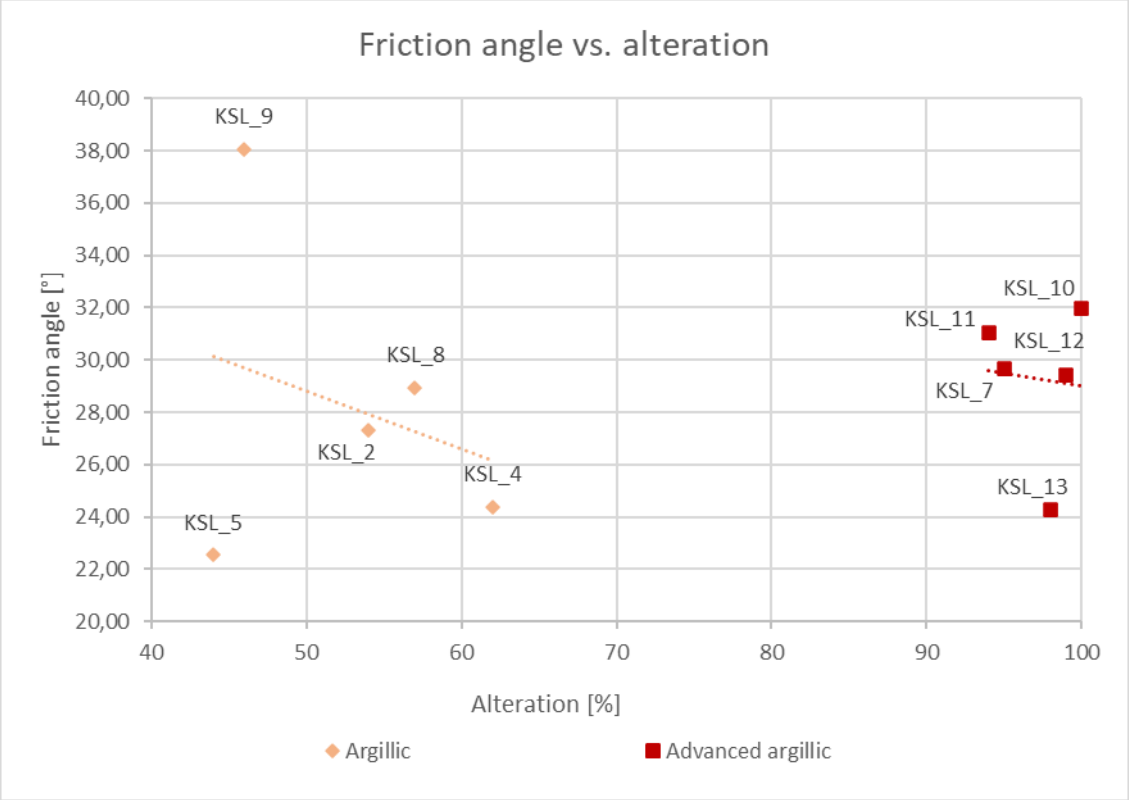

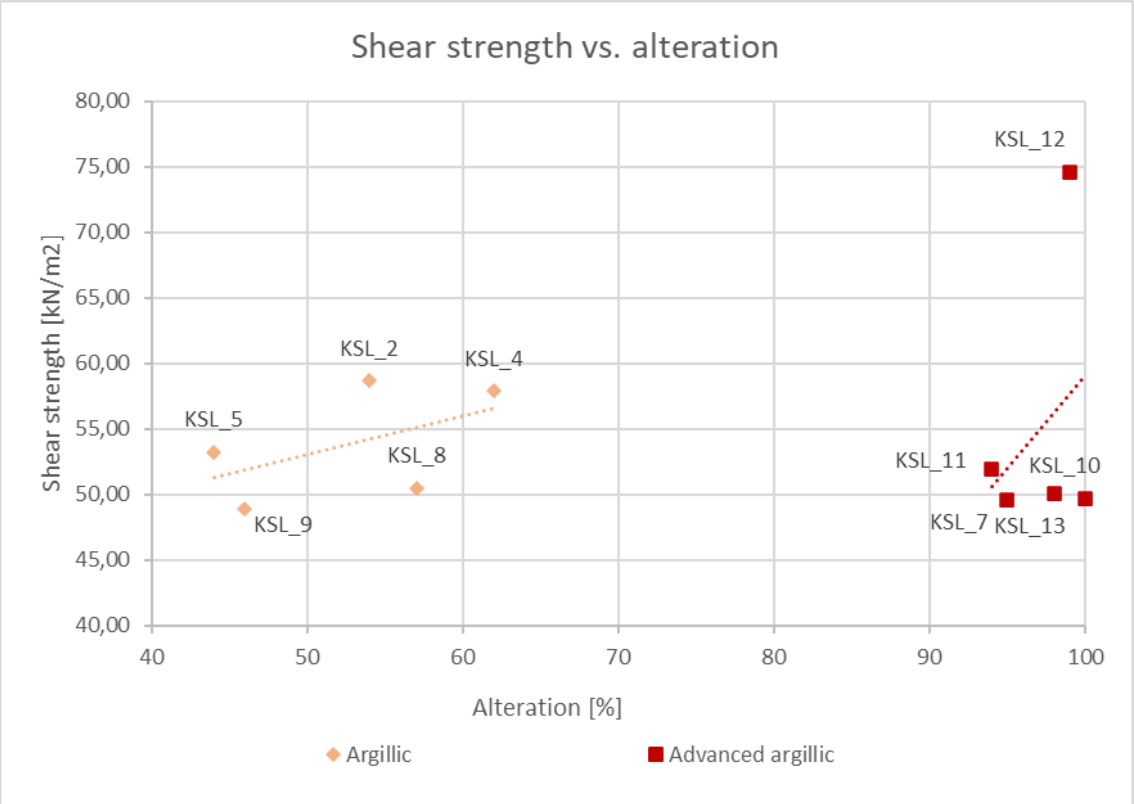
Shear strength vs. alteration
Shear strength [kN/m2]
80,00
75,00
70,00
65,00
60,00
55,00
50,00
45,00
40,00
40
50
60
70
80
90
100
Alteration [%]
KSL_12
KSL_2
KSL_4
KSL_5
KSL_8
KSL_11
KSL_10
KSL_9
KSL_7
KSL_13
Argillic
Advanced argillic

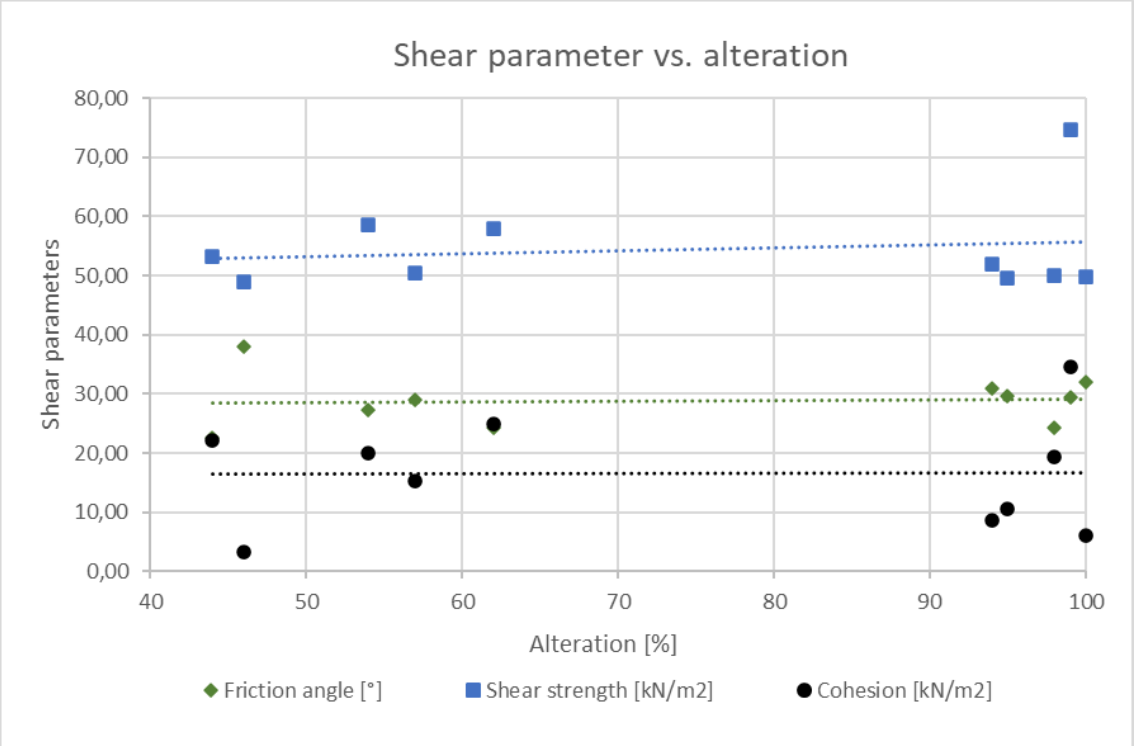
Shear parameter vs. alteration
Shear parameters
80,00
70,00
60,00
50,00
40,00
30,00
20,00
10,00
0,00
40
50
60
70
80
90
100
Alteration [%]
Friction angle [°]
Shear strength [kN/m2]
Cohesion [kN/m2]

11.6 Appendix F – Diagrams of secondary minerals vs. Atterberg limits

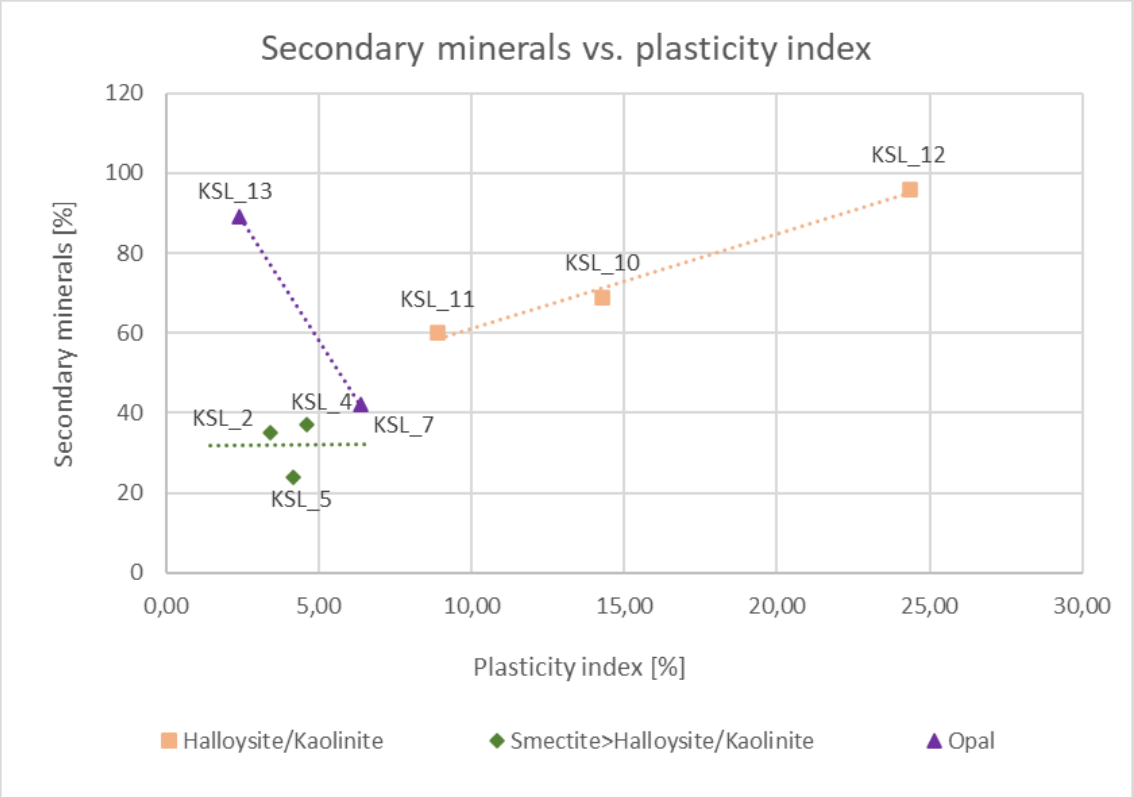

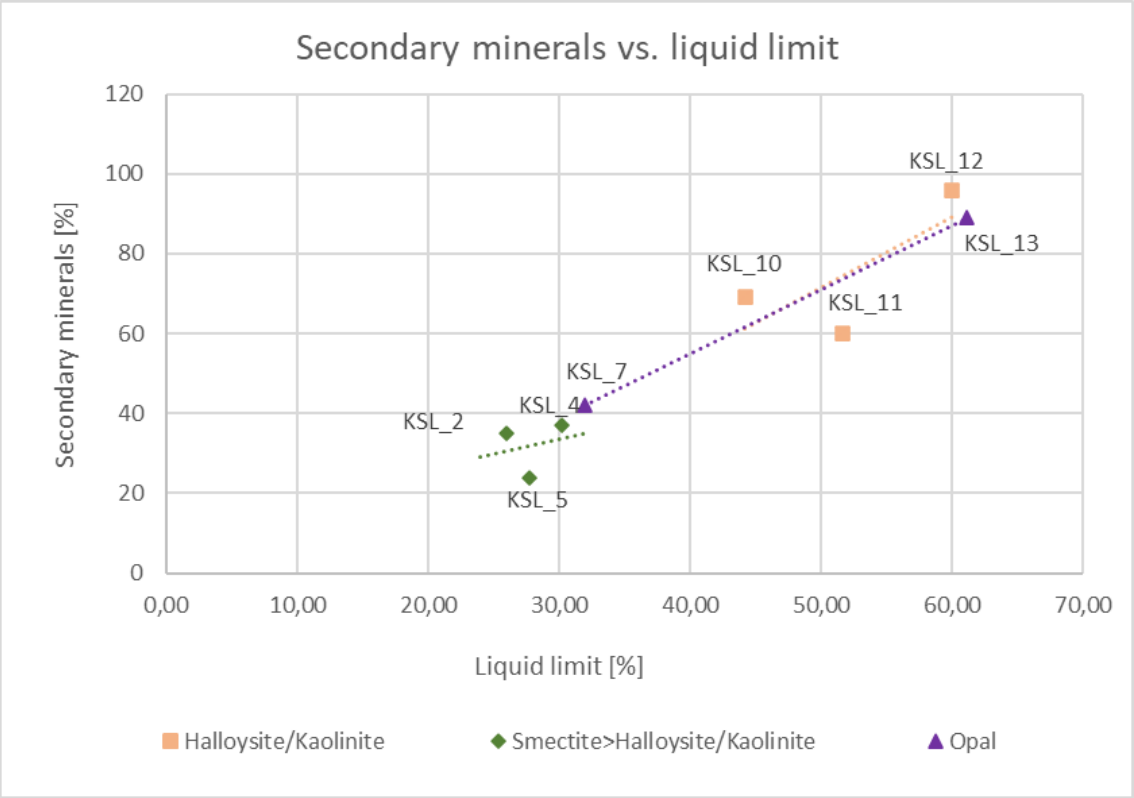

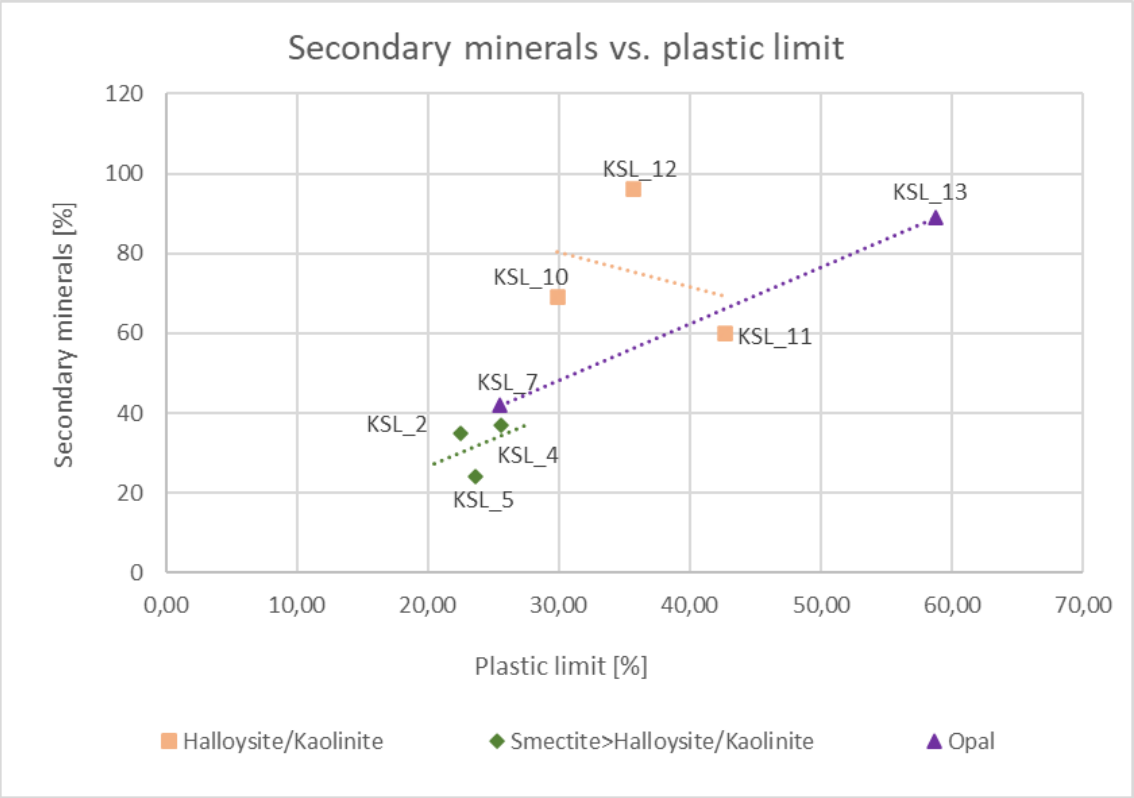
Secondary minerals vs. plastic limit
Secondary minerals [%]
120
100
80
60
40
20
0
0,00
10,00
20,00
30,00
40,00
50,00
60,00
70,00
Plastic limit [%]
KSL_12
KSL_13
KSL_10
KSL_11
KSL_7
KSL_2
KSL_4
KSL_5
Halloysite/Kaolinite
Smectite>Halloysite/Kaolinite
Opal

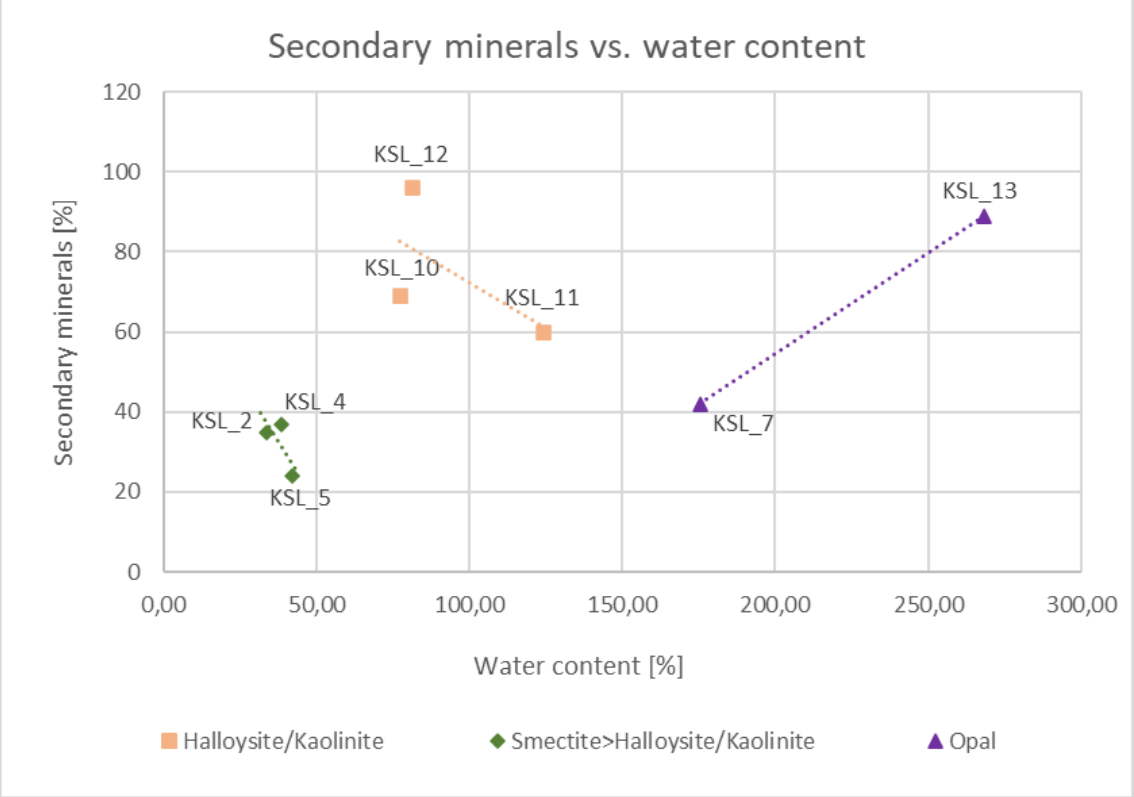
Secondary minerals vs. water content
Secondary minerals [%]
120
100
80
60
40
20
0
0,00
50,00
100,00
150,00
200,00
250,00
300,00
Water content [%]
KSL_12
KSL_13
KSL_10
KSL_11
KSL_4
KSL_2
KSL_7
KSL_5
Halloysite/Kaolinite
Smectite>Halloysite/Kaolinite
Opal

11.7 Appendix G – Diagrams of shear parameter vs. Atterberg limits considering clay minerals

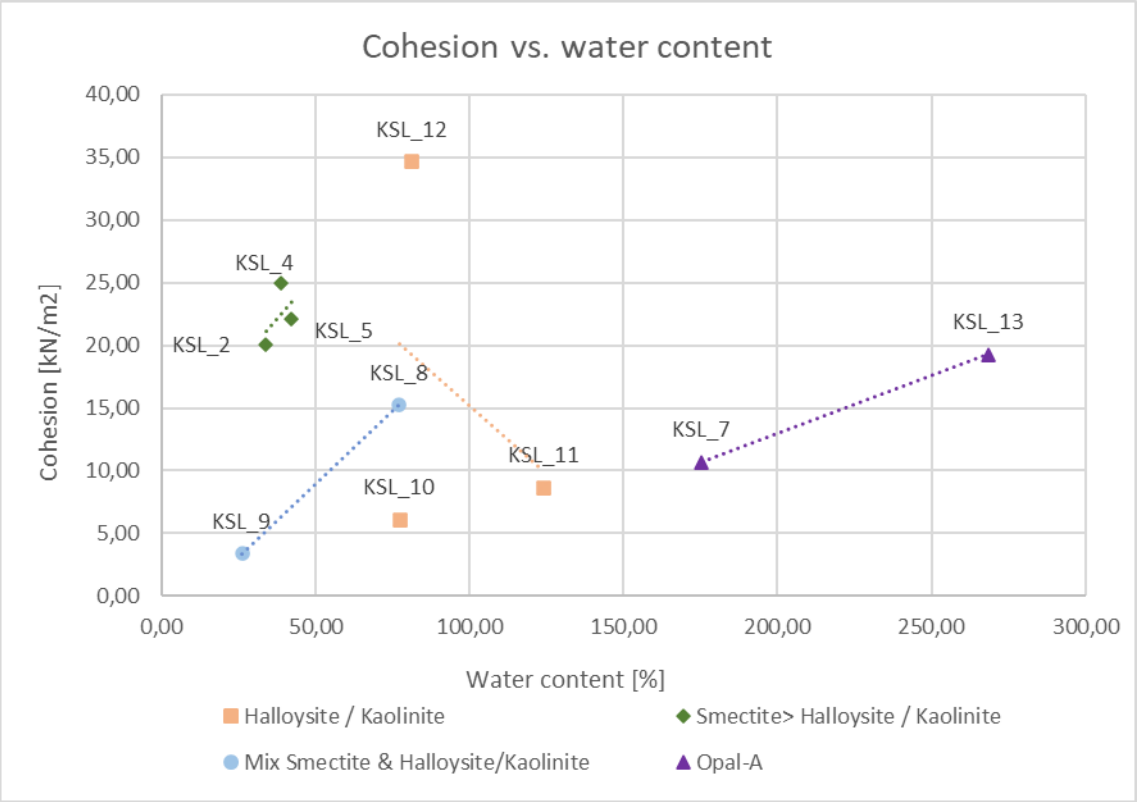

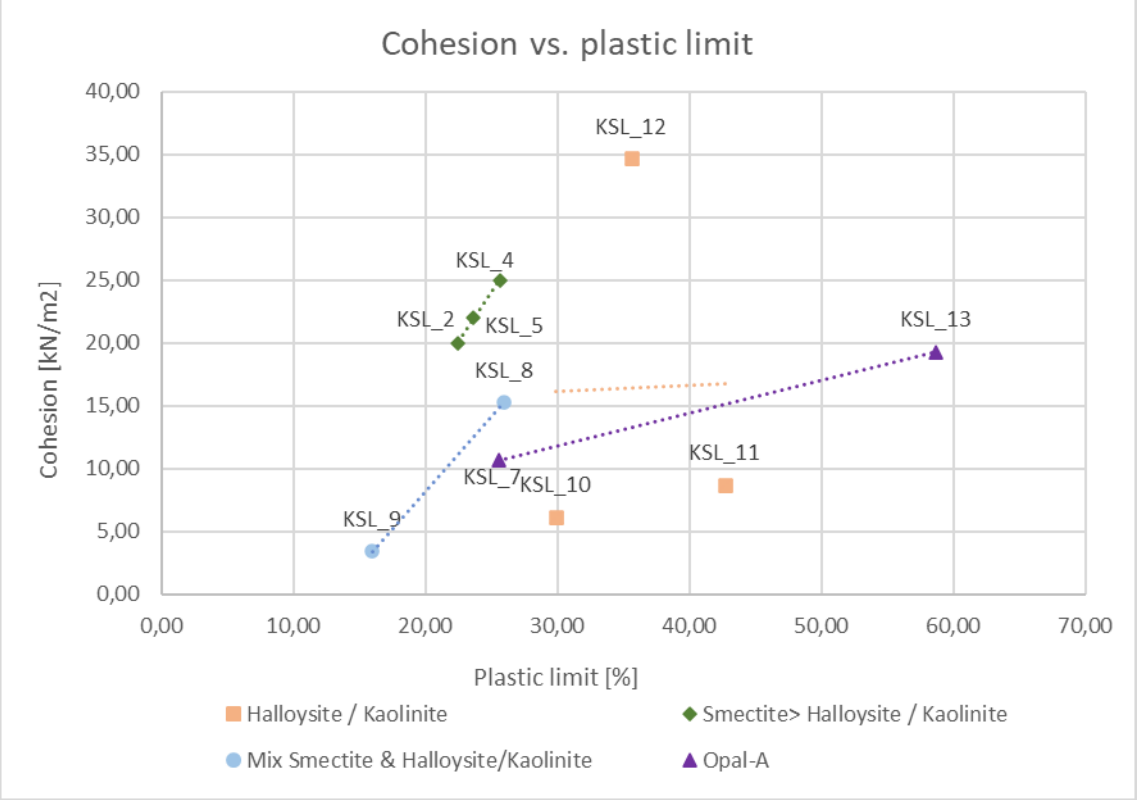

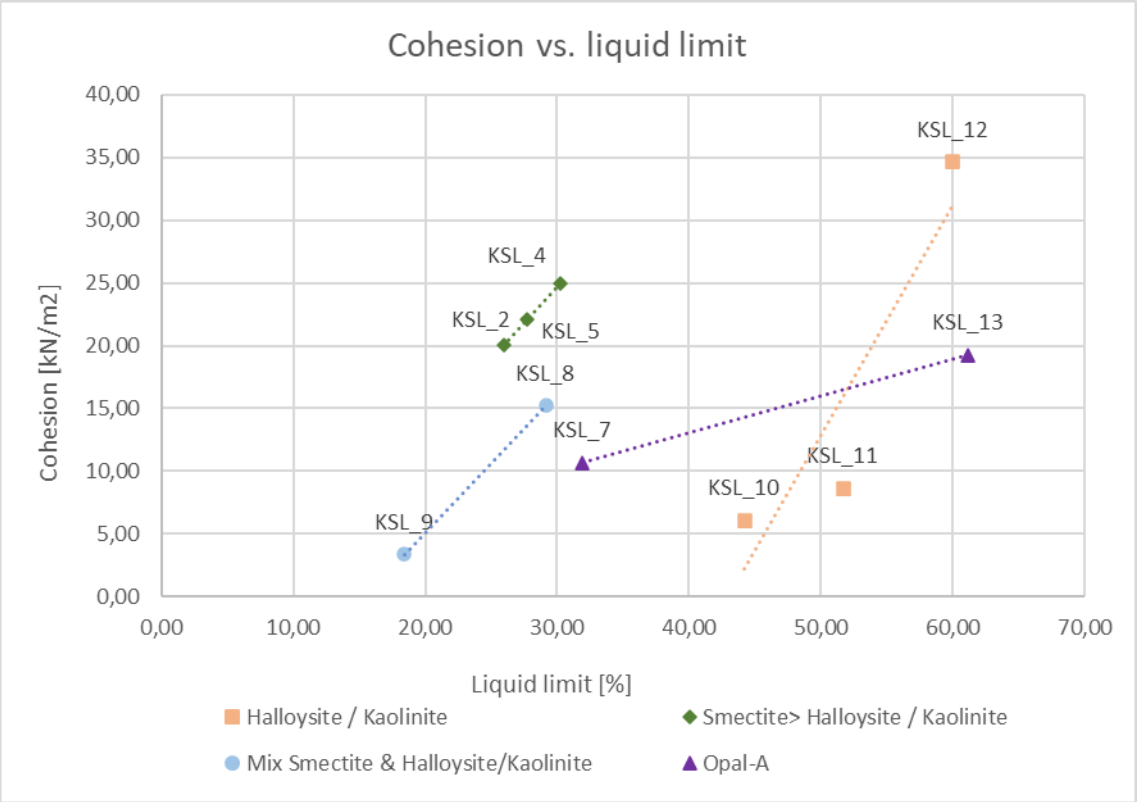
Cohesion vs. liquid limit
Cohesion [kN/m2]
Liquid limit [%]
40,00
35,00
30,00
25,00
20,00
15,00
10,00
5,00
0,00
0,00
10,00
20,00
30,00
40,00
50,00
60,00
70,00
KSL_12
KSL_4
KSL_2
KSL_5
KSL_13
KSL_8
KSL_7
KSL_11
KSL_10
KSL_9
Halloysite / Kaolinite
Smectite> Halloysite / Kaolinite
Mix Smectite & Halloysite/Kaolinite
Opal-A

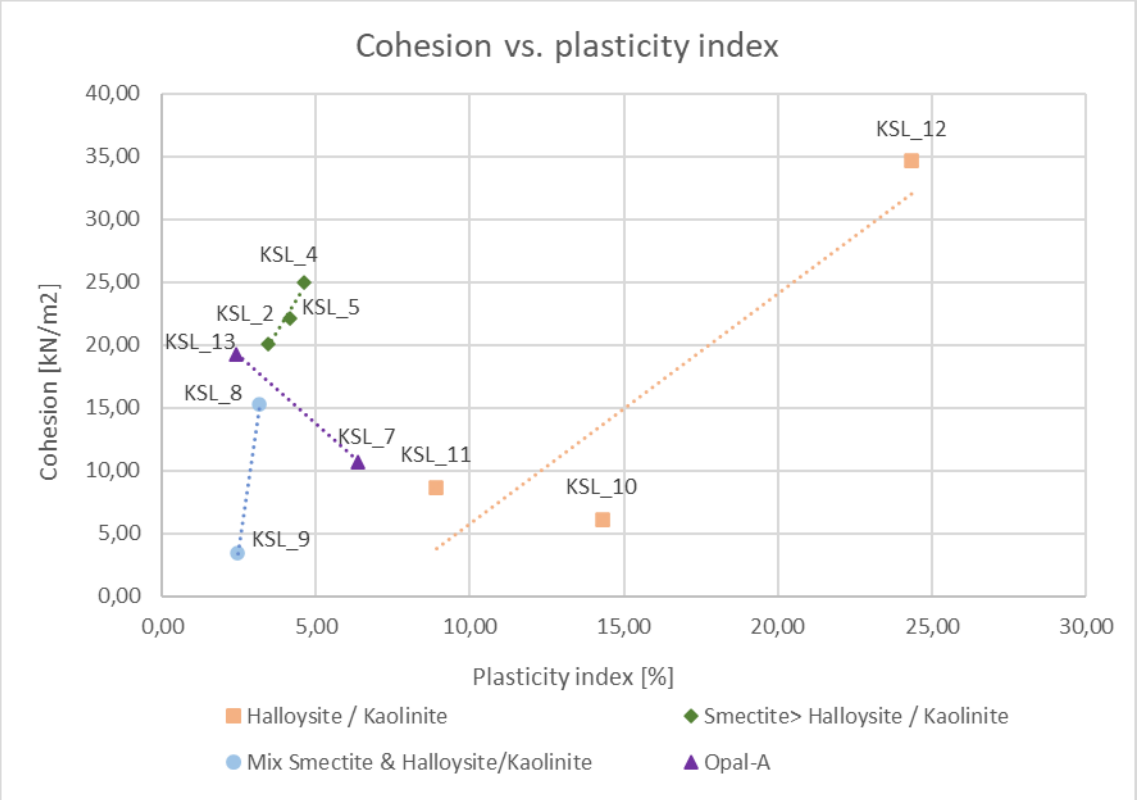
Cohesion vs. plasticity index
Cohesion [kN/m2]
Plasticity index [%]
40,00
35,00
30,00
25,00
20,00
15,00
10,00
5,00
0,00
0,00
5,00
10,00
15,00
20,00
25,00
30,00
KSL_12
KSL_4
KSL_2
KSL_5
KSL_13
KSL_8
KSL_7
KSL_11
KSL_10
KSL_9
Halloysite / Kaolinite
Smectite> Halloysite / Kaolinite
Mix Smectite & Halloysite/Kaolinite
Opal-A

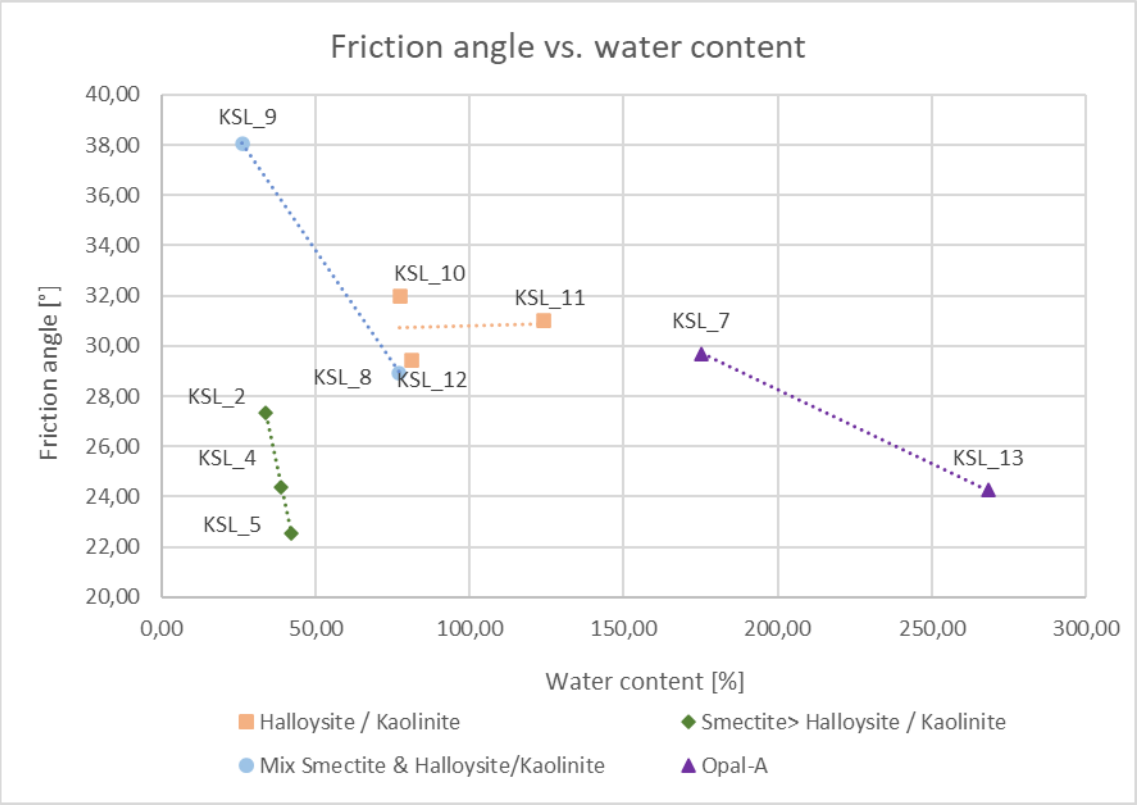
Friction angle vs. water content
Friction angle [°]
40,00
38,00
36,00
34,00
32,00
30,00
28,00
26,00
24,00
22,00
20,00
0,00
50,00
100,00
150,00
200,00
250,00
300,00
Water content [%]
KSL_9
KSL_10
KSL_11
KSL_7
KSL_8
KSL_12
KSL_2
KSL_4
KSL_5
KSL_13
Halloysite / Kaolinite
Smectite> Halloysite / Kaolinite
Mix Smectite & Halloysite/Kaolinite
Opal-A

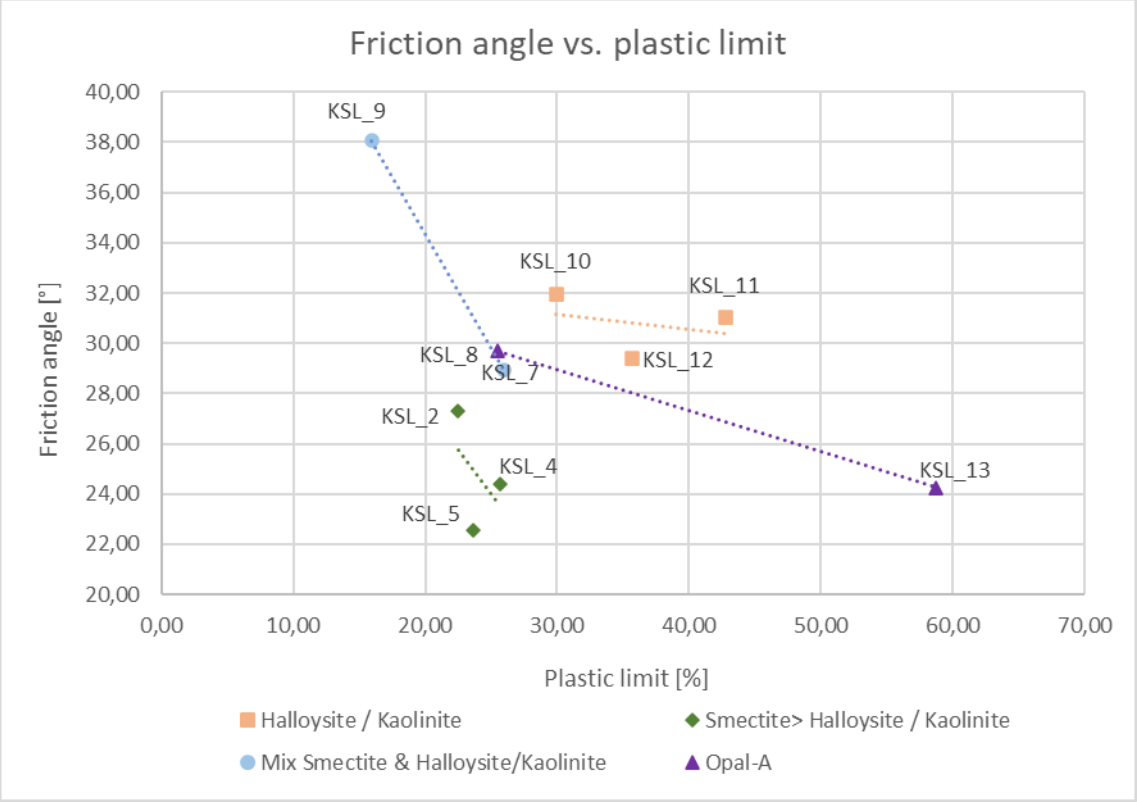
Friction angle vs. plastic limit
Friction angle [°]
40,00
38,00
36,00
34,00
32,00
30,00
28,00
26,00
24,00
22,00
20,00
0,00
10,00
20,00
30,00
40,00
50,00
60,00
70,00
Plastic limit [%]
KSL_9
KSL_10
KSL_11
KSL_8
KSL_7
KSL_12
KSL_2
KSL_4
KSL_5
KSL_13
Halloysite / Kaolinite
Smectite> Halloysite / Kaolinite
Mix Smectite & Halloysite/Kaolinite
Opal-A

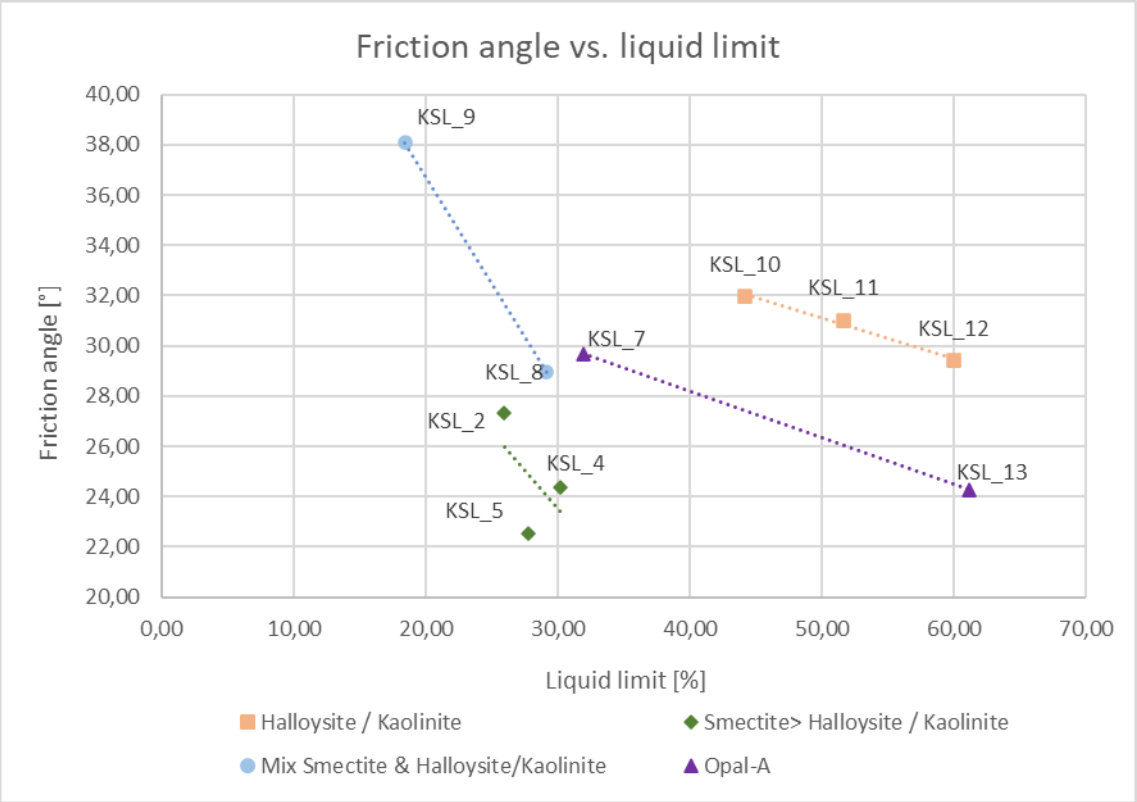
Friction angle vs. liquid limit
Friction angle [°]
40,00
38,00
36,00
34,00
32,00
30,00
28,00
26,00
24,00
22,00
20,00
0,00
10,00
20,00
30,00
40,00
50,00
60,00
70,00
Liquid limit [%]
KSL_9
KSL_10
KSL_11
KSL_12
KSL_7
KSL_8
KSL_2
KSL_4
KSL_13
KSL_5
Halloysite / Kaolinite
Smectite> Halloysite / Kaolinite
Mix Smectite & Halloysite/Kaolinite
Opal-A

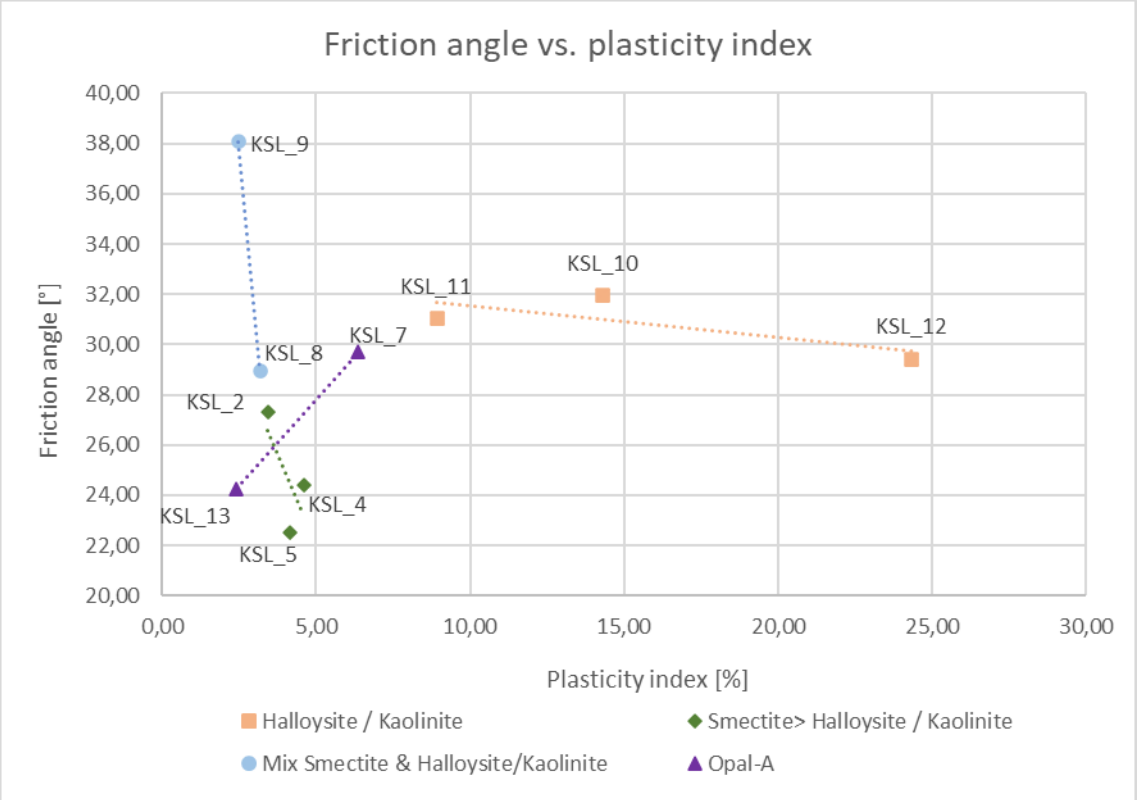
Friction angle vs. plasticity index
Friction angle [°]
40,00
38,00
36,00
34,00
32,00
30,00
28,00
26,00
24,00
22,00
20,00
0,00
5,00
10,00
15,00
20,00
25,00
30,00
Plasticity index [%]
KSL_9
KSL_10
KSL_11
KSL_12
KSL_7
KSL_8
KSL_2
KSL_4
KSL_13
KSL_5
Halloysite / Kaolinite
Smectite> Halloysite / Kaolinite
Mix Smectite & Halloysite/Kaolinite
Opal-A

11.8 Appendix H – Diagrams shear parameter vs. Atterberg limits considering alteration type

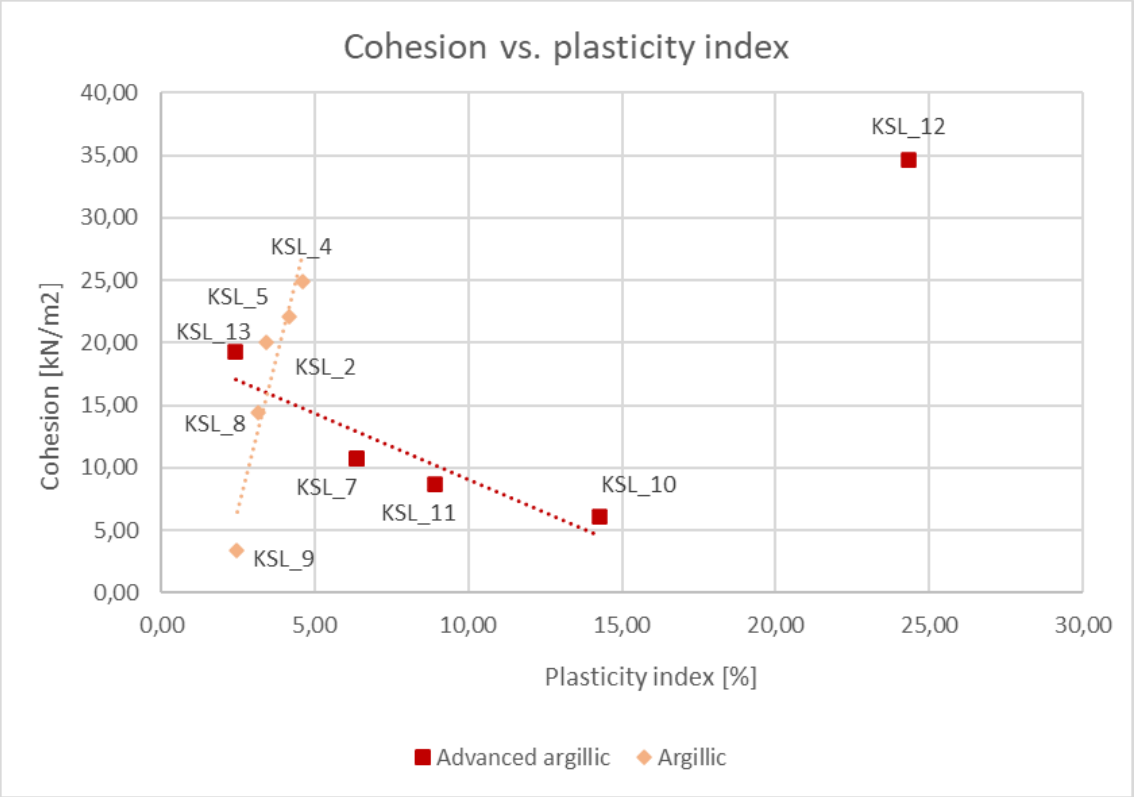

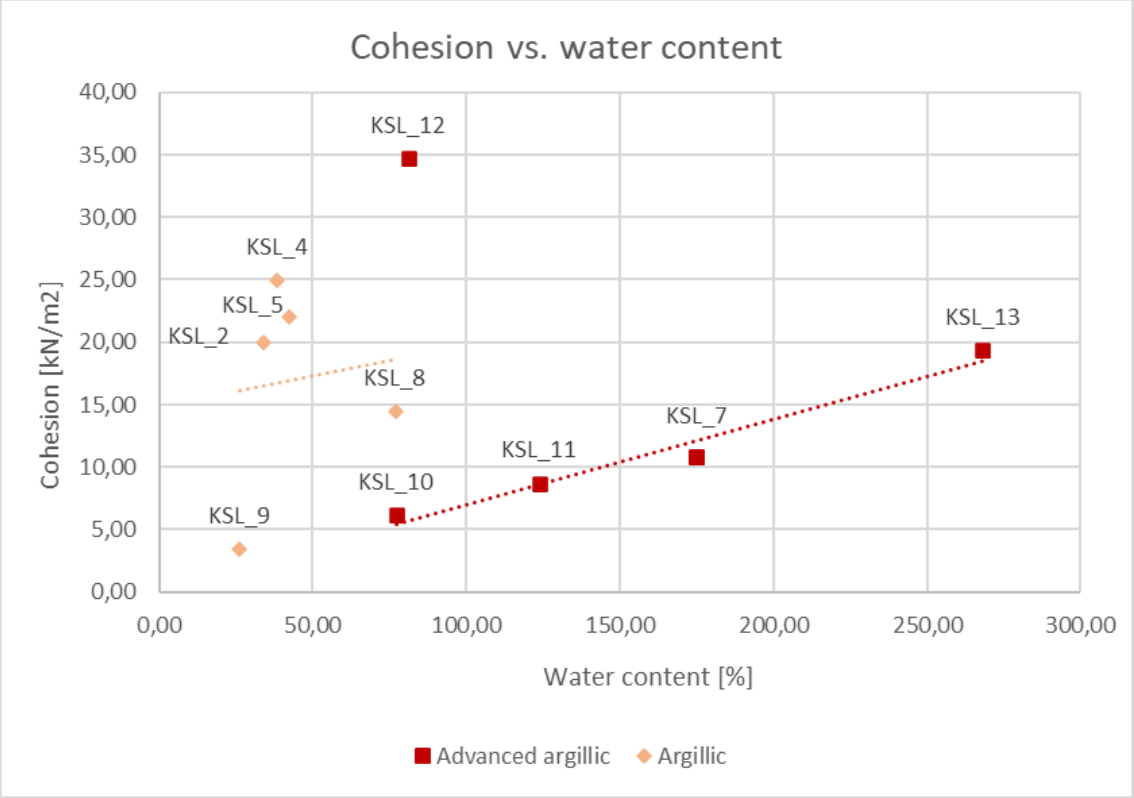

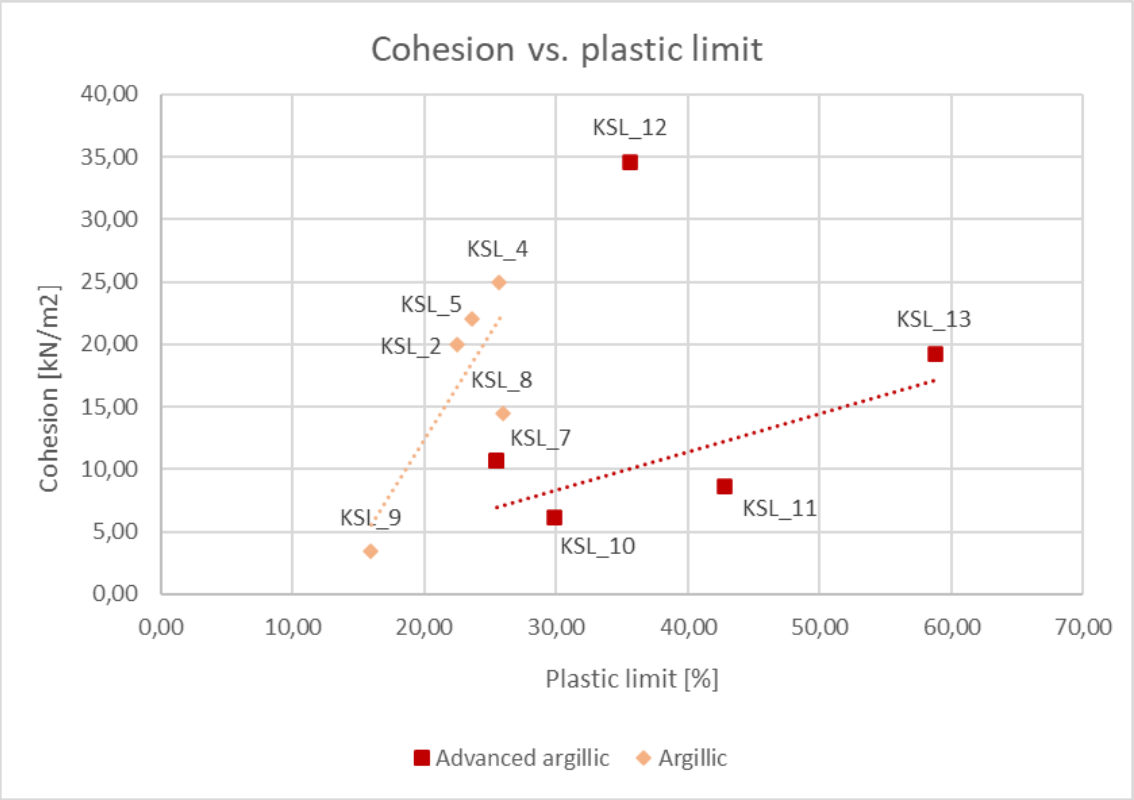
Cohesion vs. plastic limit
Cohesion [kN/m2]
40,00
35,00
30,00
25,00
20,00
15,00
10,00
5,00
0,00
0,00
10,00
20,00
30,00
40,00
50,00
60,00
70,00
Plastic limit [%]
KSL_12
KSL_4
KSL_5
KSL_2
KSL_13
KSL_8
KSL_7
KSL_9
KSL_11
KSL_10
Advanced argillic
Argillic

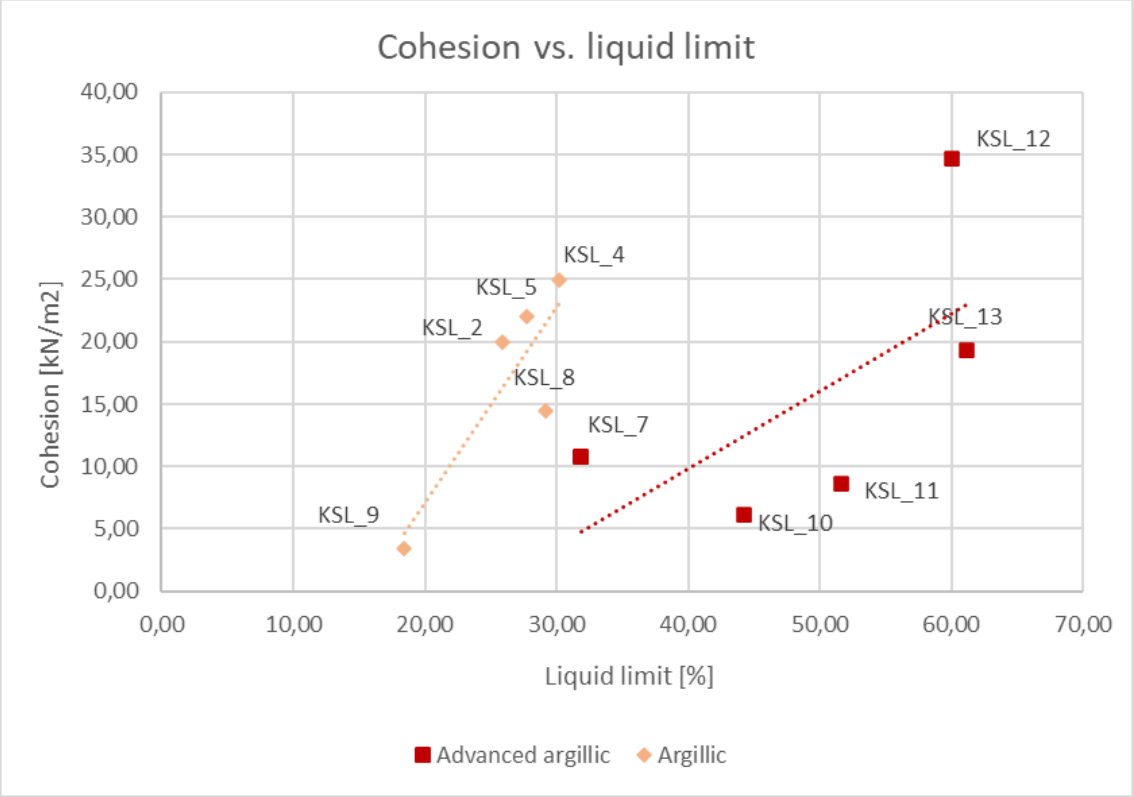
Cohesion vs. liquid limit
Cohesion [kN/m2]
40,00
35,00
30,00
25,00
20,00
15,00
10,00
5,00
0,00
0,00
10,00
20,00
30,00
40,00
50,00
60,00
70,00
Liquid limit [%]
KSL_12
KSL_4
KSL_5
KSL_2
KSL_13
KSL_8
KSL_7
KSL_11
KSL_9
KSL_10
Advanced argillic
Argillic

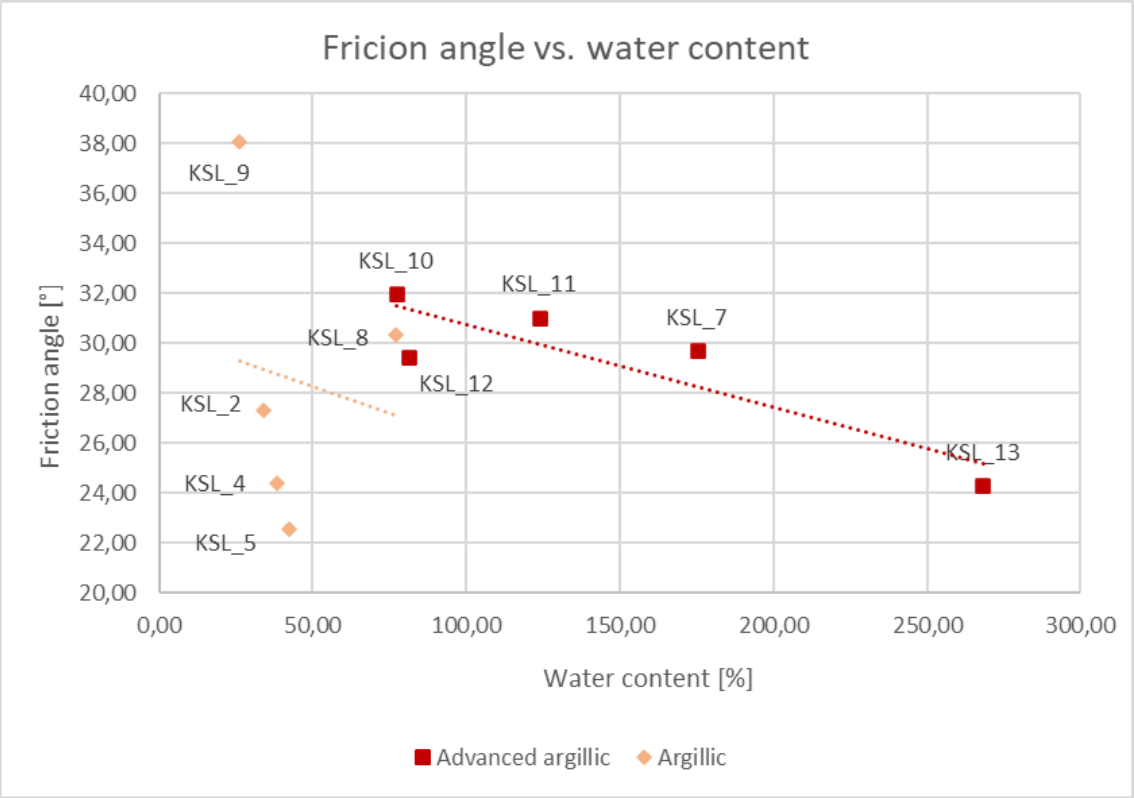
Fricion angle vs. water content
Friction angle [°]
40,00
38,00
36,00
34,00
32,00
30,00
28,00
26,00
24,00
22,00
20,00
0,00
50,00
100,00
150,00
200,00
250,00
300,00
Water content [%]
KSL_9
KSL_10
KSL_11
KSL_7
KSL_8
KSL_12
KSL_2
KSL_13
KSL_4
KSL_5
Advanced argillic
Argillic

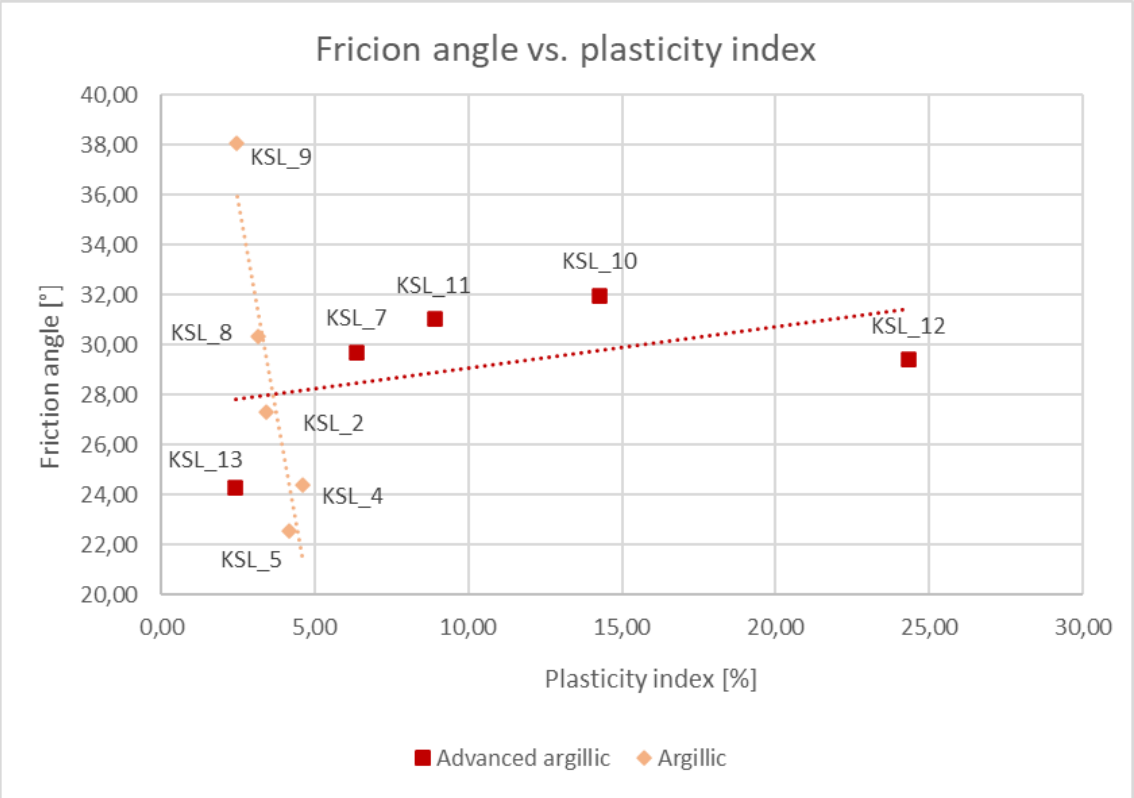
Fricion angle vs. plasticity index
Friction angle [°]
40,00
38,00
36,00
34,00
32,00
30,00
28,00
26,00
24,00
22,00
20,00
0,00
5,00
10,00
15,00
20,00
25,00
30,00
Plasticity index [%]
KSL_9
KSL_10
KSL_11
KSL_7
KSL_8
KSL_12
KSL_2
KSL_13
KSL_4
KSL_5
Advanced argillic
Argillic

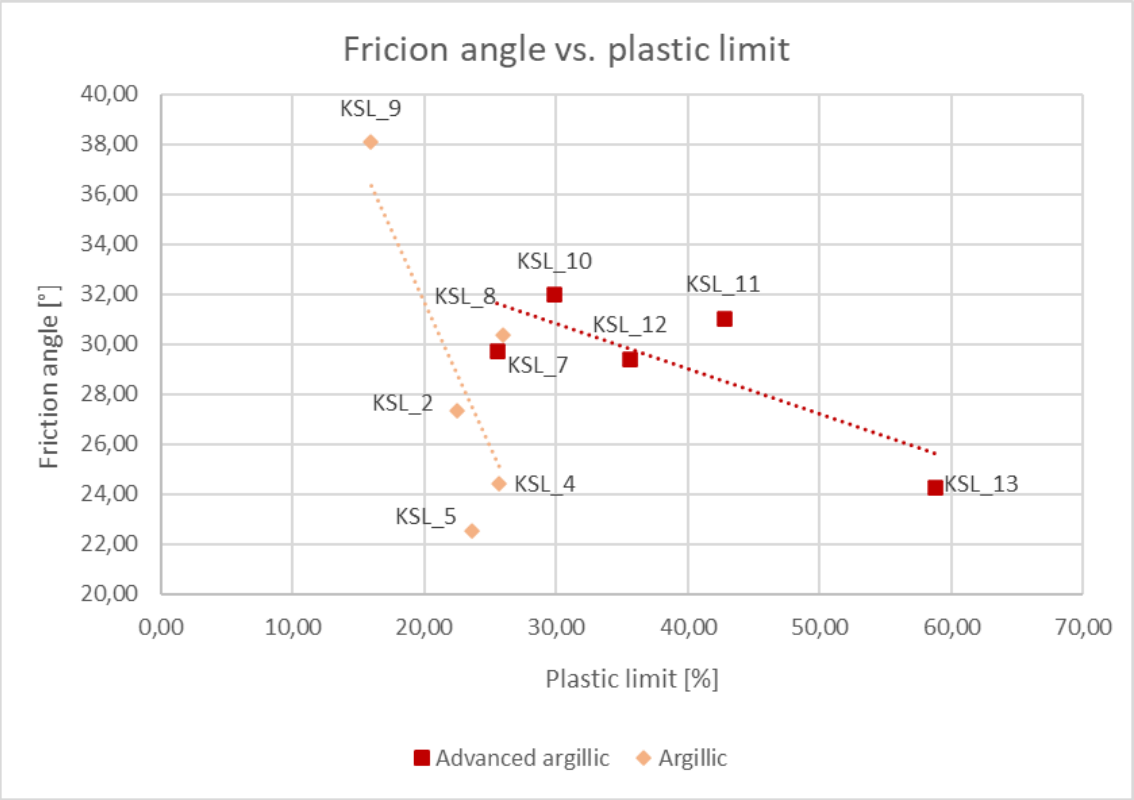
Fricion angle vs. plastic limit
Friction angle [°]
40,00
38,00
36,00
34,00
32,00
30,00
28,00
26,00
24,00
22,00
20,00
0,00
10,00
20,00
30,00
40,00
50,00
60,00
70,00
Plastic limit [%]
KSL_9
KSL_10
KSL_8
KSL_11
KSL_12
KSL_7
KSL_2
KSL_4
KSL_13
KSL_5
Advanced argillic
Argillic

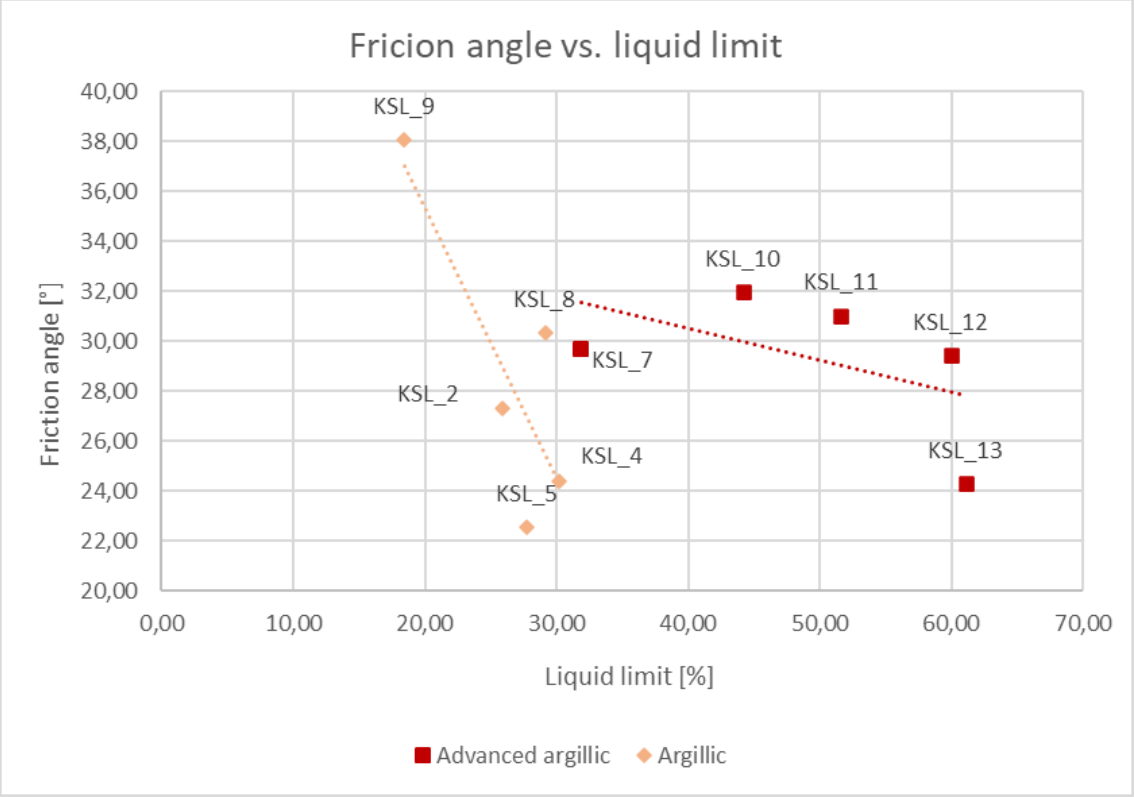
Fricion angle vs. liquid limit
Friction angle [°]
40,00
38,00
36,00
34,00
32,00
30,00
28,00
26,00
24,00
22,00
20,00
0,00
10,00
20,00
30,00
40,00
50,00
60,00
70,00
Liquid limit [%]
KSL_9
KSL_10
KSL_11
KSL_8
KSL_12
KSL_7
KSL_2
KSL_4
KSL_13
KSL_5
Advanced argillic
Argillic

11.9 Appendix I – Diagrams comparison dome vs. fault samples

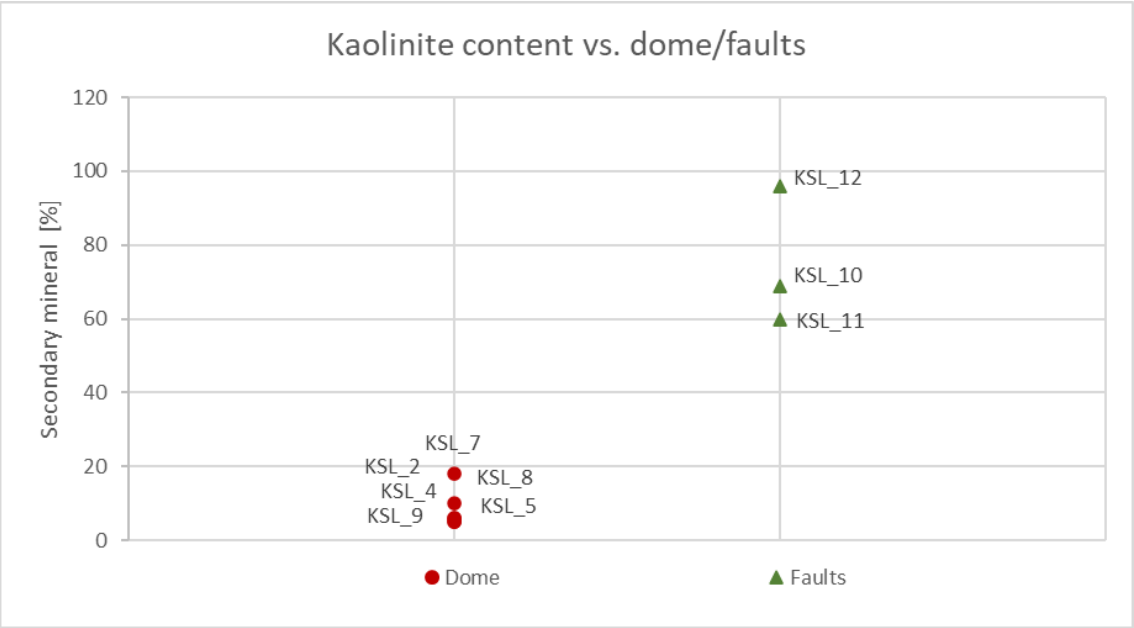

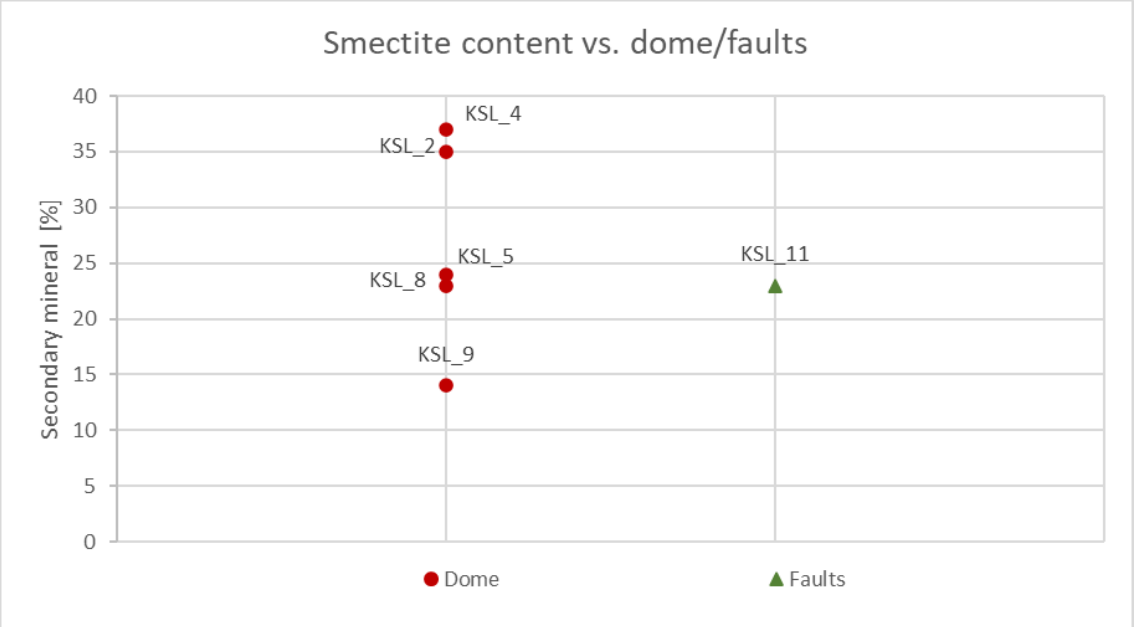

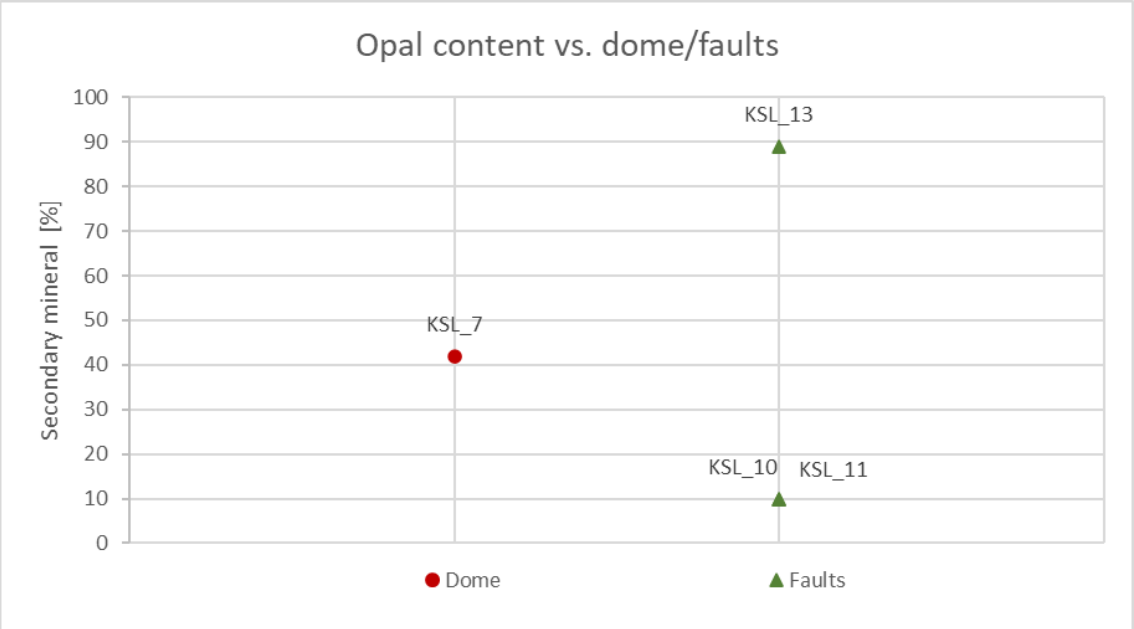
Opal content vs. dome/faults
Secondary mineral [%]
100
90
80
70
60
50
40
30
20
10
0
KSL_13
KSL_7
KSL_10
KSL_11
Dome
Faults

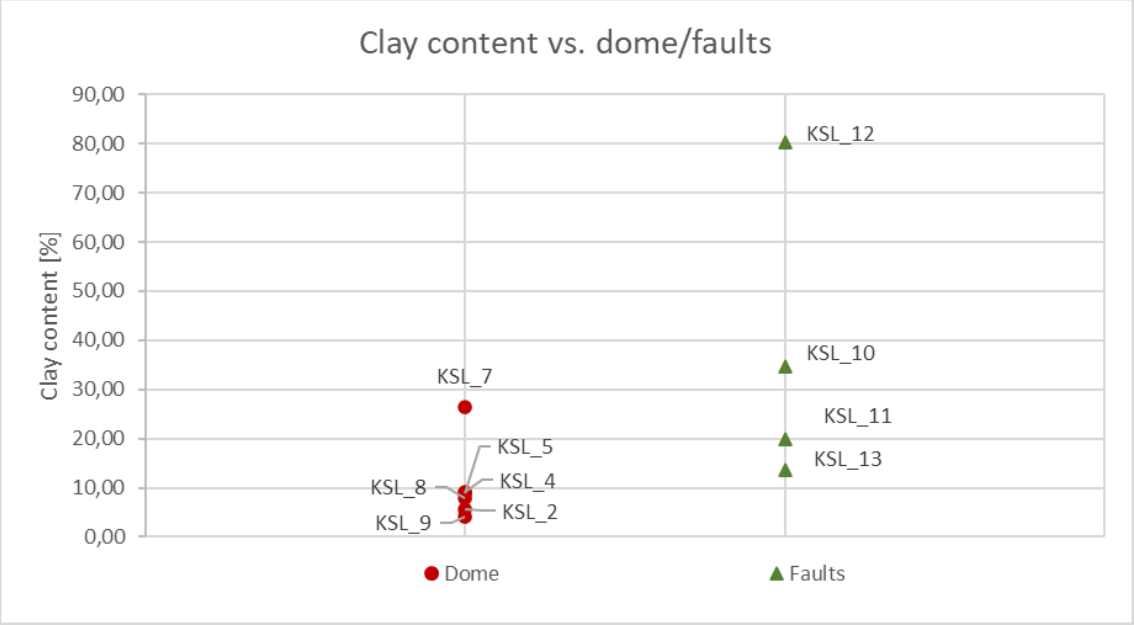
Clay content vs. dome/faults
Clay content [%]
90,00
80,00
70,00
60,00
50,00
40,00
30,00
20,00
10,00
0,00
KSL_12
KSL_10
KSL_7
KSL_11
KSL_5
KSL_13
KSL_8
KSL_4
KSL_2
KSL_9
Dome
Faults

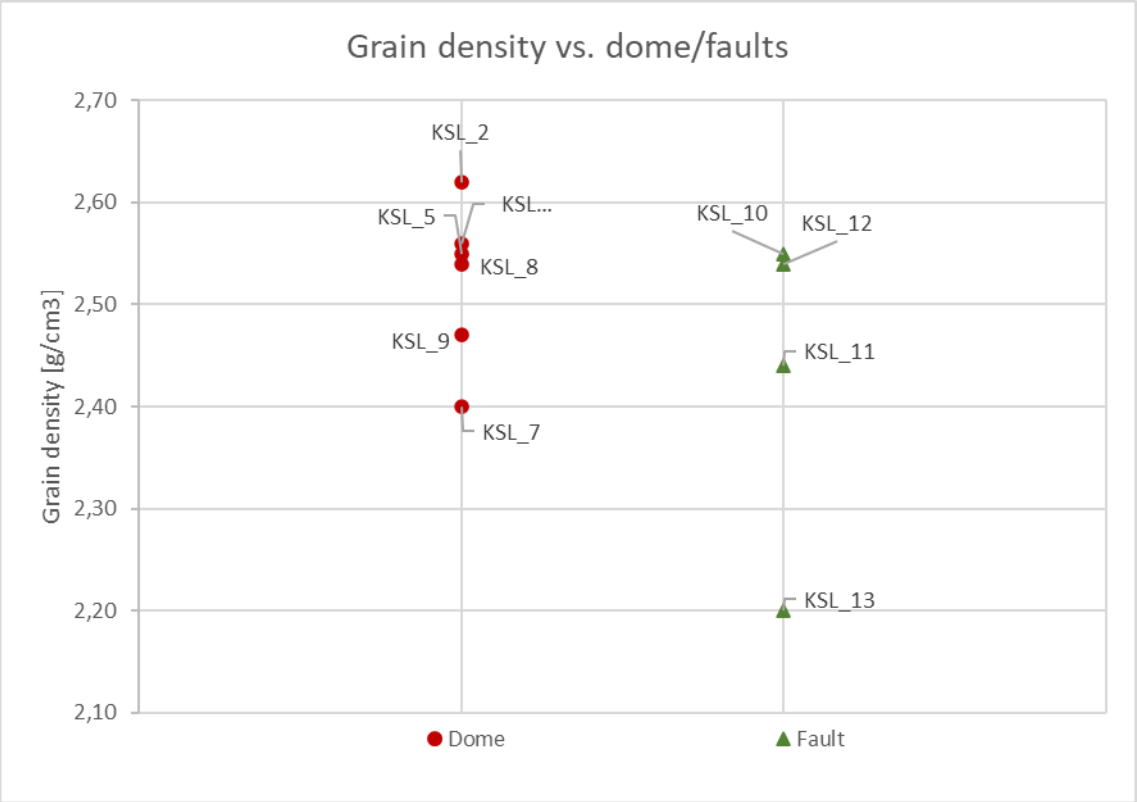
Grain density vs. dome/faults
Grain density [g/cm3]
2,70
2,60
2,50
2,40
2,30
2,20
2,10
KSL_2
KSL_5
KSL...
KSL_8
KSL_9
KSL_7
KSL_10
KSL_12
KSL_11
KSL_13
Dome
Fault

11.10 Appendix J – Diagrams comparison short-, long and fault influence

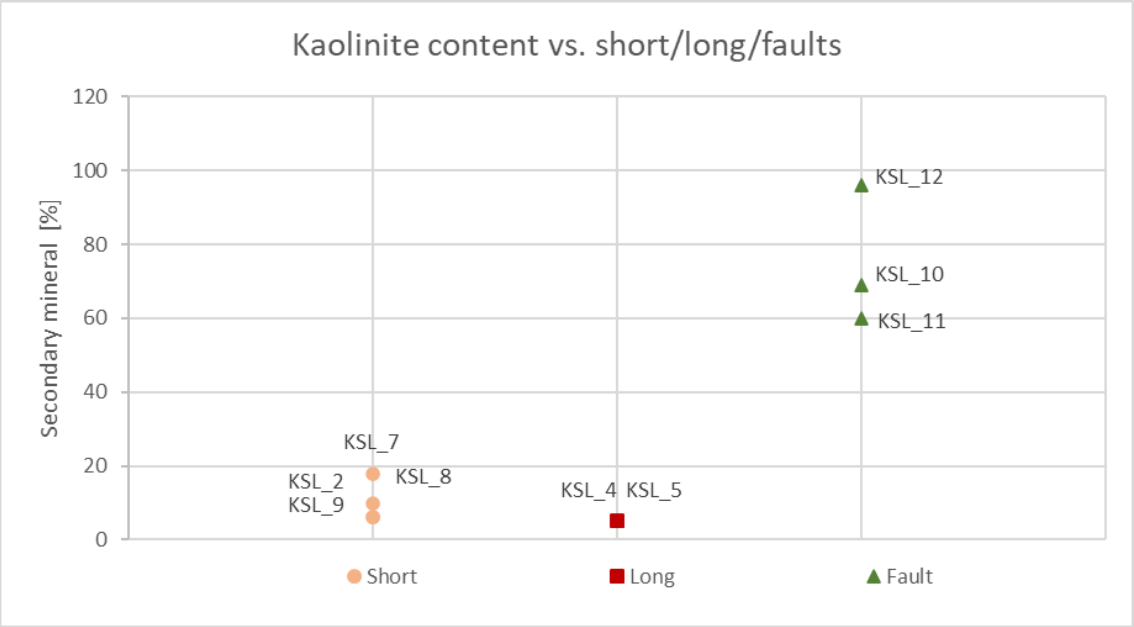

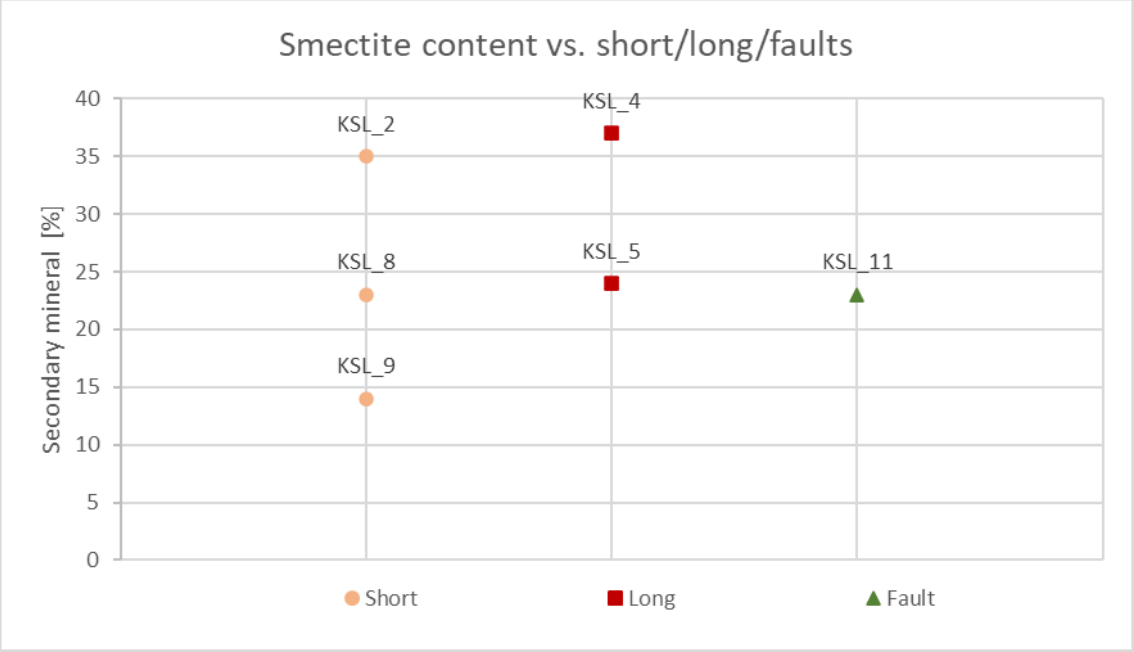

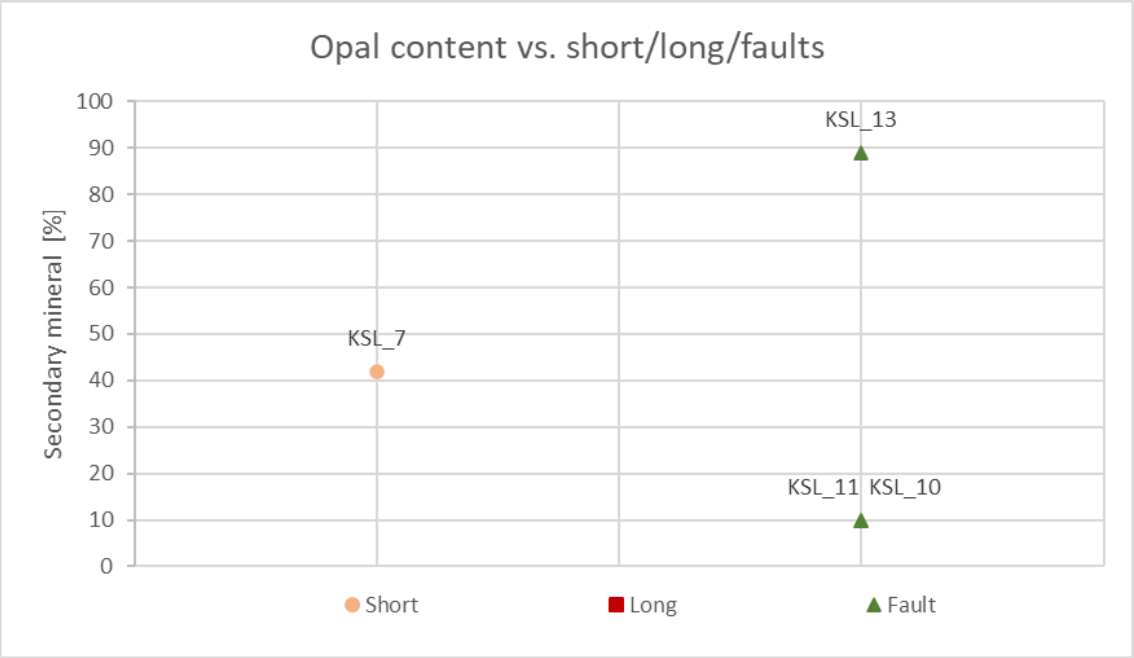
Opal content vs. short/long/faults
Secondary mineral [%]
100
90
80
70
60
50
40
30
20
10
0
KSL_13
KSL_7
KSL_11
KSL_10
Short
Long
Fault

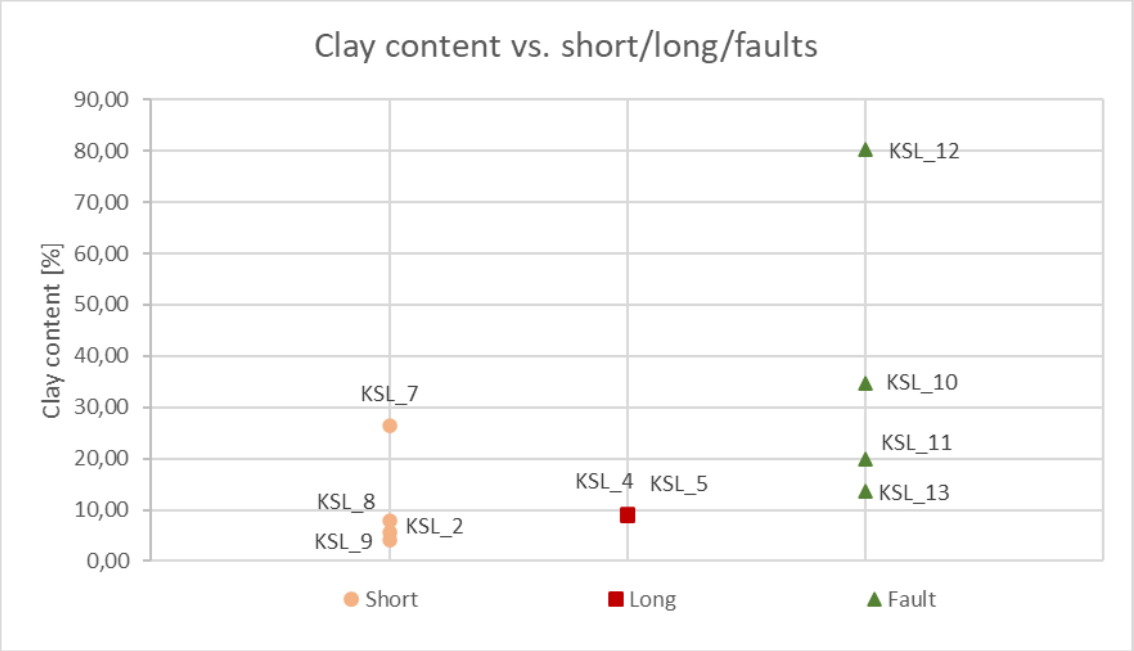
Clay content vs. short/long/faults
Clay content [%]
90,00
80,00
70,00
60,00
50,00
40,00
30,00
20,00
10,00
0,00
KSL_12
KSL_7
KSL_10
KSL_11
KSL_4
KSL_5
KSL_8
KSL_13
KSL_2
KSL_9
Short
Long
Fault

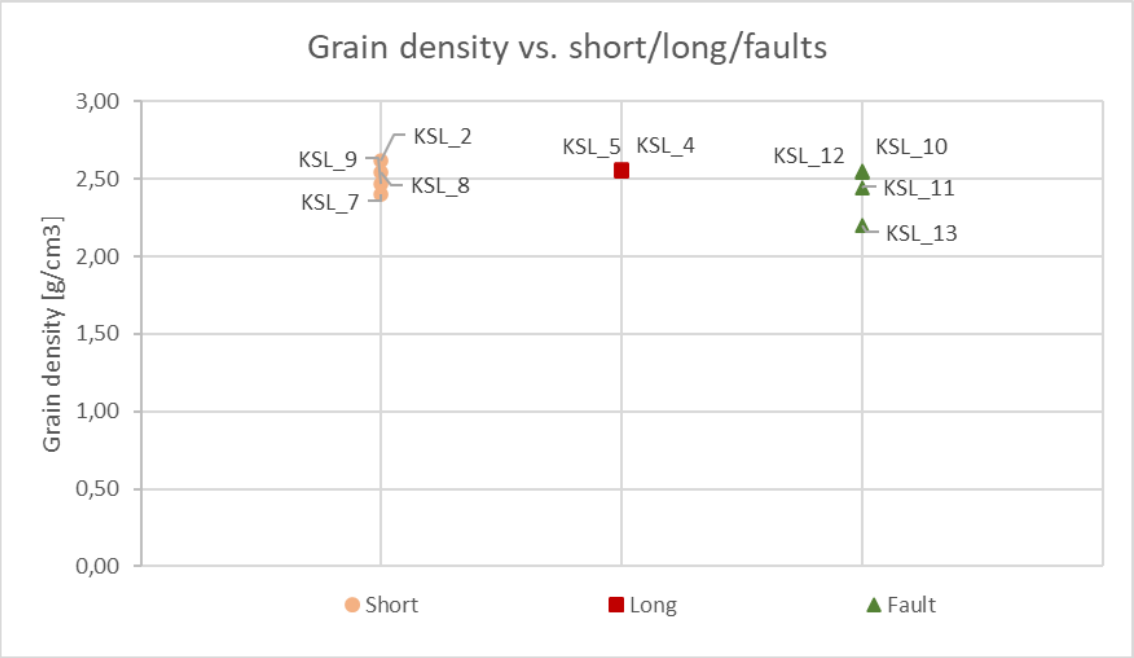
Grain density vs. short/long/faults
Grain density [g/cm3]
3,00
2,50
2,00
1,50
1,00
0,50
0,00
KSL_9
KSL_2
KSL_8
KSL_7
KSL_5
KSL_4
KSL_12
KSL_10
KSL_11
KSL_13
Short
Long
Fault